Picosecond Pulse Measurements of Graphene

Nicholas Callum Hunter

Submitted in accordance with the requirements for the degree of
Doctor of Philosophy

The University of Leeds
School of Electronic and Electrical Engineering

May 2015

The candidate confirms that the work submitted is his/her own, except where work which has formed part of jointly authored publications has been included. The contribution of the candidate and the other authors to this work has been explicitly indicated below. The candidate confirms that appropriate credit has been given within the thesis where reference has been made to the work of others.

The majority of the work in Chapter 4 was published in the article:

"On-Chip Picosecond Pulse Detection and Generation Using Graphene Photoconductive Switches". Nicholas Hunter, Alexander S. Mayorov, Christopher D. Wood, Christopher Russell, Lianhe Li, Edmund H. Linfield, A. Giles Davies, and John E. Cunningham. Nano Lett., 2015, 15(3), pp 1591-1596.

In this article, Nicholas Hunter designed, fabricated and tested the devices. Alex Mayorov provided the analysis of the data and wrote the manuscript. The waveguide structure and experimental setup were based on previous experiments by Christopher Wood and Christopher Russell. The MBE growth was undertaken by Lianhe Li. The project was supervised by Edmund Linfield, Giles Davies and John Cunningham.

Acknowledgements

I would like to thank my supervisors, Professor John Cunningham, Professor Edmund Linfield and Professor Giles Davies for their guidance throughout my project. I would also like to thank the EPSRC for funding the project.

I am very thankful for the assistance and friendship from all my colleagues at the IMP, especially Dr. Chris Russell, Dr. Divyang Mistry, Dr. Mark Rosamond and Dr. Alex Mayorov, all of whom went above and beyond on countless occasions. Special thanks go to: Dr. Vaidotas Miseikis, who initiated this project and tutored me in device fabrication and characterisation; Dr. Chris Wood, who designed and maintained the experimental setup; Dr. Oscar Céspedes for the use of the Raman spectrometer; and Dr. Lianhe Li, who grew the LT-GaAs.

I would like to thank Dr. Andrew Burnett, Mr. Geoff Butterworth and Li Chen for their assistance and troubleshooting throughout, and Wilson Muchenje, Siddhant Chowdhury, Manoj Kumar and Matthew Swithenbank for their many valuable discussions over the years.

My family and friends have provided more entertainment and support than I could ever wish for, and for that I am eternally grateful. But most of all I would like to thank Emer, my best friend and fiancée, who has encouraged and inspired me every day throughout this PhD.

Abstract

This thesis investigates Graphene, a gapless semi-conductor with relativistic-like electron behaviour, using on-chip terahertz time-domain spectroscopy (OC-THz-TDS). In this technique single-cycle THz frequency pulses are emitted, guided by waveguides, and detected on a single chip. The device fabrication is achieved by incorporating planar Goubau line waveguides with epitaxial GaAs and graphene grown by chemical vapour deposition. Spectroscopy of these devices, with graphene spanning a small gap between the waveguides, reveals large oscillations that are mainly attributed to the gap and other waveguide features. Optical-pump terahertz-probe measurements are used to isolate the contribution of the graphene sample, and to observe the (picosecond timescale) hot-carrier lifetime.

The ultrafast carrier dynamics of graphene are then applied to demonstrate the first known measurements of graphene as an on-chip terahertz photoconductive detector; operating at frequencies up to 600 GHz. Pulsed terahertz emission from graphene is also demonstrated for a range of bias voltages, and considerations towards the design of all-graphene on-chip terahertz devices is discussed.

The spatial dependence of picosecond pulse detection using graphene is also investigated, achieved by mapping the optical probe location for a variety of switch geometries. A better understanding of the interaction of the terahertz field with the graphene over distances of 50 to 200 um is obtained, which may be used to improve performance and build towards making graphene a viable option in commercial THz-TDS systems.

Contents

List of Tables

List of Figures

Abbreviations

AC	Alternating current
C	Carbon
c	Free space speed of electromagnetic waves
CH_4	Methane
CPW	Co-planar waveguide
Cu	Copper
CVD	Chemical vapour deposition
DC	Direct current
DI	De-ionised
EM	Electromagnetic
FFT	Fast Fourier transform
FS-THz-TDS	Free-space terahertz time-domain spectroscopy
FTIR	Fourier transform infra-red (spectroscopy)
FWHM	Full width at half maximum
GBIP	General purpose interface bus
GDC	Grating dispersion compensator
HF	Hydrofluoric Acid
IPA	Isopropyl alcohol
LED	Light emitting diode
$LiTaO_3$	Lithium Tantalate
LT-GaAs	Low temperature grown gallium arsenide
MBE	Molecular beam epitaxy
MSL	Microstrip transmission line
NIR	Near infra-red
OC-THz-TDS	On-chip terahertz time-domain spectroscopy

OPOP	Optical-pump optical-probe
OPTP	Optical-pump terahertz-probe
PC	Photoconductive
PCB	Printed circuit board
PGL	Planar Goubau line (waveguide)
PMMA	Poly(methyl methacrylate)
PTE	Photo-thermoelectric
QWP	Quarter wave plate
SiC	Silicon carbide
SI-GaAs	Semi-insulating gallium arsenide
SL	Slot line (waveguide)
SNR	Signal-to-noise ratio
TEM	Transverse electromagnetic
TM	Transverse magnetic
TOF	Time of flight
UV	Ultra violet
VNA	Vector network analyser

Chapter 1: Introduction

Terahertz (THz) radiation lies between the microwave and infrared region of the electromagnetic spectrum (covering the range roughly from 300 GHz to 10 THz) and has many proposed applications across the fields of imaging,[1] sensing[2] and communications.[3] It is non-ionising, non-destructive and can spectroscopically identify a large number of materials, including drugs of abuse and explosives.[4] Despite being utilised for research purposes for over 60 years, specific industrial applications have been slow to emerge, as a result of many current THz technologies offering either low power, being very large (requiring expensive laser systems) or requiring cryogenic cooling. As the research field has expanded, increasing pressure has been placed on the community to produce new materials to generate or detect THz radiation, which are inexpensive, more powerful and can operate at room temperature.

Since its discovery,[5] graphene has been shown to exhibit high room-temperature carrier mobility,[6,7] a wide-band optical transparency in the infrared and visible light ranges,[8] and fast (relative to many semiconductors) hot-carrier transport dynamics,[9] where the kinetic energy of the photoexcited carriers exceeds that of lattice. Investigations of the high frequency properties of graphene have demonstrated picosecond (ps) hot-carrier lifetimes[10–13] and THz frequency oscillations of the carrier density[14,15] that have been exploited for a range of applications, such as THz frequency emission[16] or amplification.[17] Monolayer graphene transistors have also been demonstrated at frequencies approaching the THz band,[18,19] although these devices show rather low modulation ratios, which limit their potential as logic based components for computing. However, for analogue applications such as communications or sensing, graphene has the potential to be produced cheaply[20], making it preferable provided its performance can match that of current semiconductor technology.

This project set out to study the terahertz properties of graphene using spectroscopic techniques. The optical conductivity of graphene in the visible range is frequency independent and is determined by the fine constant,[8] while at terahertz frequencies, the conductivity of graphene has been shown to sharply increase due to Drude absorption.[21] Subsequent experimental investigations of this effect have studied the THz field propagation as it travels perpendicular to the plane of the graphene sheet,[21–27] as shown in Figure 1.1 (a). These revealed that the presence of multiple graphene layers,[26] changes in temperature,[27] and variations of carrier density[25] each affected the fast carrier dynamics.

Such measurements do not, however, allow the dynamics of the electrons, in the plane of the graphene, to be measured. These are important for obtaining a more complete understanding of the THz interaction with carriers and quasiparticles (plasmons, collective oscillations in the carrier distribution, for example) in the graphene, and could potentially allow their propagation velocity to be measured. To study these dynamics, THz time-domain spectroscopy (THz-TDS) techniques can be used to couple radiation via a waveguide directly to the edge of a graphene sheet as shown in Figure 1.1 (b). Detection of the THz-TDS signal at the other side of the graphene could allow sub-ps resolution measurements of the pulse propagation in the graphene. Frequency-domain spectroscopy of the graphene can also be performed by obtaining a fast Fourier transform of the time-domain data, as in the perpendicular measurements.

When the pulse propagation is in the same plane as the graphene, more direct measurements of the electronic and plasmonic effects in graphene can be observed. This is a rapidly growing field of research,[14,15,28] which has proposed a range of passive[29] and active[30–32] graphene devices for use in the terahertz range. As these frequencies are difficult to measure with conventional electronics, the field of graphene terahertz plasmonics is relatively unexplored. To date, the experimental configuration of Figure 1.1 (b) has only been performed at frequencies up to ~110 GHz where simple graphene transmission lines[33] and transient current excitation of graphene magneto-plasmons (plasmons controlled by a magnetic field)[34] have been studied. The work conducted in this thesis demonstrates a design and experimental configuration for testing THz pulse interaction in the same plane as the graphene by using on-chip THz-TDS (OC-THz-TDS) systems,[35,36] and presents the time- and frequency-domain results for a number of graphene configurations. Resonances are found in these measurements and a number of sources are considered, including plasmonic effects.

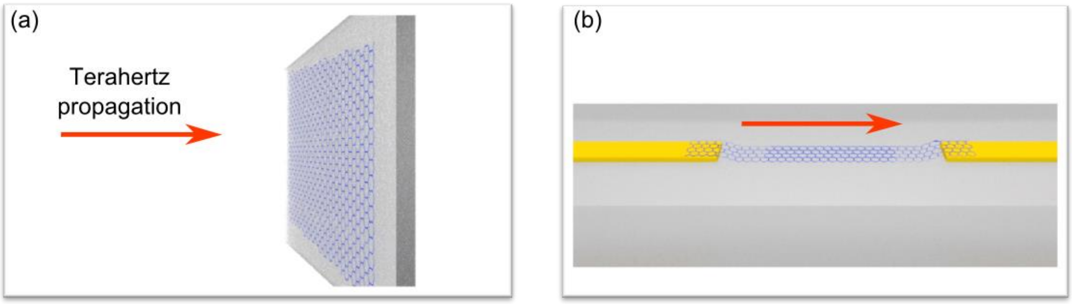

Figure 1.1: Methods for producing interaction between graphene and a terahertz field. (a) Pulse propagation that is perpendicular to the graphene plane using free space radiation. (b) Parallel pulse propagation to the graphene plane, where the graphene is directly coupled to an on-chip transmission line.

As a result of studying graphene in this configuration, terahertz pulse detection by optically sampling the graphene itself was found to be possible. Graphene photodetection using visible and infrared light has previously been demonstrated at optical modulation frequencies up to tens of gigahertz.[37,38] In this thesis, it is shown that by generating pulses using high-performance low-temperature-grown gallium arsenide (LT-GaAs) and established OC-THz-TDS techniques,[35,36,39] graphene photodetectors can operate at frequencies exceeding 600 GHz. In addition, the generation of few-picosecond pulses from voltage-biased graphene is also observed, supporting previous work based on un-biased, suspended graphene.[40] Such developments could lead to graphene-based on-chip THz sensors with the potential to significantly reduce the overall cost of OC-THz-TDS systems.

1.1 Structure of this thesis

Chapter 2 presents a background of OC-THz-TDS with particular emphasis on the materials and designs used throughout the thesis, including planar Goubau lines. A short background of graphene is also given and the key literature for the DC electronic, high frequency terahertz and optical properties is discussed.

The processing steps that were used to fabricate graphene OC-THz-TDS devices are documented in Chapter 3, and the developments that were implemented to increase device yield are also discussed. The specific system configuration chosen for the OC-THz-TDS system used here is also described. Characterisation of LT-GaAs material anneal temperatures are then discussed, using a range of characterisation techniques, also providing an introduction to the measurements that are used throughout the thesis. The Raman spectroscopy methods used to characterise graphene are also presented.

Chapter 4 initially presents and characterises the graphene OC-THz-TDS device design that is used for measurements in Chapters 4, 5 and 6. A sequence of graphene spectroscopy geometries are presented and tested, gradually increasing in complexity. Spectroscopy of optically pumped graphene is then demonstrated and the results are discussed.

Picosecond pulse detection using graphene as a photoconductive detector and emitter is demonstrated independently in Chapter 5, using LT-GaAs to characterise each technique. Measurements of simultaneous graphene pulse emission and detection are also presented, and the results are discussed.

Chapter 6 investigates the graphene detected picosecond pulse signal as a function of the spatial probing location. Measurements are made along the length of a rectangular graphene strip, where the width of the strip is of similar dimensions to the laser spot size. 2D mapping of the laser spot on larger semi-circle graphene regions are also presented.

Chapter 7 concludes the work of the project by summarising the key results and suggesting topics for future work.

Chapter 2: Background and theory

2.1 Introduction

This chapter discusses the relevant literature and highlights the key principles used for investigating picosecond phenomenon in graphene. It will, first of all, introduce on-chip terahertz time-domain spectroscopy (OC-THz-TDS) systems, giving a brief background to the technology and its applications. The individual components of the THz-TDS system are then discussed, including a comparison of some of the key terahertz waveguide geometries. The Goubau waveguide geometry used throughout this thesis is then discussed in detail in Section 2.3. In Section 2.4 of this chapter, some of the key electronic, terahertz and optical properties of graphene are discussed. Throughout this section, justifications are given as to why this is an interesting material for picosecond time-scale measurements and literature is presented on the mechanisms that are important throughout this thesis.

2.2 On-chip terahertz time-domain spectroscopy

2.2.1 Introduction

The THz frequency band (0.3 – 10 THz) is particularly useful for spectroscopy of materials, since it offers a non-destructive means to observe low energy molecular transitions and vibrations. THz spectroscopy was preceded by mm-wave (30 to 300 GHz) spectroscopy. The mm-wave band was developed to increase the resolution of radar technology after World War II.[41] The technology and techniques quickly advanced operating frequencies, reaching the lower end of the THz band in 1954.[42] The experimental configuration for measuring the time-domain response of mm-wave pulses was developed in the mid 1970's,[35] and subsequent advances in photoconductive materials[43,44] supported the implementation of the first on-chip THz time-domain spectroscopy (OC-THz-TDS) system.[45]

The first application of THz-TDS investigated changes of permittivity in GaAs as a function of sub-picosecond optical illumination, measured by the phase of THz pulse reflections at a $LiTaO_3$-GaAs impedance mismatch.[46] Applications then advanced onto spectroscopy of materials such as erbium iron garnets,[47] and crystalline materials such as lactose monohydrate.[48] The generation and detection of THz radiation in free space (FS-THz-TDS) was developed shortly after OC-THz-TDS and allowed higher bandwidth and collection efficiency.[49] This configuration also allowed fast transmission measurements of many different samples by placing them directly in the terahertz beam path. The bandwidth of FS-THz-TDS systems was increased by using optical rectification,[50,51] which is only limited by the duration of the ultrafast laser source, rather than the carrier dynamics of photoconductive material. THz-TDS spectroscopy came full circle in 2004 when the free space radiation was coupled into a single wire transmission line, demonstrating the coupling efficiency and transmission capabilities of a single wire,[52] or Sommerfeld line,[53] at terahertz frequencies, an adaptation of which is further discussed in Section 2.3.

FS-THz-TDS systems are most commonly used to inspect the frequency dependent transmission or reflection components of materials in the frequency range from DC to tens of terahertz. The fast Fourier transform (FFT) of the pulse can have resolutions as low as tens of GHz depending on size of the reflection-free time window, where the reflections can be caused by emitters, detectors or the sample itself. To guide the THz pulse FS-THz-TDS systems use a range parabolic mirrors and other THz optics that are often as large as 2 to 10 cm each. In contrast, OC-THz-TDS can incorporate emitters, detectors, samples and waveguides onto devices that are less than 1 cm^2. The waveguides provide sub-wavelength confinement and allow stronger field interaction when working with small sample sizes. As the pulse propagates along the surface of the sample, relatively long interaction lengths can be obtained (compared with free-space THz-TDS) even when measuring thin samples. This is especially useful for investigating spectral phenomenon in low-dimensional semiconductors, such as resonant plasmon and magneto-plasmon effects in 2-dimensional electron gasses,[54–56] and the spectroscopy of 1-dimensional carbon nanotubes.[57]

The following sections will give an overview of the components of an OC-THz-TDS system, used in this work, with a focus on how they can be tailored for the study of graphene. Section 3.2 will give a more detailed description of the system and its constituent components.

2.2.2 System overview

A schematic diagram of an OC-THz-TDS system is outlined in Figure 2.1. First, a pulsed laser (typically generating 10-100 fs duration pulses) emits a beam which is split into two paths; one path excites an emitter to generate a single-cycle THz pulse (lasting a fraction of a picosecond), while the other path illuminates a sampling detector. Control over one of the two path lengths, using a linear motion stage, allows convolution of the shorter sampling pulse with the broader terahertz pulse. By measuring many discrete samples across a range of stage positions (encompassing times before, during, and after the pulse arrival time), a reconstruction of the terahertz pulse shape can be made as it arrives at the

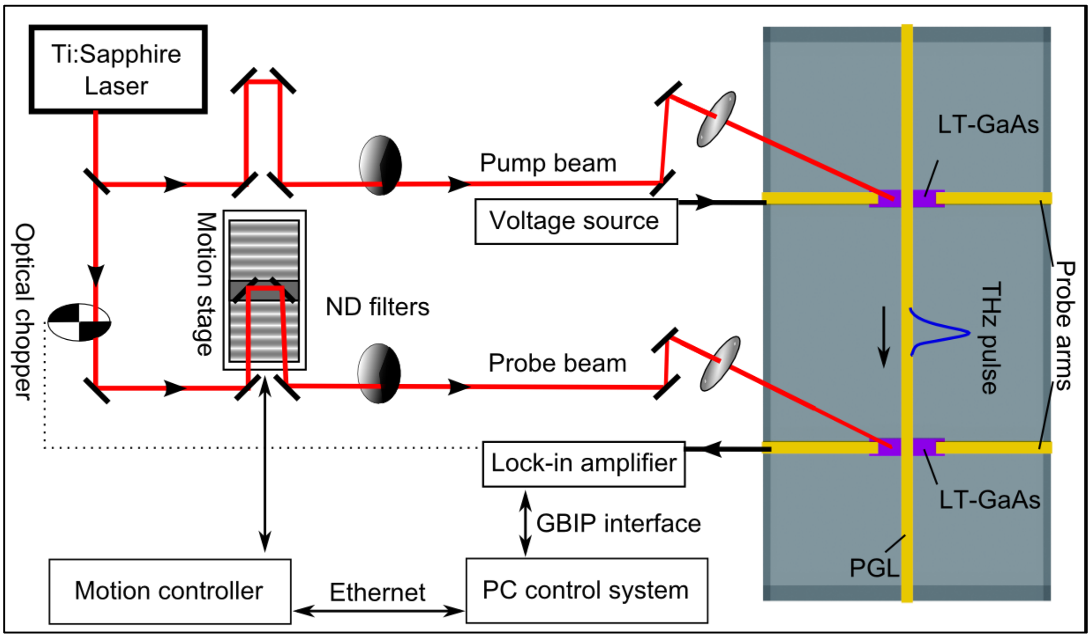

Figure 2.1: Schematic configuration for an on-chip THz-TDS system.

detector. The information retrieved is in the form of a pulse in the time-domain and, with a suitable reference measurement, the broadband amplitude and phase information of a particular sample are all recorded in a single scan. From this information, the complex permittivity of a sample can be extracted.

2.2.3 Photoconductive switches

Photoconductive switching involves the (short pulsed) illumination of a material to change its conductivity and hence, if the material is biased, a transient change in the flow of current will occur. This photoconductive effect is used in a range of devices such as light sensors, fibre optic receivers and digital cameras. In traditional semiconductors, the effect only occurs if the electron energy is larger than the bandgap of the photoconductive material. This causes an electron to be excited from the ground state in the valence band to an excited state in the conduction band, leaving a hole behind. If the material is subjected to a voltage bias, these charge carriers (both electron and hole) will flow across the device either until they hit a defect and emit a phonon, recombine by emission of a photon (as in an LED) or until they transfer energy into another carrier (Auger recombination).

The generation of terahertz signals by photoconductive switching requires fast carrier dynamics, including short carrier generation and recombination times. In the nearfield, the THz field that is coupled to the on-chip waveguide $E_{THz}(t) \propto J(t)$, where J is the current density and is given by $J = J_e + J_h = e[nv_e + pv_h]$. The magnitude of the radiated electric field in the far field regime is given by

$$E_{rad}(t) \propto \frac{\delta J}{\delta t}.$$

(2-1)

Where this equation can be expanded to become

$$E_{rad}(t) \propto e\left[v_e \frac{dn}{dt} + v_h \frac{dp}{dt} + n \frac{dv_e}{dt} + p \frac{dv_h}{dt}\right].$$

(2-2)

The terms $\mathrm{dn/dt}$ and $\mathrm{dp/dt}$ are representative of the rate at which the electron-hole pairs are generated and recombined. Therefore, to obtain the largest field strength in the near- or far- field regimes: the power of the laser pulse should be large; the laser pulse should be as short as possible; and the carriers should recombine quickly afterwards. Lasers with pulse widths in the region of 10 fs – 100 fs and suitably large "output" power are commercially available. The recombination time, however, is usually an intrinsic property of the photoconductive material. Furthermore, the latter two terms in Equation 2-2 require the acceleration of charge carriers due to the electrical bias; this means that the amplitude of the emitted pulse is proportional to the electric field across the gap and the mobility of the carriers. It is clear that the properties of the photoconductive material play a key role in the emission of THz radiation. There are three main properties that contribute to this, which will be discussed in the following sub-sections.

2.2.3.1 Intrinsic response time

Most semiconductor materials are photoconductive to some extent but many, such as Si, GaAs and InGaAs, are limited to operation at high microwave frequencies due to their intrinsic response time, given by

$$t_r^{-1} = t_{rec}^{-1} + t_t^{-1},$$

(2-3)

where t_{rec} is the carrier recombination time, and t_t is the carrier transit time. Although the recombination time is a property of the semiconductor, and cannot be changed, the transit time can be reduced (by introducing point defects into the material, for example). This is typically done by either by performing the MBE growth of GaAs at a lower temperature (LT-GaAs),[58] or by implanting high energy (MeV) ions into the semiconductor wafer using a particle accelerator.[59] The former method works by using more arsenic than gallium, and by preventing the arsenic from reaching temperatures where it can diffuse in an even manner. Instead, islands of As form throughout the lattice, which then act as carrier traps and reduce the average transit time. The defects and lattice-strain from this type of growth also adversely affect the mobility, so post-growth annealing is usually performed to (partially) precipitate the As in a controllable way. This process has to be tailored for each wafer growth recipe to obtain the best possible performance.

The carrier transit time t_t can be also be reduced by minimising the size of the metal-semiconductor-metal gap. It has been shown that bandwidths up to 510 GHz for 300 nm inter-digitated transducers on GaAs can be achieved.[60] However, LT-GaAs and ion implanted GaAs is advantageous as the material can be produced at wafer scales and allow for scalability of switches to optimise the total switch power.

2.2.3.2 Material dark resistivity

The material resistivity ideally would be zero under illumination, and infinite otherwise, allowing maximum modulation of the current and, hence, the largest amplitude transients could be achieved. Unfortunately, real semiconductors do not possess this property owing to dark currents that are created by thermal excitation at room temperature and non-zero intrinsic doping levels. LT-GaAs in its un-annealed state has a low resistivity, which is assumed to be from hopping across the conductive defect sites. Again, this may be improved by post-growth annealing of the wafer.[58]

2.2.3.3 Carrier mobility

To ensure the minimum possible rise time and, hence, the highest bandwidth, the carriers must be able to accelerate as quickly as possible after excitation. Typically, a perfectly arranged lattice will produce the highest mobility, and is reduced by scattering events from dopants and defects (or other carriers at higher carrier concentrations). To obtain high quality material capable of meeting these requirements, a growth technique that can grow a pure crystal is required, such as molecular beam epitaxy (MBE), which has the ability vary the dopant density and defect concentration with precision.

2.2.4 Laser excitation source

To generate pulsed THz radiation, the photoconductive material is typically photo-excited using a 10 to 100 fs optical source, such as a Ti:Sapphire laser, which typically have emission wavelengths of ~800 nm. Ti:Sapphire laser technology is relatively bulky, and is sensitive to misalignment. As LT-GaAs is excited by a maximum wavelength of 870 nm, the cost and complexity of the overall system is typically high (>£100k).

Currently, low carrier-lifetime materials that can be pumped by compact and cheaper 1.55 μm lasers are being developed[61] so that the systems may eventually have smaller form factors, cost less and become more robust.

2.2.5 Switch geometry

LT-GaAs is designed to have a very short electron mean free path, in order to obtain short carrier lifetimes. Unfortunately, this also means that many carriers are excited and recombine within the bulk of the material, without reaching a contact; hence they do not cause a current flow in the metal. In FS-THz-TDS systems these bulk carriers still emit radiation perpendicular to the applied electric field, but in OC-THz-TDS the main contribution to the signal is from transient current flow into the centre conductor. Only carriers that are generated near the edge of the metal probes are accelerated towards the contact and contribute to the current flow. To improve the current flow into the centre conductor, increasing the carrier mobility, reducing the defect density, or using short, wide semiconductor channels can be implemented. For LT-GaAs material that has already been grown to the highest standards capable of an MBE system, it is desirable to choose an optimised switch design to obtain the best results. The design considerations of an OC-THz-TDS switch include:

- Switch gap. This is the length of the semiconductor channel from one contact to another and effects the field distribution across the PC material. Larger biases are needed when using larger gaps to maintain electric field strength. Shorter gaps that were tested in this project (2.5 μm) were found to produce more efficient current flow into the metal wire, but were more susceptible to failure due to fabrication tolerances and material breakdown at higher powers. Ideally the length should not be larger than the laser beam spot size as the non-illuminated material will contribute unwanted series resistance. However, when the spot is smaller than the gap size, the largest THz amplitude is produced when the beam is focussed at the metal/semiconductor interface.[62]
- Switch width. Increasing the switch width maintains the same electric field strength and allows a larger photocurrent current to flow. However, it can also increase the "dark" resistance. Some devices incorporate interdigitated switch contacts to produce very large current flow for comparatively low bias voltages. Widths larger than the laser beam spot size are not detrimental if the dark resistance is suitably high, but are unnecessary as they can add parallel resistance to the signal. The capacitance of the switch is determined by the metal thickness, switch gap and switch width and is typically in the range of atto-Farads as the gap

is much larger than the metal thickness. Therefore, the time constants are typically less than the carrier relaxation rates of the semiconductor.

- Semiconductor thickness. Thicknesses of 2 μm are typically used for LT-GaAs in higher power devices, where the majority of the optical power is absorbed. Thicknesses down to 200 nm are typically used when the LT-GaAs has to be transferred to other substrates. This was done here to increase the fabrication yield, and allow for graphene integration into the transmission line (see Section 3.1).
- Sample photoconductivity. In this project it was found that the performance of the material was greatest when the polarisation of the optical beam and orientation of the electrical field were aligned. Therefore, the polarisation of the THz-TDS system and orientation of the device must be considered. Also, through substrate optical excitation can be used for transparent substrates, where illumination of larger areas of the photoconductive material can be achieved for similar gap sizes, and can lead to much larger signal amplitudes.

2.2.6 Guiding terahertz fields

In FS-THz-TDS systems the radiation is typically guided and focussed onto samples using parabolic mirrors, as shown in Figure 2.2. Modern free-space configurations provide a high brightness, as well as permitting the beam spot size to be as small as the diffraction limit will allow. However, there are some specialised areas of interest which require confinement of terahertz frequencies below the diffraction limited spot size (such as microfluidics and mesoscopic systems). To address this, lithographically- defined on-chip terahertz waveguides and transmission lines can be used. These confine the electromagnetic field to the sub-wavelength regime, along their length. This tight confinement permits relatively large interaction lengths for small samples when positioned in close proximity.

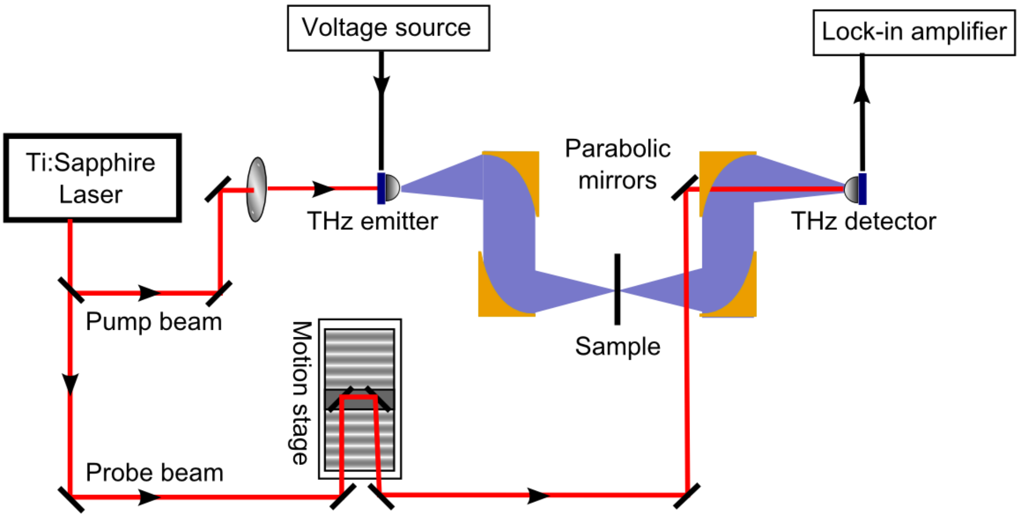

Figure 2.2: The schematic layout for a FS-THz-TDS system where parabolic mirrors (orange) are used to guide the THz radiation from the THz emitter, through the sample, and into the THz detector.

Free-space waveguides typically confine the field inside an enclosed single conductor where it must form into modes, which are solutions to the wave equations. The cross-sectional profile of a waveguide is typically rectangular or circular, but can also be a single wire suspended in free space, called a Goubau line (when surrounded by a dielectric). A modification of this approach, a single planar track on a dielectric substrate, is called a planar Goubau line (PGL)[63], and this was the primary waveguide used throughout this thesis owing to its high bandwidth at terahertz frequencies[36] and radial confinement profile.[39] PGLs are discussed in detail in Section 2.3, but to justify its selection it is compared to other planar structure THz waveguides. These include slot line (SL), microstrip line (MSL), and co-planar waveguide (CPW) geometries; a schematic of the electric field lines in each of these waveguides is shown in Figure 2.3.

CPWs are popular in conventional high frequency electronics since they can be easily fabricated in a single layer of metallisation onto printed circuit boards, and have a tight confinement of electric field to the surface. This allows many high frequency circuits to be clustered together on a single substrate with relatively low cross-talk. They have a symmetric electric field profile for one particular mode (the “odd mode”), and allow the centre conductor to be replaced with channels of thin-film material (e.g. two-dimensional electron gasses[55]) for investigations of their high frequency properties. However, CPWs have multiple modes of propagation, some of which (“even modes”) have the potential to bypass the centre conductor entirely.

SL waveguides are two-conductor structures that, amongst other applications, have been used to measure the THz properties of graphene and carbon nanotubes. For spectroscopy applications the material can be used to shunt the transmission lines. Although they have been used in OC-THz-TDS systems, they do not prevent higher order modes from forming[64] and, hence, are best suited to narrow bandwidth applications.

Microstrip lines confine most of their field in the material between the ground plane and the transmission line when the distance between the conductor and ground plane $d \ll \lambda$. The dominant mode is a quasi-transverse electromagnetic (TEM) field pattern which gives good, relatively low-loss, high frequency performance. At terahertz frequencies, common low permittivity substrates such as quartz, FR-4 or Duroid are too thick to allow support the quasi-TEM mode. However, thinner dielectric spacer layers can be used. These require multi-level fabrication processes adding extra complexity to device designs.

PGLs have been demonstrated to perform very well in the THz range, when used on a low permittivity substrates.[36,39,65] However, they are not well suited to lower frequencies due to its TM mode of propagation. The single wire structure means that the design, fabrication and integration of PGL waveguides with thin films are relatively simple. The confinement of the field is not as strong as the previously mentioned geometries, although the vast majority of the field remains close to the single conductor, and is not

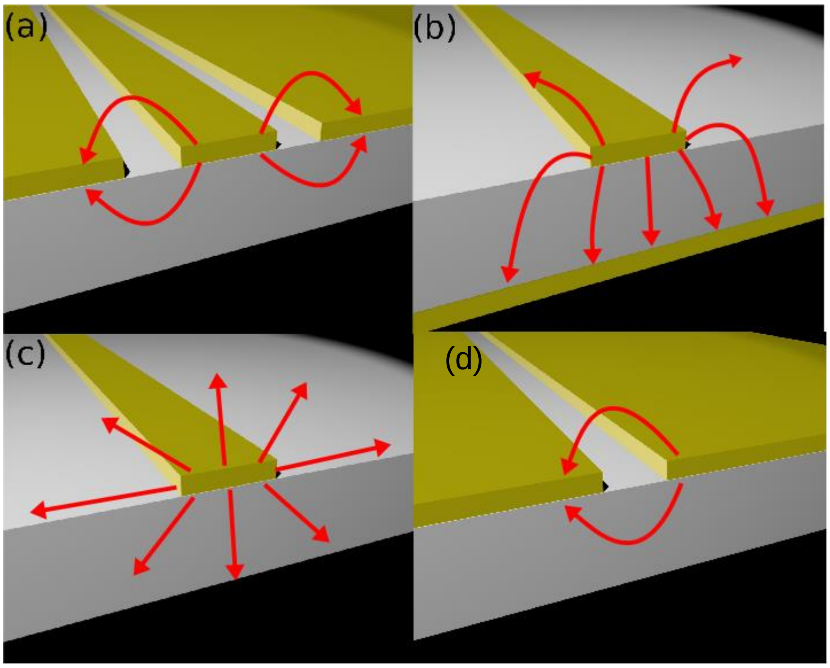

Figure 2.3: Waveguides and transmission lines used in on-chip THz devices with electric field distribution shown in red. (a) Co-planar waveguide. (b) Microstrip line. (c) Planar Goubau line. (d) Slot line.

spread across two or three conductors. Furthermore, the PGL geometry offers an easy integration route for planar materials like graphene. For these reasons it was chosen to form a THz probe into and out of graphene in the present work. The following section discusses the theory of the planar Goubau line in detail.

2.3 Planar Goubau waveguides

Planar Goubau lines (PGLs) historically originate from an analysis by Sommerfeld of the high frequency properties of single wire transmission lines.[53] This concept was expanded by Goubau for practical applications by covering the single wire in a dielectric to confine the field further and protect the wire.[66] Over 50 years later it was studied at THz frequencies[52] and was subsequently adapted for use on a planar PCBs and studied with mm-waves using vector network analysers.[63,67]

In order for the PGLs to work with conventional electronic signal generators and test equipment, it needed to incorporate a launching horn to convert a coplanar or coaxial transmission line into the Goubau line, whilst simultaneously exciting the Goubau mode. An example of this type of PGL excitation structure is shown in Figure 2.4. For use in an OC-THz-TDS system with photoconductive switches, it has been found that these conversions are not necessary, and the Goubau mode can be excited directly from a point-like source contacted adjacently to the conductor.[68] Another advantage of using this geometry in a TDS system over a VNA system is that it allows the bandwidth to be increased beyond the current technological limit of 1.1 THz in VNAs.

OC-THz-TDS systems allow the phase and polarity of reflections to be analysed if the pulse velocity is known and, hence, the information from a particular, known feature

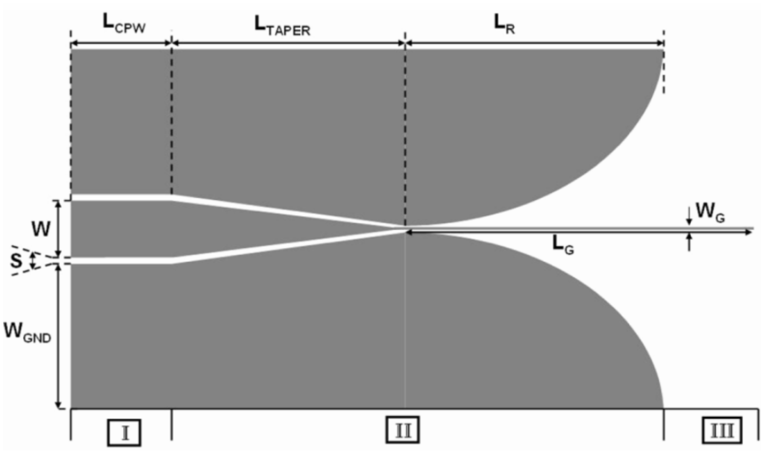

Figure 2.4: A horn structure used to efficiently excite a PGL mode from a CPW mode.[65]

(that generates a reflection) can be isolated. The pulse velocity between two features of a known separation is given by the formula $v = d/t$, where d is the separation between the features, and t is the time of flight (TOF). The measured value can then be used to calculate the effective permittivity using

$$\varepsilon_{eff} = (c/v)^2. \tag{2-4}$$

The substrates permittivity can be determined using

$$\varepsilon_s = 2\varepsilon_{eff} - \varepsilon_a\,, \tag{2-5}$$

where ε_a is the permittivity of the superstrate.

Information about the nature of a reflection in a time-domain system can be obtained from investigating the polarity of the pulse with reference to the initial pulse. A simple transmission line model with a termination is given in Figure 2.5. The polarity and magnitude of the reflection is given by the reflection coefficient

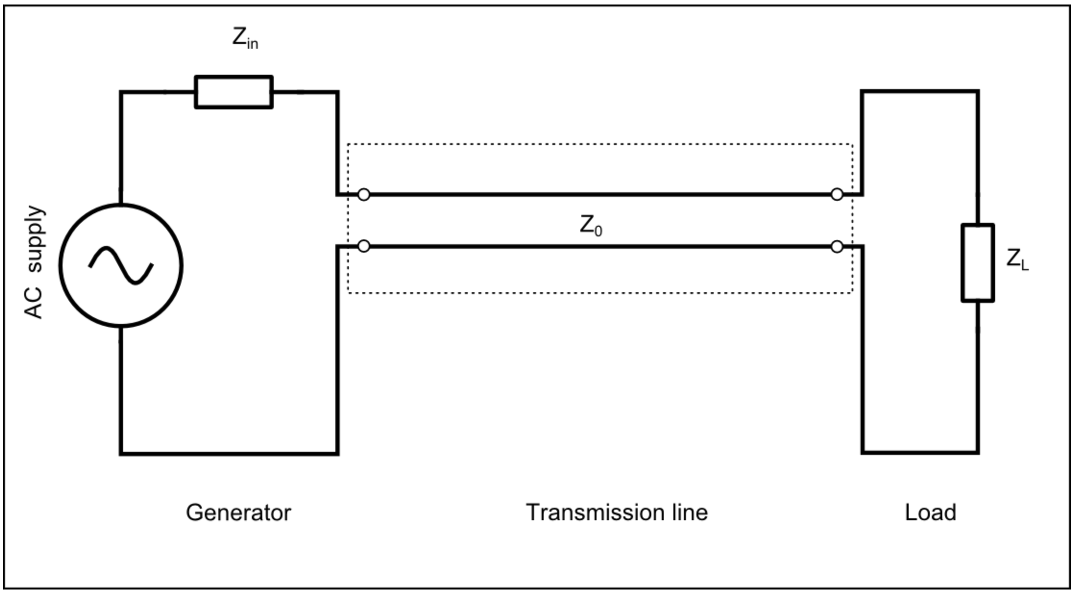

Figure 2.5: A simple transmission line model illustrating the three typical impedances that are encountered in a system, Z_{in}, Z_0 and Z_L. The two wire representation does not directly apply to a PGL, but the second wire can be considered to be the field that is in the surrounding dielectric/air. The load can be a short or open circuit, a change in the dielectric properties, or a change in the centre conductor properties.

$$\Gamma = \frac{V_0^-}{V_0^+} = \left(\frac{Z_L - Z_0}{Z_L + Z_0}\right)$$

(2-6)

For planar Goubau lines, the exact values of the characteristic impedance Z_0 and load impedance Z_L are difficult to calculate from theory due to single conductor geometry. However, this equation is still important for the analysis of experimental data, as the polarity and amplitude of a time-domain reflection can determine if the reflecting feature is open- or closed-circuit relative to the PGL.

The modes that propagate in PGLs are quasi-transverse magnetic (TM), where only the magnetic field is perpendicular to the direction of propagation, and it is unable to support propagation at lower frequencies. This makes PGLs a waveguide and not a transmission line (by definition). As the modes of waveguides are normally evaluated by solving Maxwell's equations for given boundary conditions (typically in circular or rectangular waveguides), this makes PGLs difficult to analyse accurately due to the lack of a defined boundary. Several attempts have been made analytically[69] but instead numerical simulation packages are often used with large (but finite) boundaries. As part of the mode propagates in the substrate and part in air,[69] shown in Figure 2.6, each medium propagates the electric field at different velocities. As each of the two fields interact, phase dispersion occurs and the bandwidth is reduced. Therefore, in order to obtain a large bandwidth the substrate is often chosen to have a permittivity as close to the superstrate as possible. Alternatively, with an air superstrate, the substrate can be thinned to a point where it has a reduced interaction with the electromagnetic field.[68]

The effects of varying the geometry of the single conductor with the surrounding fields have been investigated;[70] the findings suggest that decreasing the width of the

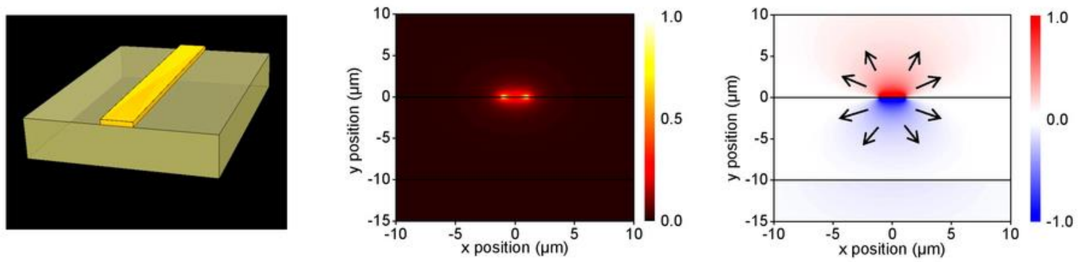

a) b) c)

Figure 2.6: Simulations of the PGL field by Gacemi *et al.* Ref 69. a) The rectangular PGL with a low refractive index ($n_{diel} = 1.46$) dielectric substrate and air superstrate. b) The power distribution in the cross section PGL, where y = 0 µm is the surface of the substrate. c) The electric field component of the PGL mode where the field is distributed evenly in the substrate and the air.

transmission line increases the normalised field confinement closer to the centre conductor. This is particularly useful when probing thin film materials such as graphene which are in contact with the waveguide as the field is confined to the single contact rather than distributed across two or three metal structures.

2.4 Graphene

2.4.1 Introduction

Graphene was first discussed theoretically[71] in 1947 and only much later discovered experimentally[72] in 2004, despite speculation that single atomic layers of crystals would not be thermally stable enough to observe.[73,74] In the following years, a great deal of interest has been sparked by its exceptional mechanical,[75] optical,[8] thermal,[76] magnetic[77] and electronic[78] properties, resulting in an almost exponential growth of publications investigating graphene. The experimental work presented in this thesis mainly covers fabrication and characterisation of terahertz graphene devices, where the following sections are intended to give a brief understanding of what makes it of interest to terahertz science, including the measurements and literature which have already been conducted in this area.

2.4.2 Methods for obtaining graphene

Before the properties of graphene are discussed, it is useful to have a basic understanding of how graphene can be obtained and prepared for experimental testing. There are several methods used to produce graphene films, each displaying various advantages and disadvantages depending on their application. The technique which accelerated graphene to widespread fame was the "scotch tape" method, which relies on the natural structure of highly oriented graphite; built from many parallel layers of graphene bonded together by van der Waals forces. When a sheet of graphite is split by pulling two flat faces apart with sticky tape, it will separate into two graphite sheets of arbitrary thickness. If this process is repeated many times (typically ~10) and then pressed onto a substrate, there is a likelihood that at some position on the substrate there is a single layer of graphene. However, there is a high level of skill required to conduct this process repeatedly, and to locate and identify the mono-layer graphene. This method is known to produce large, high quality crystals domains and is still typically used when very high carrier mobility is required.[7,79] The disadvantage of this method is that total graphene area is relatively small, where the largest flakes can range from 2,000 μm^2 to 1,500,000 μm^2.[80] These sizes are suitable for many scientific investigations, but are highly impractical for many of the proposed industrial applications (such as touch screen phones and microelectronic heat spreaders).

Graphene can also be obtained at wafer scale by epitaxially growing it directly onto single crystal SiC wafers.[81] This is prepared through controlled sublimation of the surface Si atoms leaving the C atoms to reconstruct a few-layer graphene structure. The processing procedure is more specialised than the exfoliation method as it requires temperatures up to 1700 °C and careful selection and preparation of the SiC wafer. It can, however, repeatedly produce large terraced channels (<10 μm) of graphene that are tens of microns long. The processing steps include heating an atomically clean SiC surface to temperatures in excess of 1500 °C in an argon atmosphere to thermally decompose approximately three bi-layers of SiC to produce one graphene layer.[82] The wafer is then slowly cooled to allow the carbon atoms to reassemble, where the first hexagonally structured carbon layer is covalently bonded to the SiC below and as such, does not behave as graphene. This has the advantage of seeding single-crystal like domains during subsequent layer formation that can behave similarly to mono-layer graphene, although they are formed from multi-layer sheets of graphene.[83] The resultant graphene layers have been shown to have a high mobility,[84] and the insulating substrate allows graphene devices to be formed directly, without any transfer process. Within the scope of this project, however, the large scale regions of graphene required and the availability was prohibitive for the epitaxial and exfoliated techniques.

Chemical vapour deposition (CVD) growth of graphene is a controllable method of producing up to 95 % coverage of monolayer graphene on copper catalysts.[85] Techniques have been developed for the subsequent transfer of this graphene onto arbitrary substrates.[20] After pre-annealing of the copper in a hydrogen atmosphere at ~1000 °C to remove oxide, clean the surface and crystallise the surface of the copper foil, a precursor (typically CH_4) is passed into the chamber which breaks down and seeds carbon to the copper surface. The system is then slowly cooled to allow the hexagonal graphene lattice to form on the surface. As copper is conductive it is not a suitable substrate for many graphene characterisation techniques and so it is typically etched away to allow the graphene to be transferred to a more suitable substrate (the complete recipe for this process is given in Section 3.1). Although a continuous film of graphene is typically produced, it is comprised of many smaller, rotationally disordered domains that range from sub-micron to 500 μm in size, and with carrier mobility up to 25,000 $cm^2V^{-1}s^{-1}$ on SiO_2 (at room temperature).[86] Additionally, small hexagonal nucleation points form, which are 5-10 layers thick in the centre and gradually thin outwards to form a single layer.[87] The size of these regions are typically controlled to be <1 μm, although they can continue to grow and merge into large polycrystalline films under certain growth parameters. The grain boundaries are expected to degrade both the electrical and mechanical properties of graphene.

For applications that require large single-crystal graphene regions, CVD grown graphene shows great potential[88] although mechanical exfoliation is currently the most suitable method for obtaining high mobility samples. However, in a practical sense, CVD graphene is perhaps the most promising method shown to date for growing large scale graphene for use in industry, where, for example 3.1 inch touch screens and even 30 inch conductive sheets have now been demonstrated.[20] The controllable, large area transfer and continuous conductance of the CVD grown graphene sheet were primary factors in the decision to use it for the work in this project. It is also commercially available, either on the Cu film (as was used here) or pre-transferred onto a number of substrates, making it very versatile in a research environment.

Graphene obtained by epitaxial growth, CVD growth and mechanical exfoliation are the most frequently used methods for electronic measurements, however, a number of other techniques are also being developed such as molecular beam epitaxy on SiC,[89] reduced graphene oxide[90] and solvent based sonication.[91] The applications of these materials vary from ultra-strong graphene-loaded-polymers to corrosion prevention spray coatings. However, many of these alternative methods are prone to poor connection from one sheet to another, small domain size, or have many defect sites, features that are typically not desired in electronic measurements.

2.4.3 Electronic properties of graphene

Graphene is a flat single-layer of hexagonally arranged carbon atoms which are covalently bonded to each other by hybridised sp^2-orbitals. These in-plane δ-bonds are formed by the superposition of a lower energy 2s-orbital with two higher 2p-orbitals, resulting in a total of three sp^2-orbitals and a single 2p-orbital which is perpendicular to the plane of the sheet. The δ-bonds are stronger than the C-C bonds in diamond and are responsible for graphene being incredibly strong and flexible, where the electrons are highly localised and do not contribute to conduction. The 2p-orbital orbitals, on the other hand, form weak π-bonds to the nearby atoms and are responsible for the electronic properties of graphene, forming π and π* bands, which are analogous to the valence and conduction bands respectively. The dispersion relation is typically calculated using a nearest neighbour tight-binding approach where the atomic separation is $a_0 = 1.42$ Å (ref.[92]), and each atom is arranged into two sub-lattices as shown in Figure 2.7 (a). The lattice constant $a = a_0\sqrt{3} = 2.46$ Å (ref.[93]) can be used to obtain the dispersion relation

$$E^{\pm}(k_x, k_x) = \pm\gamma_0 \sqrt{1 + 4\,cos\frac{\sqrt{3}k_x a}{2}\cos\frac{k_y a}{2} + 4\cos^2\frac{k_y a}{2}} \tag{2-7}$$

where γ_0 is the nearest neighbour hopping energy and the full band structure is shown in Figure 2.7 (b). The low energy cone shape of this band structure (<1 eV) occurs at the K (and K') points and gives rise to some very important electronic features of graphene. When Equation 2-7 is expanded around the **K** vectors at low energy, the dispersion relation can be given by

$$E^{\pm}(q) \approx \pm\hbar v_F|q|, \tag{2-8}$$

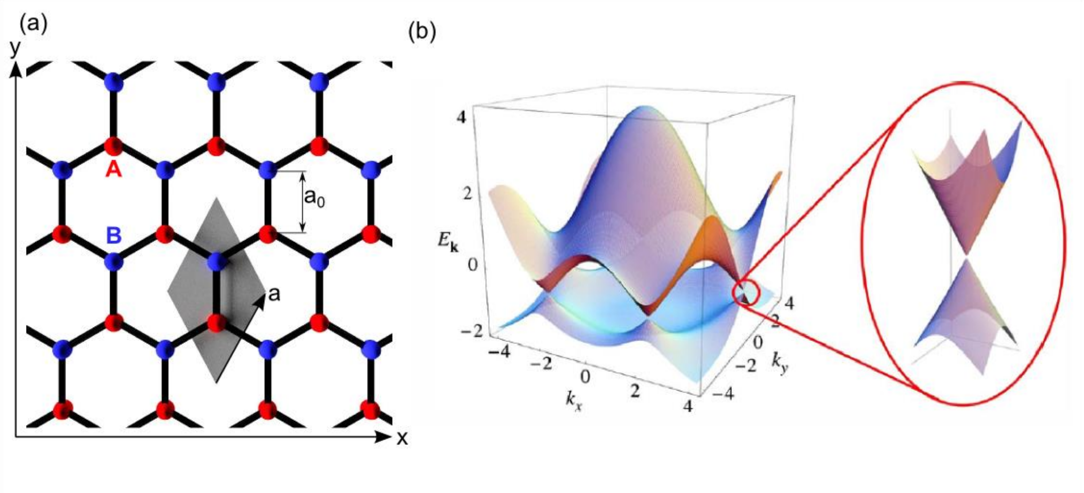

Figure 2.7: (a) The hexagonal lattice of graphene showing the key structural elements. A and B indicated the two sub-lattice assignments, *a_0* is the carbon-carbon spacing and *a* is the lattice constant. (b) The electronic dispersion in the honeycomb lattice with the linear, low-energy region shown to the right.

where v_F is the Fermi velocity and $q = (k_x, k_y) - \boldsymbol{K}$. This dispersion relation sets graphene apart from other semi-conductors because the band gap between the π and π* bands at the K points is 0 eV, meaning it can interact with very low energy photons (such as those at THz frequencies: ~0.4 meV to ~40 meV). The linear dispersion relation in the lower energy regime is also better described by the Dirac equation rather than the Schrödinger equation, and results in the carriers behaving similar to photons with a velocity $v_F \approx 1 \times 10^6\ m\ s^{-1}$.[71] Another point to note in the low energy region is that the conduction and the valence band are symmetrical around the 0 eV point, meaning that electrons and holes should, theoretically, have similar mobilities.[94]

The mobility of graphene is remarkably high at room temperature (in excess of 15,000 $cm^2V^{-1}s^{-1}$ on SiO_2 substrates[95]). The mobility is determined using the Drude model

$$\mu = \frac{\sigma}{ne},$$

(2-9)

where σ is the conductivity of the graphene sheet, and n is the carrier density. Experimentally, the value for mobility is often calculated by measuring the field effect in graphene transistors, where n is manipulated by applying a voltage, V_G, to a parallel conductive plane. This forms a parallel plate capacitor and allows control of the type (p or n) and the magnitude of carrier concentration, where the upper limit is typically limited by the voltage breakdown of the dielectric medium. The most frequently used configuration of this measurement is a graphene Hall bar geometry defined on a 300 nm SiO_2 oxide layer with a high conductivity Si substrate, where carrier concentrations from 2×10^{11} cm^{-2} to 4×10^{12} cm^{-2} can be obtained before the high electron regime is reached, and the mobility saturates.[96] Alternative configurations, such as using an ionic gel gate[14] or polymer doping,[97] can reach concentrations of ~1×10^{14} cm^{-2} owing to enhanced capacitive coupling. The high surface area of graphene also makes it very susceptible to alteration of its carrier concentration by a number of factors, including: the substrate,[7] residues of the fabrication process, or factors such as environmental gasses.[98] The dopant concentration can be evaluated by

$$n_s = \frac{\epsilon_0 \epsilon}{te} |V_G - V_{Dirac}|$$

(2-10)

where ϵ_0 is the permittivity of free space, ϵ is the relative permittivity, t is the dielectric thickness and V_{Dirac} is the location of the conductivity minima. There are a number of ways to alter this dopant concentration to meet the needs of an experiment. Intrinsically doped graphene is typically achieved by annealing in a vacuum using either external heating elements,[79] or by passing large current densities through the sheet.[79] The doping can similarly be changed by treating the surface of the graphene with vapour,[99] polymers[100] or other materials.

External doping of graphene is relevant to this project since the tested devices incorporated a polymer superstrate to support the graphene structurally. Earlier investigations into polymer doping mainly focussed on how carrier mobility could be improved by removing the residues, such as PMMA, after the fabrication process.[101] However, it was later realised that some polymers such as poly(4-vinylpyridine) (P4VP) and SU8 could be used to provide p- and n-type doping, for the purpose of creating more efficient active devices.[102] As the interaction of H_2O with graphene can cause undesired fluctuations to its performance, great effort is often put into removing water before, and during, testing by annealing and/or using ultra high vacuum environments. When this is not practical, a thick polymer coating may be considered to stabilise the carrier concentration. The mechanism by which the carrier concentration is changed has been studied in detail for a number of gasses and even PMMA[101] due to its frequent use in the processing of graphene devices.

Novolac based positive photoresist Shipley 1813 (S1813) is less frequently used in comparison to PMMA and there have been few investigations reporting its interaction with graphene. One study observed that the graphene carrier concentration increased from 1.1×10^{13} cm^{-2} to 1.8×10^{13} cm^{-2} when UV exposed S1813 covered the graphene.[103] As S1813 is very thin (typically ~1 μm), the conditions of the graphene underneath are expected to be very stable. Hence, S1813 doped graphene is used throughout this thesis to enable consistent graphene doping levels, as well as providing good structural support.

2.4.4 Terahertz properties of graphene

The terahertz and far-infrared (up to ~100 THz) conductivity of graphene is determined by intraband transitions and can be described by the Drude model. The Drude model assumes that the electrons act as particles with kinetic mechanics and travel through a system with fixed ionic scattering locations. The particles can move through the system under the influence of Lorentz forces to produce current flow. The probability an electron will scatter in the time δt is given by $\delta t/\tau$, where τ is the electron scattering time and, in the absence of external forces, the momentum of the system decays exponentially

$$p(t) = p_0\, e^{-t/\tau}.$$

(2-11)

It is apparent that the time dependence of Drude model will lead to a frequency dependent behaviour in the conductivity of the system. For a time dependent electric field $E(t) = E_0 e^{-j\omega t}$ and the corresponding time dependence of the momentum $\mathrm{p}(t) = p_0 e^{-j\omega t}$, the equation of motion

$$\frac{dp}{dt} = -\frac{p(t)}{\tau} - eE,$$

(2-12)

becomes

$$-j\omega p_0 = -\frac{p_0}{\tau} - eE_0.$$

(2-13)

Since the current density is $J = -nep/m^*$ (n, number of electrons. m^*, effective mass), and Ohms law is $J = \sigma E$, the conductivity is therefore

$$\sigma(\omega) = \frac{ne^2\tau/m^*}{1 - j\omega t}.$$

(2-14)

This is often also expressed as

$$\sigma(\omega) = \frac{\sigma_{DC}}{1 - j\omega t} \quad \text{or} \quad \sigma(\omega) = \frac{jD}{\pi(\omega + j\Gamma)},$$

(2-15)

where $\sigma_{DC} = ne^2\tau/m^*$ is the DC conductivity, and $D = \pi ne^2/m^*$ is the Drude weight for classical materials. The effective mass is a descriptive metric that is used to relate the true mass of the electrons to the measured motion of the electrons to an external Lorentz force. The commonly used definition of effective mass results in a diverging value as it assumes a parabolic dispersion relation, found in many semiconductors. The relativistic charge carriers in graphene have a linear dispersion relation, which would imply a zero rest mass. However, the effective mass of the electron under a perpendicular magnetic field, or the cyclotron effective mass, is non-zero. Novoselov *et al* experimentally obtained the effective mass to be $m^* = \sqrt{\pi\hbar^2 n/v_F^2}$, where v_F is the Fermi velocity.[77,95] This results in a Drude weight of

$$D = \frac{v_F e^2}{\hbar}\sqrt{\pi|n|}.$$

(2-16)

An increased optical absorption is expected in graphene at the terahertz frequency range due to Drude absorption as shown in Figure 2.8,[21] where the optical conductivity is dominated by intraband carrier dynamics (as opposed to interband at optical and UV frequencies). The techniques that can measure the Drude response are limited by the availability of technology that can reliably measure broadband terahertz radiation. Fourier transform infrared (FTIR) spectroscopy has been used to find the transmission spectrum which was discovered to be Drude-like,[21–23] but can vary from the theoretical value by up to 45 % at higher values of n, where the lower carrier density regime was found to have a conductivity independent of n. The deviation from the expected values was speculated to be a result of the electron-electron and electron-impurity interactions that are neglected in the Boltzmann transport theory.[23]

Studies with FS-THz-TDS systems on the other hand observed a flat response even though the measurements were taken at much lower frequencies than the Drude roll-off observed in the FTIR systems.[104] An investigation into the dependence of carrier concentration found that the conductivity of the entire band (0 to 1.5 THz) shifted as predicted by the Drude model and was proportional to $\sqrt{n}$.[25]

In transmission spectroscopy, a highly conductive substrate is often used to control the gate bias; this is only one of a few methods for changing the properties of the graphene, as discussed in Section 2.4.3. One method that was not mentioned before is optical pumping, where carriers can be pumped into excited states for very short periods of time.[105] Optical-pump terahertz-probe measurements are modified FS-THz-TDS systems that incorporate an additional beam path which optically excites the graphene at a similar time range to a terahertz field passing through it.[12,13,26] The beam causes interband transitions and temporarily changes the conductivity of the graphene sheet which can be measured without electrical contacts by changes in the THz pulse transmission at that location. Although the entire pulse can be measured for a range of excitation times, if the change in amplitude is uniform for all frequencies, only the amplitude needs to be measured. This drastically improves the speed of the scan and provides information on the rates of optical excitation and relaxation of the carriers. Using these methods the carrier dynamics have been found to change with the number of graphene layers and even with different environmental gasses.[106]

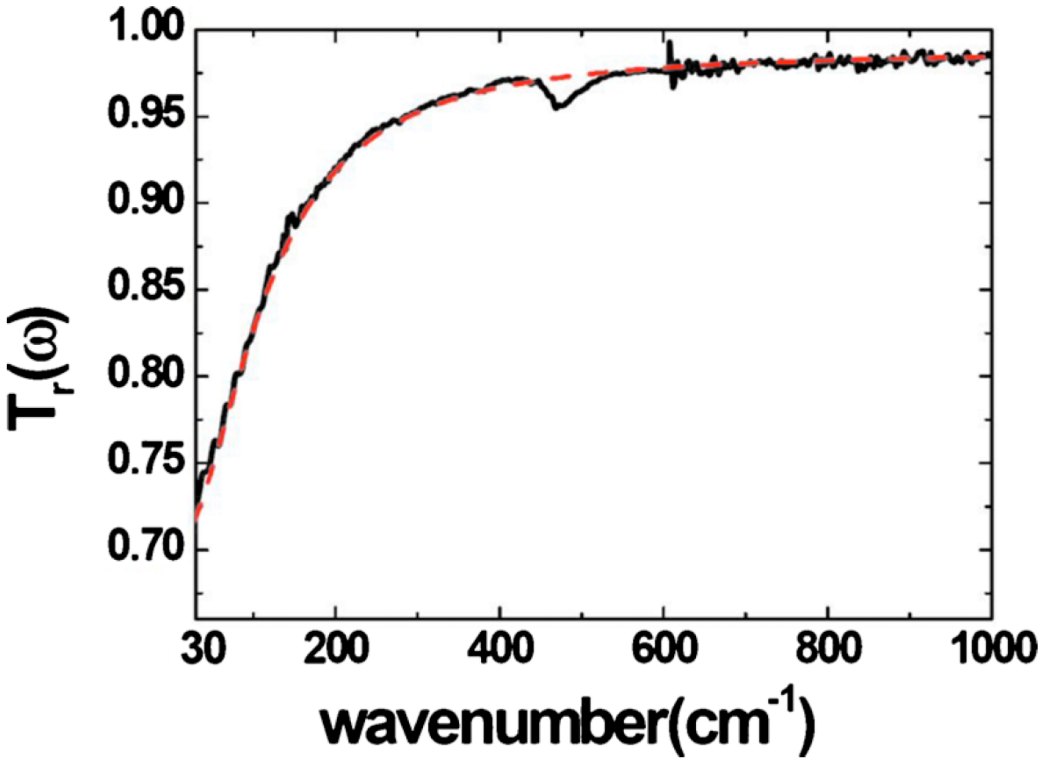

Figure 2.8: The transmission of far infrared through a mono-layer of graphene. The lower frequency response is characteristic of a Drude absorption, and at higher wavenumbers the response is dominated by the interband optical response (see Section 2.4.5). Figure from Ref 21.

The absorption of terahertz radiation into graphene can be further increased by excitation of intrinsic plasmon modes in the graphene.[28] Plasmons are collective charge density oscillations that are caused by the overshooting of the electron position under the influence of a charge disturbance, where the returning force results in a weakly damped oscillation. The interaction of adjacent electrons causes a hydrodynamic wave-like propagation the frequency of which is determined by the carrier density of the graphene. Coupling of infra-red and THz radiation to excite the plasmon modes in graphene requires meta-material formation by using graphene disks or ribbons. With graphene micro ribbons, absorption of up to 13 % has been observed in the region of 1-4 THz, which for a monolayer of atoms is quite extraordinary.[14] Plasmons are typically very lossy compared to EM waveguide propagation, but the Dirac plasmon propagation in graphene is more efficient than its classical semiconductor counterpart.[15] They also have the advantage of confining the signal up to 40 times more than free space,[107] making them potentially very useful in the future of chip-integrated terahertz frequency optoelectronics.

Most current experimental research at terahertz frequencies on graphene is performed by measuring the pulse propagation perpendicular to the plane of the material, owing to the opportunity to use existing FS-THz-TDS or FTIR systems and place the graphene sample in the beam path. However, there have been publications which investigate the coupling of millimetre-wave radiation parallel to the graphene and coupled to waveguides, similar to the configuration that is used in Chapter 4. Single wire graphene transmission lines have been investigated up to 40 GHz with very high mobility samples (110,000 $cm^2V^{-1}s^{-1}$) to reveal a carrier concentration controllable attenuation by means of controlling the kinetic inductance.[108] CVD grown graphene transmission lines have been tested at frequencies up to 110 GHz at room temperature, where negligible kinetic inductance was reported along with insignificant skin depth, and suggesting that monolayer graphene may be used as a broadband resistive element in mm-wave circuits.[33,109]

Beyond the frequency response of graphene transmission lines, plasmons in graphene have also been observed in the tens of GHz range. Petkovic *et al* used a dual channel time-domain reflectometry module to excite a graphene oval from an input transmission line as shown in Figure 2.9 and was detected with a perpendicular transmission line to reduce cross talk.[34] The step input signal to the graphene was capacitively coupled to the "output" resulting in a differentiated, peak-like signal. The signal from the wires and transmission lines were subtracted by modulating a current through the graphene. This caused a change in the edge density, where the measurement isolated only the signal that was affected by the change in graphene properties. The key investigation of this work was the study of the dynamics of magnetoplasmons (plasmons under the influence of a magnetic field), where the Lorentz force on the electron liquid could guide the

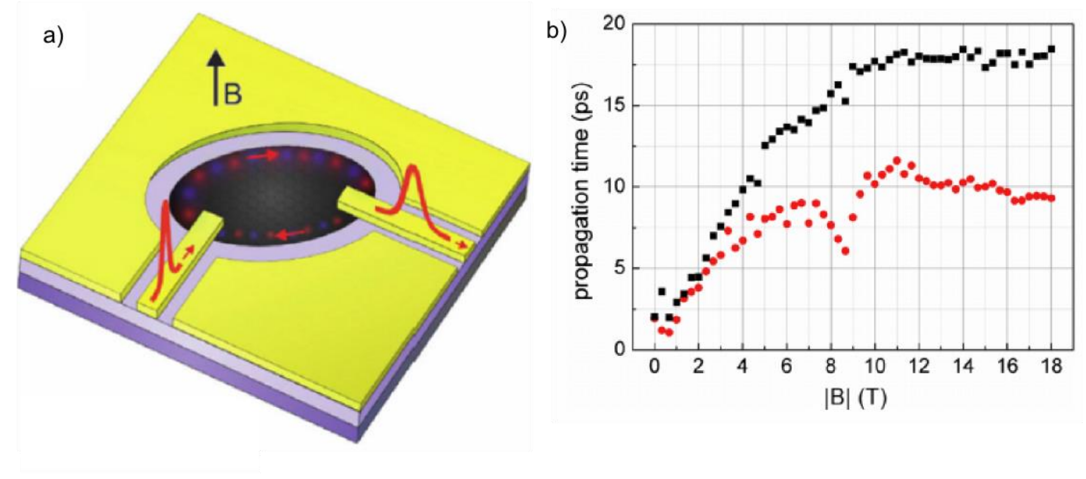

Figure 2.9: The schematic layout used to test edge-magnetoplasmons that are excited by step-like excitations on the left and detected as pulses on the right. The direction of the magnetic field can change the propagation of the pulse to be clockwise or anticlockwise around the edge.[34]

propagation of the plasmon wave around the inner or outer edge, depending on the magnetic field polarity. This is particularly relevant, since magnetoplasmon research was considered as a future development to the work presented in Chapter 4.

2.4.5 Optical properties of graphene

Graphene has a universal optical conductivity of $e^2/4\hbar$, corresponding to a wideband optical absorption of $\pi\alpha$, even for energies which extend beyond that of the estimated linear energy range (~1 eV).[8] When investigating the optical transparency, Nair *et al* discussed that "the fine structure constant can so directly be assessed practically by the naked eye",[8] where the experiment resolved a 2.3 % absorbance per monolayer of graphene. The influence of the interband transitions on the electrical properties of a single atomic layer has many promising photonic applications. These include tuning the absorption wavelength through Pauli blocking, and solar cells that outperform similar-thickness Si based devices.[110]

Graphene photodetectors could be considered to be an unusual topic of research as the gapless nature means that on-off ratios are very small when they are operated with the same principals as semiconductor photodetectors.[72] Where, under bias, large currents are generated. However, it was found that the doping by metal contacts created a p-n junction at the graphene/metal interface, which produced a photocurrent upon illumination.[111] This effect means that a source-drain bias does not need to be applied to measure optical fields, resulting in zero shot noise from the detector. It was found that the optical energy had to be focussed onto single graphene/metal interfaces as the photovoltage from a two terminal device would cancel out. Improvements to graphene photodetectors were achieved by using different work function metals for the source, and drain contacts.[112,113] This increased the photoresponsivity of the devices, meaning that in practical applications the devices would not be as sensitive to misalignment.

The mechanism by which the photovoltage is produced has been attributed to the photo-thermoelectric (PTE) effect.[114] At graphene p-n junctions the PTE effect, and inner photoelectric effect (found in semiconductor photodiodes), have both been considered, but studies have revealed that the PTE effect is dominant and describes graphene photovoltage very accurately.[9] The experimental method that was used to test the contribution of each was to observe the photoresponse amplitude as a function of polarisation. Whilst the PTE is only based on illumination power; the inner photoelectric effect is most efficient when the optical field is polarised perpendicular to the junction. Illumination of a doped graphene sheet results in hot-carriers as a result of the low dimensionality, gapless band structure and weak acoustic phonon coupling.[115] In doped graphene, photoexcited carriers collide with each other in the first ~100 fs and produce hot carriers.[116] This is when the electron temperature becomes out of equilibrium from the lattice and these local, thermalized carriers diffuse into cooler areas according to the Seebeck equation

$$S = \frac{2\pi^2 k_B T_{el}}{3eT_F},$$

(2-17)

where k_B is Boltmann's constant, T_{el} is the electron temperature, and T_F is the Fermi temperature (where $E_F = k_B T_F$).

On a plane sheet of graphene, hot carriers distribute equally in all directions and result in zero net current flow.[115] However, at a graphene metal interface, the graphene in contact with the metal has a different T_F than the graphene in the surrounding region and results in a net flow of electrons in one direction. The PTE voltage is given by

$$V_{PTE} = (S_2 - S_1)\left(T_{el,hot} - T_{el,0}\right),$$

(2-18)

where S_1 and S_2 are the Seebeck coefficients for the graphene on the metal and the graphene on the quartz respectively, $T_{el,hot}$ is the photoexcited electron temperature, and $T_{el,0}$is the temperature before excitation. The carriers eventually cool to equilibrium, mainly due to acoustic phonon emission or by optical phonon emission above 200 meV.[9,10] In the experiments that discuss the cooling of hot-carriers, metal/graphene contacts on SiO_2 are used to generate substantial photovoltages with relaxation times up to 100s of picoseconds.[40] These picosecond time-scale carrier dynamics are important factors for the measurements throughout this thesis, but the generation of photovoltages at metal/graphene interfaces are particularly important in Chapter 6 as these mechanisms are used to generate few-picosecond transient currents.

Chapter 3: Fabrication and characterisation

3.1 Fabrication of on-chip terahertz devices

The fabrication steps described in this section were applied to all devices described in this thesis. This processing regime was arrived at by several iterative improvements to existing techniques that had been previously developed, both for on-chip terahertz time-domain spectroscopy (OC-THz-TDS) devices, and for graphene devices.[70,117] The LT-GaAs transfer process was based on early epitaxial GaAs transfer methods,[118] that were subsequently developed for the specific epitaxial wafer structure.[70] Further development of this technique were required in order to fully remove thin LT-GaAs residues that were not entirely removed during the etching process, which would otherwise interfere with the graphene layer. The graphene transfer process was adapted from established techniques for monolayer CVD graphene grown on Cu,[119] and was developed further to remove the unwanted graphene on the backside of the Cu. These methods were adapted to transfer the graphene over metal contacts (up to ~100 nm thick) so that if the graphene sheet was found to be defective between the metal contacts, it could easily be etched away so that new graphene could be transferred.

The final device structure required the following sequential steps: (i) epitaxial transfer of low temperature grown gallium arsenide (LT-GaAs) onto quartz, (ii) etching of the LT-GaAs, (iii) fabrication of metal planar Goubau lines (PGL) and switches, (iv) transfer of CVD grown graphene onto the quartz, and finally (iv) etching graphene into the desired shape. Other device structures which required transfer of the graphene before the metal step were also attempted, but it was found that adhesion in the quartz/graphene/metal stack was poor, and often led to delamination. The was because the transferred LT-GaAs could be removed by using ultrasonic cleaning or strong solvents, hence, the quartz surface could not be prepared using the same techniques that are suggested in the literature.

Low-temperature-grown GaAs (LT-GaAs) was grown (at 180 °C) using molecular beam epitaxy (MBE) on a 500-μm-thick semi-insulating GaAs (SI-GaAs) substrate. The growth consisted of a sacrificial 100-nm-thick layer of AlAs, followed by a layer of 350-nm-thick LT-GaAs. This wafer was cleaved into 3 mm × 4 mm chip sizes, and cleaned; first for 5 minutes in acetone, and then isopropanol (IPA) in an ultrasonic bath, and oxygen plasma ashed. It was annealed at 575 °C for 15 min in a rapid thermal annealer to give an optimal dark resistance and carrier lifetime in the LT-GaAs layer. Using epitaxial lift-off techniques,[120] the LT-GaAs was removed from the SI-GaAs, using Apiezon wax as a temporary host superstrate whilst the sacrificial AlAs layer was etched away. To do this, the MBE structure was placed onto a hot plate at 130 °C. Apiezon wax was then placed onto the surface to melt until the top of the chip was covered, and then the sample was then left to cool. Trichloroethylene-soaked swabs were used to rub away the outer edge of the wax, exposing about ~0.5 mm of the LT-GaAs surface around the perimeter. When submerged in a solution of H_2SO_4:H_2O_2:H_2O (1:40:80 by volume) for 1 min, the unprotected LT-GaAs was removed, exposing the AlAs. The sample was then rinsed in deionised (DI) water and placed in a 10 % by volume solution of HF acid (at –4 °C to ensure a low etch rate). The slow etch rate was required to limit the size of hydrogen bubbles in the interface between the two layers of GaAs, which otherwise were found to cause micro-cracks in the transferred layer. The chip was then separated into two; the thin layer of LT-GaAs attached to the wax, and the SI-GaAs host substrate. The latter could then be discarded. The LT-GaAs was rinsed several times in water and placed onto the cleaned quartz host substrate, ensuring that a small film of water supported the LT-GaAs and the wax. The sample was then left to dry for 4 to 5 days, allowing Van der Waals bonding to take place.

After bonding, the stack was placed in trichloroethylene until all wax was removed, leaving only the ~2 mm × 3 mm piece of photoconductive material on the much larger quartz substrate. A further rinse in trichloroethylene ensured that no wax film remained, and then the sample was gently rinsed in DI water and dried. To desorb any particles trapped at the quartz/GaAs interface, the sample was then placed into a vacuum oven for 15 hours at 250 °C to further enhance the bond between the LT-GaAs and the quartz.

To etch the GaAs, photolithography was used to protect the desired switch region. Shipley S1813 was spun onto the device at 4000 RPM and soft-baked for three minutes at 115 °C to obtain a ~1.3-μm-thick layer. A Karl Suss MJB3 mask aligner was then used to define the switch pattern in the resist (two seconds exposure and subsequent immersion in Microposit MF319 developer for 40 seconds). The sample was then, rinsed in DI water and dried. A ~10 min H_2SO_4:H_2O_2:H_2O (1:8:950 by volume) etch was then used for to remove the excess LT-GaAs. The slow etch rate was used to provide a ramped edge profile on the 350-nm-thick LT-GaAs so that open circuits were not formed on the 80-nm-thick metal PGL film. Some small LT-GaAs residue was often left over after etching, and required agitation from a syringe needle or cotton swab to fully remove unwanted areas. The resist was then stripped by rinsing in acetone, IPA and water. The remaining resist residues were removed in an O_2 plasma asher (5 minutes at 50 W). The sample was placed on a hot plate for 10 min at 200 °C to desorb any residual liquid. Note that the devices could not be placed into an ultrasonic bath due to the fragility of the LT-GaAs/quartz bond after Van der Waals bonding.

To define the planar Goubau line and probe arms, bi-layer photolithography was used to obtain a uniform metal profile, which allowed easier metal lift-off in comparison to single layer photolithographic processing. A primer (hexamethyldisilazane) was used to enhance adhesion to the quartz; after application to the device surface, it was spun at 2000 RPM for 30 seconds, and then baked at 200 °C on a hot plate for 1 minute. It was then rinsed in IPA to remove excess primer, and baked for a further 5 minutes at 200 °C to desorb moisture from the surface. The device was immediately transferred to a spinner where Microchem LOR 3A was applied as the base of the bi-layer resist and was spun at 2000 RPM for 40 seconds and baked at 200 °C for 5 minutes to obtain a ~400-nm-thick layer. Shipley S1813 was applied above the LOR and spun at 4000 RPM for 40 seconds and subsequently baked at 115 °C for 3 minutes. The thick edge beads were removed using a scalpel blade to allow optimal contact to the photo-mask, which resulted in more accurate feature replication from the mask to the device. The device/mask was exposed for 2 seconds and then developed in MF319 for 1 minute 30 seconds. These parameters were found to result in an undercut of the LOR by slightly less than 1 μm, determined by optical microscopy. This was followed by a plasma ash descum and metal deposition of 5-nm-thick titanium and 80-nm-thick gold layers was performed using a Leybold Univex 350 electron-beam evaporator at pressures below 1×10^{6} mBar, which was subsequently lifted off using acetone and MF319.

CVD grown graphene on copper (purchased from Graphene Square, Korea) was prepared by spinning on a 600-nm-thick supporting layer of PMMA and subsequently baked at 200 °C for 2 min. The graphene on the backside of the copper was then removed using a reactive ion etch with 15 sccm flow of O_2 for 30 s and 80 W power. The sample was then placed copper-side down on top of a solution of $FeNO_3$ and DI water (0.01 g/ml concentration), so that the sample was floating on the surface. Once all copper had been etched away, leaving a suspended stack of graphene and PMMA, the stack was lifted from the surface of the solution using quartz and transferred onto the meniscus of a DI water bath. This step was repeated several times using fresh water until any residual $FeNO_3$ had been sufficiently diluted. The previously prepared quartz substrate with GaAs was then cleaned in acetone and IPA for 5 minutes each, oxygen plasma ashed until hydrophilic, and was then used to lift out the graphene/PMMA stack from the water. The stack, floating on a thin film of water on top of the device, was then gently manipulated into the desired position between the two GaAs stripes and left to dry overnight in ambient conditions, thereby bonding the graphene to the quartz/gold. The sample was then placed on a hot plate at 200 °C for 5 min to soften the PMMA and reduce any wrinkles that had formed during the drying process. Afterwards the PMMA was removed using an acetone bath for at least 1 hour and then rinsed in IPA. A further heating step at 200 °C for 10 min was then used. A final step of standard optical lithography was used to mask the desired graphene regions during a plasma ash. The S1813 was left on after the ashing to support the graphene structurally at the edges of the metal.

3.2 On-chip terahertz time-domain spectroscopy

The functional principal of THz-TDS systems is to take a coherent pulsed laser source (typically < 200 fs), split the beam in two, and to then control the delay time of one beam with respect to the other at a given location. One of the beams (pump beam) is used to excite an emission source, producing a single-cycle pulse of THz-frequency electromagnetic radiation, which is guided towards a detector, arriving at a time t_0. If the second beam (probe beam) arrives at the detector and samples the THz pulse, a measureable signal I_{max} can be detected. However, if the second beam is scanned above and below the arrival time $t = t_0 + \delta t$ for many pulse emissions from the laser, then a graph of I_{pulse} with respect to t will allow a reconstruction of the shape of the THz pulse in the time-domain. This section will describe the operation of the system that was used to characterise device in Chapters 4, 5 and part of Chapter 6.

3.2.1 System description

The Spectra Physics "Tsunami" mode-locked Ti:Sapphire laser system was pumped by a Spectra Physics "Millennia Xs" laser with 10 W of 532 nm wavelength continuous wave emission. The Tsunami output laser pulses are 110 fs long, centred at a wavelength of 790 nm and with a pulse repetition rate of 80 MHz. The average output power of the laser was 700 mW, where the total power available to the OC-THz-TDS system (as shown in Figure 3.1) was ~50 mW. The beam was first split into two beams of equal power, where the path length from the splitter to the device under test (DUT) was approximately the same. Each beam path contained NIR ultrafast mirrors to guide

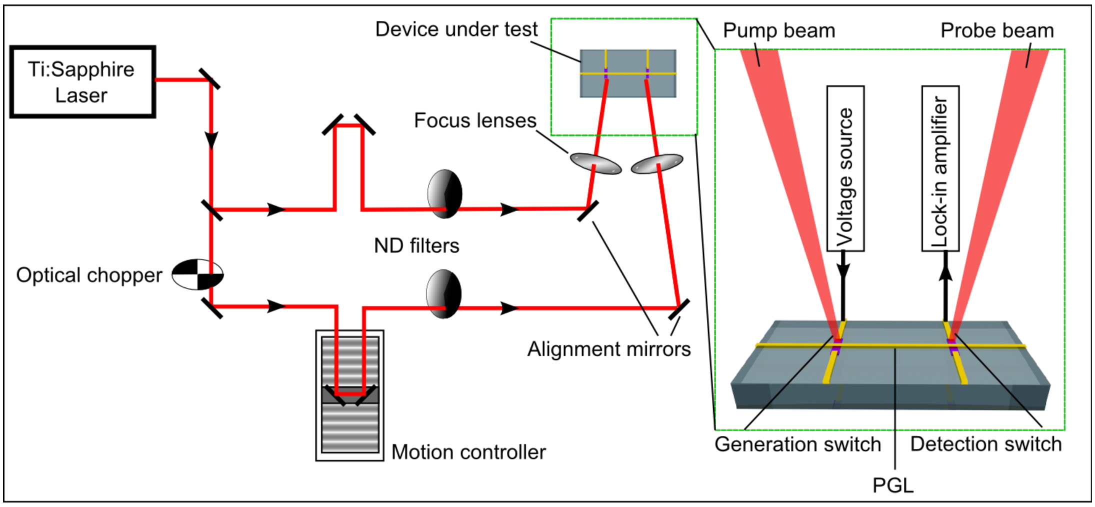

Figure 3.1: Schematic diagram of the on-chip THz-TDS system.

the beam and one variable neutral density filter to control intensity. The probe beam also contained a mechanical optical chopper that was operated between 2 kHz and 3 kHz, and a 180-mm-long delay stage containing a retro-reflector, which was used to delay or advance the probe pulse arrival time. Each beam was focussed onto the surface of the device using either a 10 cm focal length lens or a 10× NIR microscope objective with a 3.5 cm focal length. The spot size of each lens was measured using knife-edge measurement techniques, revealing Gaussian FWHM spot sizes of 24 μm (10 cm lens) and 5.5 μm (3.5 cm lens).

The bias voltages to the device were supplied by a Keithley 2400 series source-meter which also allowed current-voltage measurements for characterisation of the switches. The photocurrent signal, $I_{pulse,}$ was measured by a Signal Recovery 7265 lock-in amplifier and synchronised to the mechanical probe beam chopper. For the time-domain scans, a buffer was allocated in the lock-in amplifiers memory and the measurements were taken when a trigger signal from the motion controller indicated the stage had arrived at a pre-defined position. This increased the speed at which the measurements could be taken. The LabVIEW control software communicated with the lock-in amplifier and source-meter using the GBIP interface, and with the motion controller through an Ethernet network connection. Before each set of measurements, the lock-in was calibrated using the “auto phase” function to synchronise to the chopper, using the peak signal from the THz pulse as a reference.

3.2.2 Current-voltage measurements

Each beam was focussed onto an LT-GaAs switch biased at 10 V and was aligned to the produce maximum photocurrent readout on the source-meter. An efficient photoconductive switch would typically show very low conductivity with no illumination (~0.1 nS), but a high conductivity when illuminated by the 780 nm beam (~100 nS). However, the nature of LT-GaAs is not just to produce pulses efficiently, but also to extinguish carriers very quickly so that short carrier lifetimes can be achieved. For the material grown in this work, this trade-off between efficiency and carrier lifetime is controlled with the post-growth anneal temperature, although it is possible to anneal the material during the MBE growth cycle). This was desirable as it allowed flexibility in the annealing process to optimise the material performance. The growth of LT-GaAs by MBE is complicated by difficulties in taking exact temperature readings during growth, which results in wafer-to-wafer changes in properties. Ideally, the post-growth anneal temperature should be calibrated for each new wafer in order to obtain the best performance.

To demonstrate the optimisation process, six devices, each with switch regions 30-μm-wide and 5-μm-long, were fabricated directly onto 2-μm-thick LT-GaAs that was annealed at a range of temperatures. These devices are discussed in the following section of this chapter, where the current resulting from applied voltage (I-V) sweeps is discussed first.

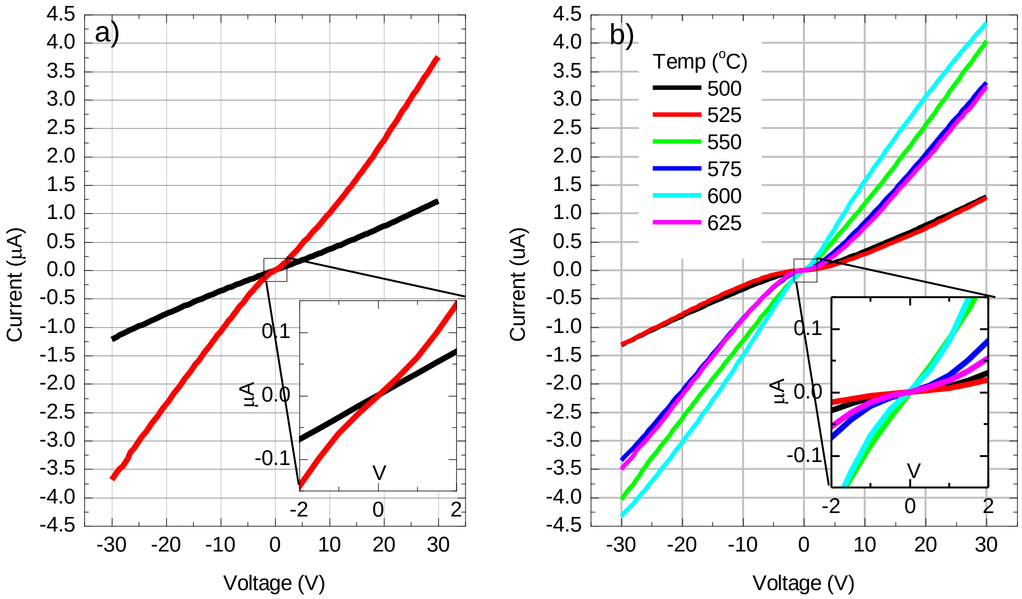

Figure 3.2: Voltage sweeps performed on six devices that were annealed at incremental temperatures measured with a 10 cm objective lens. (a) The dark (0 mW laser power, black line) and light (10 mW, red line) photocurrent produced during a voltage sweep for the 550 °C device where the inset shows the slightly non-linear region between -2 V and 2 V. (b) The voltage sweeps for each device at 10 mW laser illumination.

Figure 3.2 (a) shows the difference between illuminated and dark conditions for an anneal temperature 550 °C. A linear relationship between the voltage and current is ideal since it indicates good Ohmic contact between the gold and LT-GaAs. This is also good as, when operating as a detection switch, the magnitude of the field is linearly converted into current. However, the linear regime is only applicable above voltages of 2 V, while a Schottky response is seen for lower voltages. An I-V sweep for each of the post-growth anneal temperatures is shown in Figure 3.2 (b), where it can be observed that this Schottky response varies across all the devices. Specifically, 500 °C and 525 °C have the most pronounced Schottky response at low voltages, and the 550 °C and 600 °C devices show almost perfect Ohmic response.

It can be seen in Figure 3.2 (b) that the incremental anneal temperatures did not produce a very clear trend in the photoresponse of the material. The data shown was the average values from four separate switches on each device (except for the 600 °C device where only two switches were functional). The standard deviation (not shown) of each individual device did not exceed ±15 %, which indicated that switches on the same devices performed similarly, but also that differences occurred during the fabrication of each device that affected the switch characteristics. This is especially true for LT-GaAs that has been transferred using epitaxial lift-off, as micro-cracking can occur. If both the dark current and illuminated current are taken into consideration and formed into a ratio of the two values (shown in Table 3.1), a trend can be seen. The illuminated current varies only slightly between the devices, however, at 575 °C the dark current drops by more than two orders of magnitude leading to much larger ratios and much better signal levels.

Table 3.1: Photoconductive properties of LT-GaAs at various anneal temperatures.

Temperature (°C)	Dark current at 30 V (µA)	Current 10 mW and 30 V (µA)	Ratio
500	0.28392	1.29889	4.57488
525	0.02528	1.27975	50.62787
550	1.7805	4.03929	2.26862
575	2.44321E-4	3.30172	13513.87549
600	1.86652E-4	4.34916	23300.91735
625	3.45076E-4	3.23719	9381.0896

All of the variables discussed here, and in the following sections, are key in selecting the right anneal temperature for a given material wafer.

3.2.3 Autocorrelation measurements

The experimental setup for conducting autocorrelation measurements was adapted from the OC-THz-TDS configuration described in Section 3.2.1, where two beams were instead focussed onto a single switch using two 10 cm focal length lenses. Both beams were individually aligned to overlap spatially on the switch, corresponding to the maximum measured photocurrent at a switch bias of 30 V. Some asymmetry was noticed in a number of the measurements, which was attributed to slight misalignment of one of the beams. Although slight adjustments were made to minimise this whenever possible, a small degree of asymmetry is unavoidable owing to the approach angle of each beam. The beams were cross-polarised using quarter-wave-plates (QWP) to prevent coherent interaction of the laser beams.[121] The lock-in amplifier was connected to one of the two switch contacts via a transformer. This blocked the DC component of the signal, only allowing the chopped (or difference) signal to the input of the lock-in amplifier. This was important as the maximum specified input for the model “7265” lock-in amplifier was

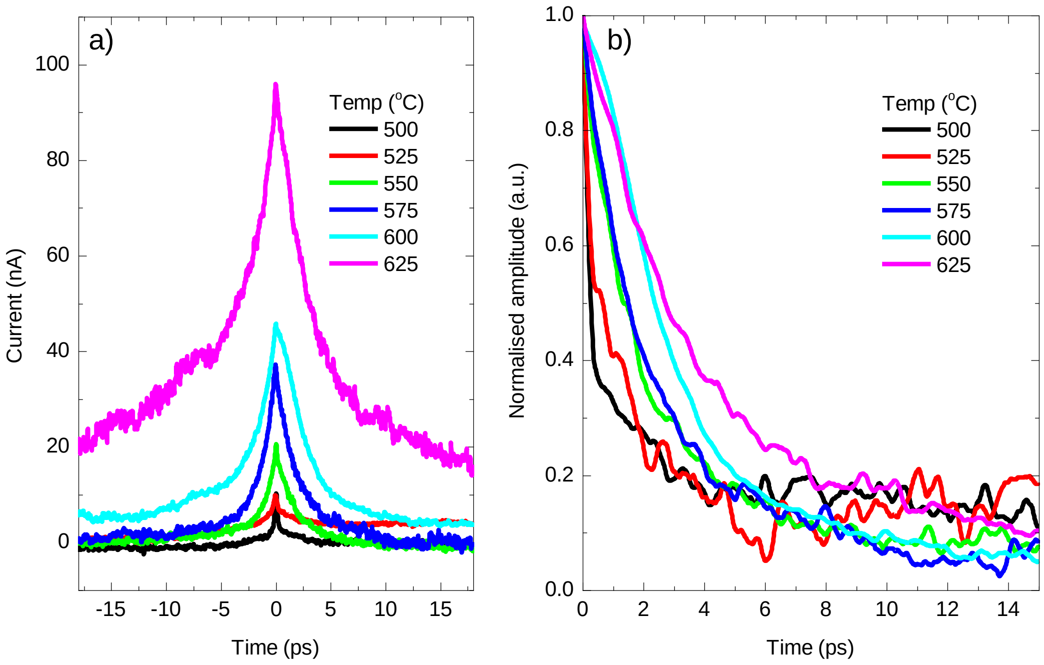

Figure 3.3: Autocorrelation measurements conducted on devices with a range of anneal temperatures at 30 V bias and 10 mW power on each beam. (a) The measurement of each device anneal temperature. A slight asymmetry can be seen on some measurements, due to small differences in the angles of incidence of each beam. (b) Each of the anneal temperatures normalised and plotted from 0 ps to 15 ps.

Table 3.2: Comparison of the carrier lifetimes for each anneal temperature.

Anneal temperature	500 °C	525 °C	550 °C	575 °C	600 °C	625 °C
Carrier lifetime	0.50 ps	1.46 ps	2.00 ps	2.33 ps	3.21 ps	4.01 ps

3 μA. At low bias voltages, insertion of the transformer did not alter the signal measurement values or attenuate the signal at the chosen chopper frequency.

The same six devices discussed in Section 3.2.2 were tested using the autocorrelation measurement configuration. The raw results, taken from an individual switch on each device, are shown in Figure 3.3 (a). These demonstrate that both the amplitude, and width, of the central feature increase with anneal temperature. The amplitude of each measurement provides information about the saturation level observed at the switch e.g. the relative number of carriers that are initially photoexcited by the first pulse, and which are still in an excited state when the second pulse arrives. The rate at which the current decays away from the centre value (at 0 ps) gives a more direct metric for evaluating the carrier lifetime, and is shown in Figure 3.3 (b). Each plot is normalised in the range of 0 ps to 18 ps. The time at which the peak amplitude decays to ~37 % is observed to range from 0.5 ps to 4ps, where each value is shown in Table 3.2.

In terms of the physical processes that occur in the LT-GaAs during annealing, this trend may is explained by the reduced dissipation of arsenic defects at lower temperatures causing faster carrier recombination when the LT-GaAs is annealed. The mean free path may then be so short, that many carriers do not reach the contacts and contribute to the

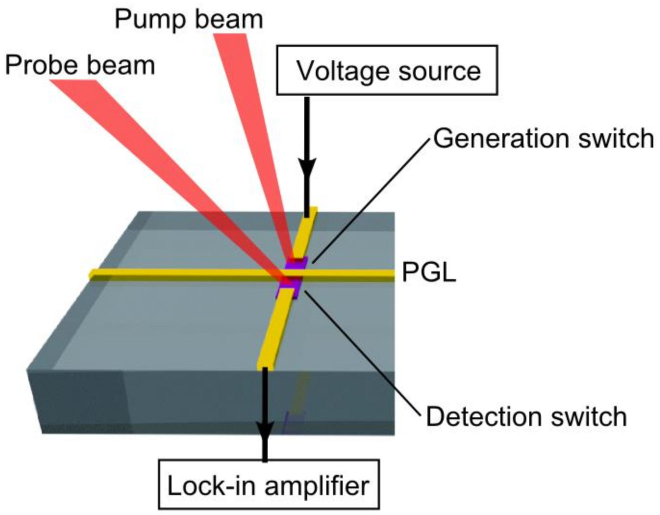

Figure 3.4: Experimental configuration for the measurement of "input" pulses

detected photocurrent. However, at higher anneal temperatures, the recombination rate is expected to be reduced as the arsenic diffuses into the GaAs crystal. Above a certain level, however, this inhibits the bandwidth of the pulse emission.

3.2.4 Input pulse measurements

"Input" pulses were measured to provide a reference signal generated by the switch. They are of importance in both the characterisation of devices to be used for spectroscopy, and in the interpretation of subsequently obtained spectroscopic data. To measure an "input" pulse, a probe arm (biased at 30 V) contacts the LT-GaAs. The switch was optically excited with 100 fs pulse duration, 800 nm centre wavelength, laser radiation to generate a THz pulse on the PGL. The "input" pulse is then sampled by the LT-GaAs switch directly opposite the generation switch (Figure 3.4), where the current detected as a function of beam delay time is shown in Figure 3.5. For all measurements throughout this thesis (unless otherwise stated), the peak of the "input" pulse is centred at 0 ps, which means that the time before the pulse has negative values. The standard for normalising pulses in all figures is to divide the signal by the peak positive value (when the baseline is 0 nA). This means that some signals may have a peak-to-peak amplitude greater than 1.

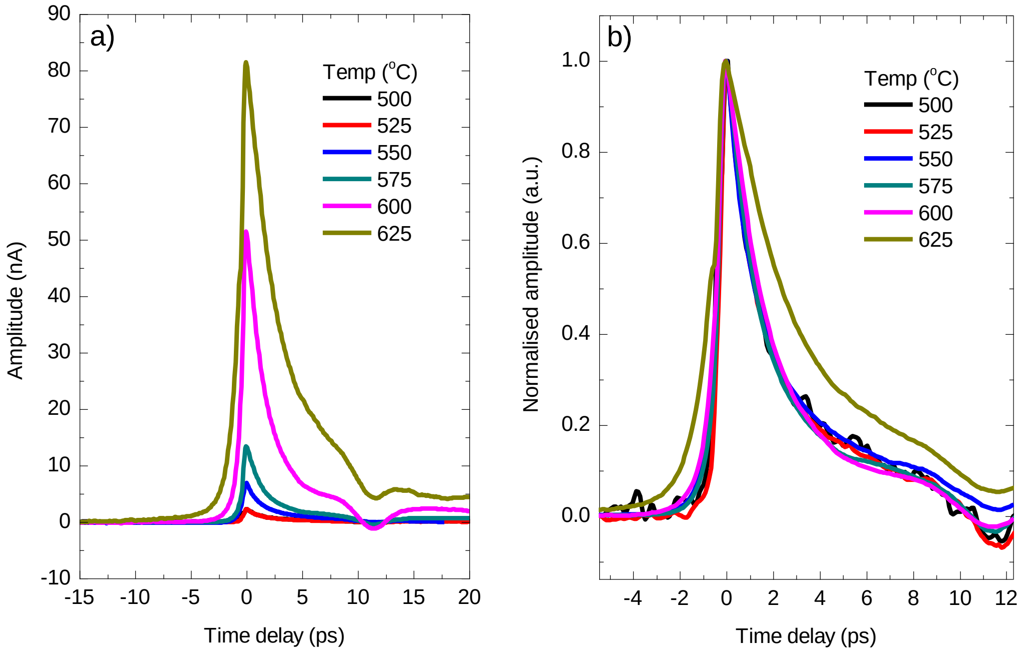

Figure 3.5: The "input" pulses measured on six devices, where the LT-GaAs in each was annealed at various temperatures. (a) The measured pulse for each device. (b) Each pulse normalised to emphasise differences in the pulse characteristics at each anneal temperature.

This measurement is important in the characterisation of an OC-THz-TDS device as it shows the pulse shape before it has had a chance to form into a propagating mode on the waveguide. The detector switch is directly connected to the lock-in amplifier, and illuminated by the 10 mW probe beam. Both beams used a 10 cm focal length lens and were polarised in the same direction as the biasing field. This was sometimes an issue for devices with 9 µm centre conductors, as the size of the laser spot meant that each beam also illuminated the opposing switch, as illustrated in Figure 3.6. This produces two superimposed signals in the time-domain; the stronger "intended" signal, as well as a weaker replica of the signal which is reversed in the time-domain (at 0 ps).

"Input" pulse measurements were conducted for the 6 devices in which the LT-GaAs was annealed at temperatures from 500 °C to 625 °C. Two or more pairs of switches on each device were measured, and the largest amplitude pulse from each device is plotted in Figure 3.5 (a). Each pulse was also plotted with normalised amplitude to allow pulse width comparison in Figure 3.5 (b). The amplitude data shows that the strength of the field increases with anneal temperature, and rises rapidly above 575 °C. However, the full width at half maximum (FWHM) of the pulses was consistent for values up to 600 °C (1.5 ps to 1.8 ps), but at 625 °C it was almost double the other values at 3.12 ps. This is interesting when compared to the autocorrelation data as the trend in carrier lifetimes is not carried through to the "input" pulse measurements. This was also noticed in separately conducted measurements of LT-GaAs.[70] One possible cause is that below a particular carrier lifetime, the properties of the switch (capacitance, resistance and inductance) dominate the frequency response of the switch.

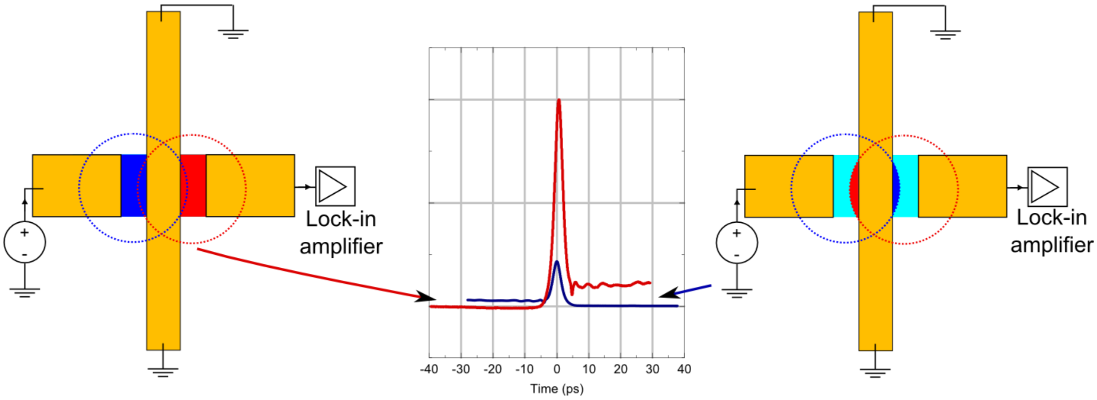

Figure 3.6: Illustration of the effects that is produced when the spot size is larger than the centre conductor. The intentional signal (left) is produced by the full illumination of each switch by the assigned beam. This is shown as a red trace in the centre figure. The un-intentional signal (right) is caused by the illumination of the opposite switch by each of the beams, the results is a smaller signal reversed in the time domain (blue in the central figure). The measured signal is a summation of the red and blue pulse shapes.

Table 3.3: Comparison of the signal to noise ratio for each anneal temperature.

Anneal temperature	500 °C	525 °C	550 °C	575 °C	600 °C	625 °C
Peak amplitude (nA)	2.28	2.29	7.15	13.67	52.41	83.02
Standard deviation (nA)	0.070	0.031	0.008	0.039	0.062	0.253
SNR (dB)	30.24	37.45	59.056	50.92	58.54	50.32

The performance of the switch may be improved by altering the geometry of the switches, as discussed in Section 2.2.5, but the design used here was chosen as it has previously been demonstrated to work at up to 2 THz on thinned quartz substrates.[68] As the devices used in this section were fabricated on higher permittivity bulk GaAs, the main limitation to reducing the FWHM is expected to be interaction between the THz field and the substrate.

The falling edge is typically what defines the bandwidth as it is highly dependent on the carrier dynamics of the system. The rising edge of the input pulse is the rate at which the electrons are pumped into their excited state and is predominantly defined by the excitation time of the laser pulse (100 fs in this instance). It is expected that for all pulses the leading edge should have the same rise time, which is observed to be true for all but the 625 °C annealed device. This is clearly a result of the longer carrier lifetime in this device but the exact reason for this is unknown.

The signal-to-noise ratio (SNR) of these signals is calculated by

$$SNR = 10\log\left(\frac{{I_p}^2}{{\sigma_{avg}}^2}\right), \tag{3-1}$$

where I_p is the peak of the main peak in nA, and σ_{avg} is the average standard deviation of the signal before the main peak. The SNR of each pulse is given in Table 3.3, where 550 °C shows the best performance. The devices with lower temperatures each have significantly poorer performance, as can also be seen by Figure 3.5 (b) in the form of short-period random deviations. From 550 °C upwards, the SNR value means that the signal is very clean and reflections and oscillations that may occur in the time-domain can be easily resolved.

Autocorrelation measurements and IV sweeps are both useful tools for analysing and characterising the material and fabrication techniques, but "input" pulse measurements are critical in the systematic evaluation of devices. This is because the frequency spectrum of the generated pulse determines the maximum system bandwidth which, as we see, is not limited solely by the properties of the semiconductor. Based on the results presented so far in this chapter for wafer L488, an anneal temperature of 575 °C showed the suitable LT-GaAs performance in terms of "input" pulse FWHM and signal-to-noise ratio. The LT-GaAs used for devices in the following chapters (L1130) was also annealed at 575 °C, which was found in all cases to provide ample performance in terms of amplitude, FWHM and signal to noise ratio.

3.2.5 Transmitted pulse measurements

Transmitted (or "output") pulse measurements were conducted using very similar techniques to "input" pulse measurements, with the difference that the sampled detection switch was now located some distance along the PGL from the generation switch. This distance was typically 0.5 mm to 2 mm depending on the device. As the pulse was allowed to propagate a finite distance, the velocity of the pulse could be determined directly by measuring the time of flight (TOF). A common method for doing this is to measure an "input" pulse and an "output" pulse in the same time window. Calculation of the velocity is determined from the known geometry and the time delay from the "input" to the "output" measurement. However, this measurement requires the probe beam to move between scans, and the path length of the beam is not maintained,

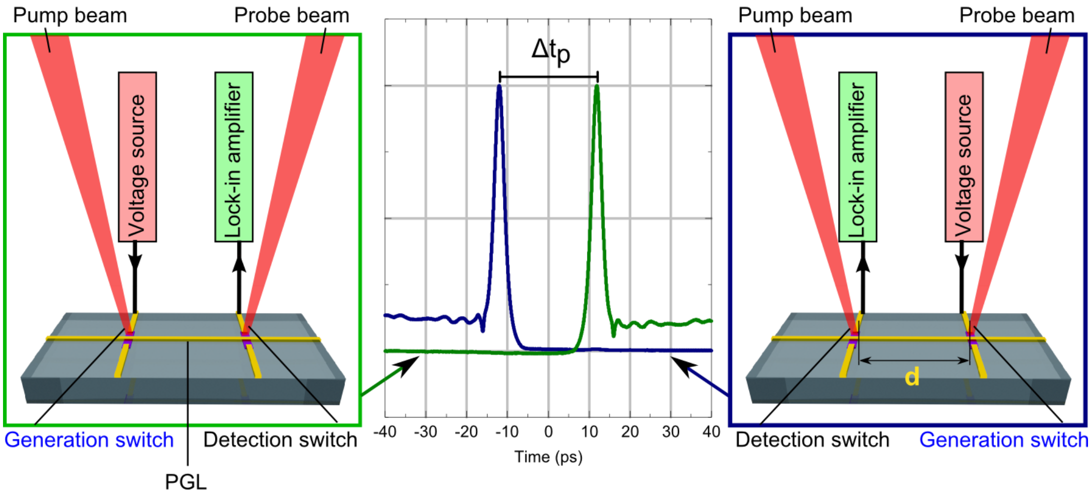

Figure 3.7: An illustration of pulse velocity measurement configuration using two switches. The bias and detection roles are alternated for the two measurements. This causes the pulse to travel from right to left (blue line) and left to right (green line).

especially if the beam is not perpendicular to the device. An alternative method, that does not require any re-alignment of the beams, is to measure an "output" pulse and then to swap the electrical bias and detector probe connections and perform a second scan using the same beam locations. An illustration of this measurement is given in Figure 3.7 for a PGL transmission line. The velocity of the pulse is

$$v = \Delta t_p / 2d \tag{3-2}$$

where Δt_p is the time difference between peaks and d is the distance between switches. This method was found to be the most accurate during device characterisation and was therefore used for propagation velocity measurements throughout this thesis. For clarity, however, many of the figures in the following chapters plot the "input" and "output" measurements on the same axis as this is a more intuitive way to describe how the pulse propagates through the device.

3.3 Characterisation of graphene

Since the first isolation of graphene in 2004,[72] many methods have been developed to identify and characterise the material. These range from advanced optical microscopy techniques,[122] to transmission electron microscopy (TEM),[123] and atomic force microscopy (AFM).[124] This section discusses the two primary methods that were used to characterise the devices used in this thesis to determine the sheet resistance, carrier concentration and layer thickness of devices.

3.3.1 Resistance measurements

Measurements of the resistance of the graphene were performed during fabrication and THz-TDS testing of the device. This allowed fast analysis of the contacts between the metal and graphene, and allowed an estimate of the quality of the graphene. During fabrication, an HP 4145A semiconductor parameter analyser was used in conjunction with a probe station to test the graphene transfer process. Values of sheet resistance for the top-contacted graphene ranged from 700 Ω/□ to 2000 Ω/□, when measured with four terminal sensing. To estimate the contact resistance for two-terminal graphene devices, two 5 μm × 9 μm metal/graphene Hall bar geometries were fabricated using the same top-transfer of graphene techniques. The contact resistance was established to be in the region of 300 Ω to 500 Ω.

The sheet resistance was periodically measured during the OC-THz-TDS characterisation of the sample to check for variations in the graphene's properties. These were typically performed after measurements that used higher bias, as many devices in the early stages of this project were especially prone to failure due to static discharge or joule heating. These issues were significantly reduced for the devices in the following chapters by applying an inert photoresist to the surface of the graphene, which helped with structural and thermal stability during measurements.

3.3.2 Raman spectroscopy

Raman spectroscopy of the devices, used throughout this thesis, was performed using a Horiba Jobin Yvon Raman microscope with a 532 nm laser source. Measurements in the early stages of this project used a 633 nm laser source, but it was found that the background signal levels from quartz were significantly higher due to fluorescence at this wavelength. The highest scan resolution was used (1800 grooves per millimetre grating) and the optimal sensitivity, without saturation, was found to be 90 seconds per measurement with 10 averages at each scan range. The 50 × objective lens that focussed the beam onto the sample resulted in a spot size of ~1um.

To identify graphene, scans were conducted in the range from 1200 cm^{-1} to 2850 cm^{-1} where the key resonances were found at approximately 1350 cm^{-1}, 1580 cm^{-1} and

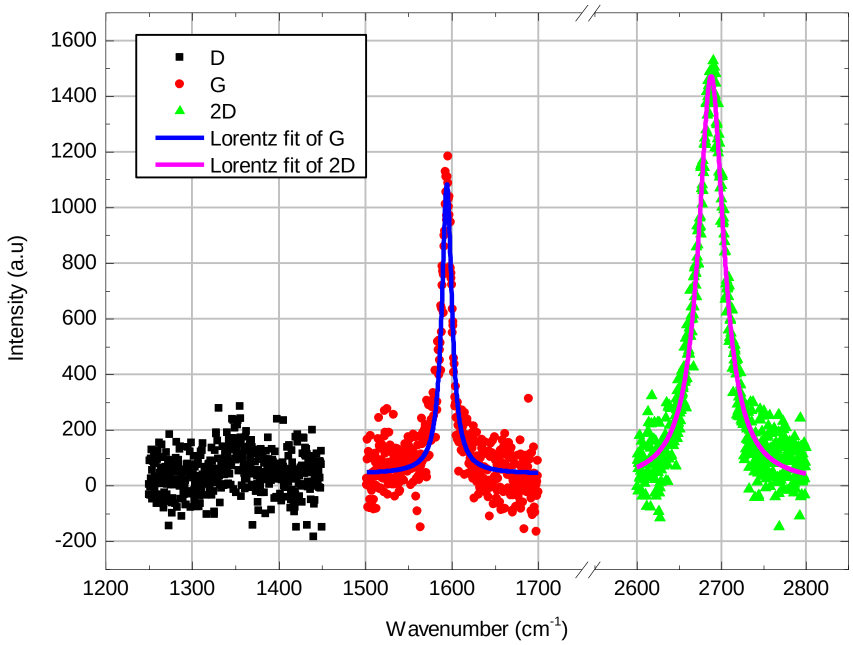

Figure 3.8: Raman spectra of the D-band (1250 cm^{-1} - 1450 cm^{-1}), the G-band (1500 cm^{-1} - 1700 cm^{-1}) and the 2D-band (2600 cm^{-1} - 2800 cm^{-1}) for the device used in Sections 4.5, 5.2, 5.3, and 6.2.

2700 cm^{-1} for the D, G and 2D bands respectively.[125] Each band corresponds to in-plane vibrational modes and, although the precise shape of the peaks are complex, the ratios and positions can be used to quickly evaluate important properties, such as the number of graphene layers, or carrier concentration.[126,127]

The bands that are used to identify and characterise graphene are shown if Figure 3.8. The device measured is D3, the same device discussed in Sections 4.5, 5.2, 5.3, and 6.2. The D peak was found to be weak and too small to extract meaningful values for its height, etc. This indicated that the crystal domain size of the CVD grown graphene was not significantly smaller than the Raman spot size (~1 μm) and the overall quality of the graphene was good. A single Lorentz fit was performed for both the G and 2D bands where the individual parameters for each are shown in Table 3. The values indicate a single layer of graphene based on the location, FWHM and intensity ratio (I_{2D}/I_G). In order to determine the carrier concentration, the values of the G-peak position and intensity ratio (I_{2D}/I_G) corresponded to a p-type carrier concentration of $6 \pm 2 \times 10^{12}$ cm^{-2}, when compared to the measurements of Das *et al* for a Raman data at range of carrier concentrations.[127]

Table 3.4: Raman peak values for transferred CVD graphene on quartz from Graphene Square (Korea).

Peak	Position (cm^{-1})	FWHM (cm^{-1})	Area (a.u.)	Intensity (a.u.)
G	1594	13.9	22651	1041
2D	2687	36.5	84162	1466

Raman spectroscopy was also used to determine if LT-GaAs was fully removed after etching to ensure that the photonic effects can definitely be attributed to the graphene. This is discussed in detail in Section 5.2.2.

Chapter 4: On-chip terahertz spectroscopy of graphene

4.1 Introduction

This section discusses the design and measurement of an on-chip terahertz waveguide device to investigate the pulse reflection and propagation properties through a channel of graphene. The devices were engineered to allow multiple geometries to be tested for reference and spectroscopy measurements, using a single chip. This was done to enable consistency of the graphene and LT-GaAs properties and to minimise the necessity for multiple devices to be fabricated. The geometries that are characterised include a straight, continuous waveguide as a reference measurement, and increase in complexity towards a cross-shaped graphene region contacted by four independent terahertz transmission lines, each with the ability to transmit or receive pulses. Finally, the first “on-chip” optical-pump terahertz-probe (OPTP) measurements are presented, as a means of comparing the existing literature of “free-space” OPTP measurements.

4.2 Device design

Quartz substrates that incorporate LT-GaAs, metal transmission lines and graphene, require many fabrication steps, where each of the three fabrication stages has the potential to compromise any of these materials. The complexity of the fabrication means that it can also take 2 – 3 weeks to fabricate a single device, which is very labour intensive if many device geometries are to be tested. To address this, the early stages of this work focussed on obtaining a device design that was simple to fabricate, easy to integrate with graphene and would provide a clean response in the time-domain, without any significant reflections or features that would distort the pulse.

The design of the device must minimise reflections in the time-domain that are not associated to the sample under test. These reflections mask, or interfere, with spectroscopic information from the sample (oscillations or reflections) and can make analysis difficult. Features that cause impedance mismatches are typically avoided in terahertz frequency waveguides, including geometric changes in the path of the propagating pulse, open circuits, or short circuits. Metal features placed close to the waveguide may also interact with the evanescent terahertz field. Not all reflections can be avoided, especially those attributed to the bonding pads at the end of each waveguide. Hence, these are typically placed far away to maximise the reflection-free time window.

A large reflection-free scan window is desirable for spectroscopy applications, and so on-chip device designs are typically very simple. These are often single transmission lines with two pairs of photoconductive (PC) switches so that the remaining available space can be kept clear, or be used for long transmission line connections to the bond pads. The design, shown in Figure 4.1, implemented similar switch and PGL regions to existing OC-THz-TDS PGL devices[68] but required modifications to be used for THz measurements of graphene. It was also designed to fit many individual PGL configurations onto a single chip, whilst attempting to minimise unwanted cross-talk between close proximity waveguides.

The maximum number of devices that could be incorporated was limited by the area of LT-GaAs that is transferred to the quartz and the minimum separation between parallel PGL lines. The LT-GaAs fabrication process had been optimised for sizes of approximately 4 mm × 4 mm. Although wafer scale regions can be transferred,[128] the selected size was used to conserve LT-GaAs material. The minimum separation between parallel PGL lines was chosen based on simulations of the perpendicular evanescent field of a 9 μm wide PGL on quartz.[70] The amplitude was shown to decay away from the centre to <10 % when 50 μm above the metal and to <2 % at 200 μm. For the device in Figure 4.1 (c), the separation between horizontal PGL lines in the centre region (between the red bars) was 300 μm, as these are very sensitive regions. The separation between the PGL and probe lines (thicker black areas) was 150 μm.

The width of each PGL was 9 μm, and was chosen to be reasonably small to have a tighter field confinement to metal, whilst still being large enough so that optical lithography features were well above the tolerances of the processing. The PGLs and probe arms connected the bonding pads, on the far left and right of Figure 4.1 (a), to the PC switch bars (Figure 4.1 (c) - red vertical bars). As reflections may occur at sharp PGL bends, these were graduated from the centre to minimise the total bend angle, where the bend is ~1.2 mm away from the PC switches. The overall size of the device was designed so that it could be fabricated on 16 mm × 16 mm quartz substrate because, if time permitted, the device would be tested in a cryogenic OC-THz-TDS system with 12 T magnetic field capabilities. Three separate mask designs allowed the distance between switches (and LT-GaAs bars) to be 500 μm, 1 mm or 2 mm apart. This was implemented to vary the total propagation length of the "output" pulse if desired. For simplicity, all measurements in this chapter are for the 2 mm geometry.

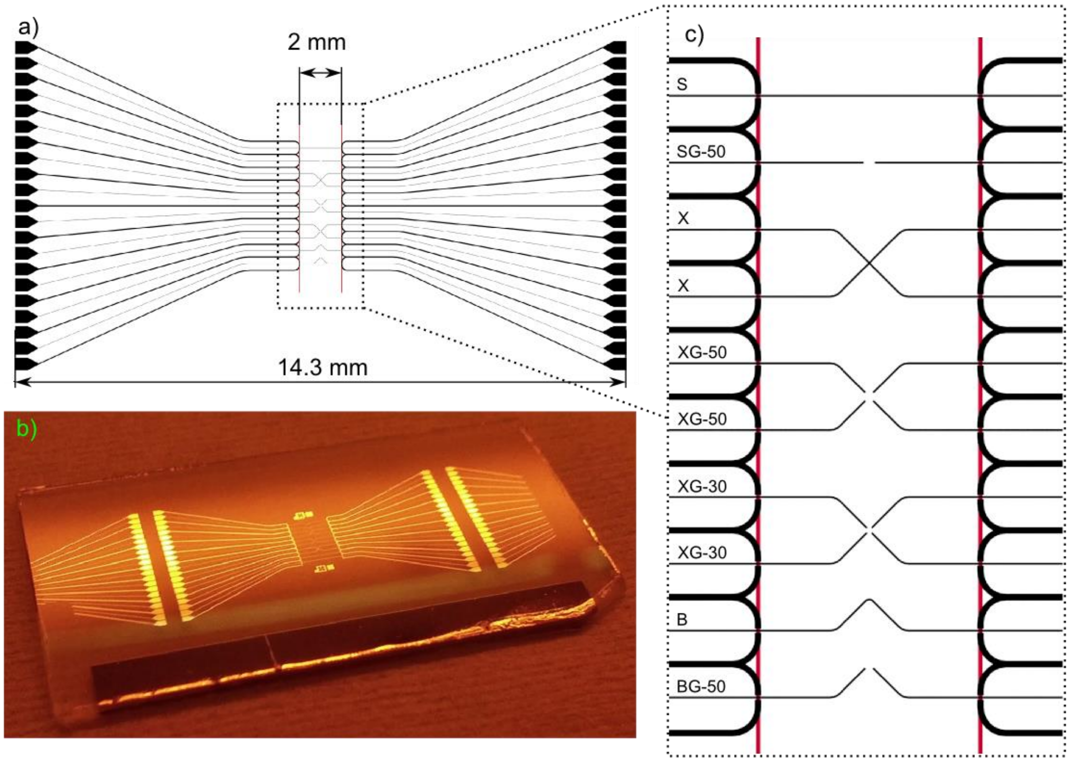

Figure 4.1: Design of multi-device, on-chip THz TDS system. (a) The full device design with metalized regions in black and red parallel LT-GaAs strips 2 mm apart in the centre. (b) An image of the fabricated device on a 20 mm × 25 mm quartz substrate. (c) The design of the central PGL region.

The design incorporated seven seperate configurations, seen in Figure 4.1 (c), that were grouped into three experiments: (S) straight PGL characterisation; (B) 90° bend PGL characterisation; and (X) cross-shape characterisation. Each of the experiments consisted of one reference device that had a unbroken PGLs from left to right, labelled as S, X and B. These geometries were replicated with a 50 μm gap in the centre, as shown by SG-50, XG-50 and BG-50. The cross configuration also had a 30 μm gap configuration, XG-30.

For reasons stated below, not all devices were characterised, but S, SG-50 and X-50 are each plotted with their important dimensions in Figure 4.2, where the switches are labelled left (L) or right (R) and numbered for each device. The straight PGL characterisation setup, shown in Figure 4.2 (a), allowed a benchmark measurements as a comparison to straight PGL designs used in previous projects. This, in turn, would allow better interpretation of the more complex designs on the rest of the device. In the lower section of Figure 4.2 (a), the 50 μm gap of device SG-50 was selected to provide a large enough separation between the left and right PGL to keep cross-talk to a minimum, but to be small enough so that if any signals were coupled to the graphene (red) they would not be significantly attenuated.

The 90° bend PGL experiment (not pictured in Figure 4.2) was added to reduce the level of cross coupling over a similar sized gap in the straight PGL configuration, where similar designs were previously studied.[34,117] This geometry was not characterised in this project, as the four terminal cross device in Figure 4.2 (b) was considered more versatile as it provided one "straight" and two "90° bend" geometries in the same device.

The design XG-50 had two 50-µm-long perpindicularly-crossing segments of the metal PGL in the centre of the device replaced with graphene. Each of the four PGL lines acted as electrical contacts to the graphene. Two LT-GaAs switches we positioned on each of the PGL lines so that "input" pulse measurements could be made for each induvidual waveguide. "Output" pulse measurements in any combination, could also be performed from one switch pair to another to characterise the transmission through the graphene area. However, the single probe arm for PC switches X-L2 and X-L3 (also X-R2 and X-R3) was primarily intended to be used for "input" pulses, and shared the same connection. Therefore, "output" pulses between these switches could not be measured. Due to the bends of the transmission line, the total path distance through the graphene to any other switch pair is ~2.19 mm.

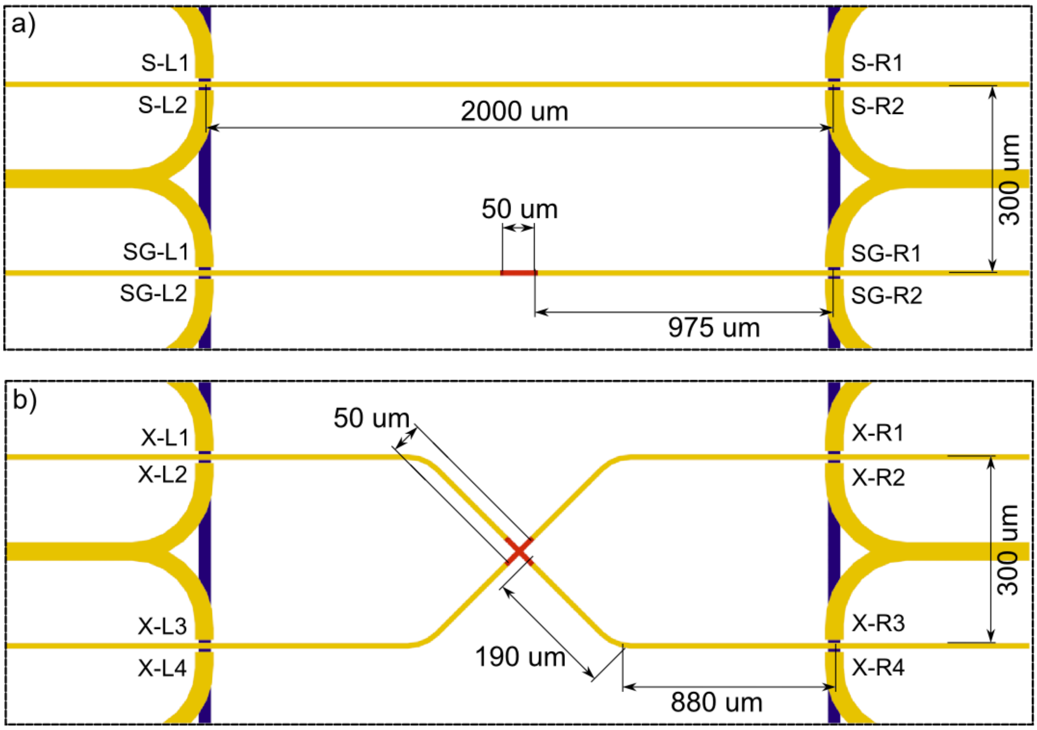

Figure 4.2: Schematic of the PGL region with LT-GaAs illustrated in blue, gold in yellow, and graphene in red (not to scale). (a) The straight PGL characterisation setup with and without gaps. (b) The cross shaped graphene design with four terahertz PGL lines as graphene contacts.

4.3 Characterisation of Goubau lines

To characterise the performance of the switches and waveguides in this design, a reference device D1 was fabricated without graphene. The straight PGL design "S" was used to measure "input" pulses from switches S-L1 to S-L2. "Output" pulses were measured from S-L1 to S-R1, where the total pulse propagation distance was 2 mm. The results from these measurements are shown in Figure 4.3. The PGL was 9-μm-wide and 80-nm-thick, where the skin depth of the field in the metal is ~78 nm at 1 THz, and ~250nm at 100 GHz. As the metal thickness should ideally be three times the skin depth of the lowest frequency, the transmission line is expected to contribute to losses that could, otherwise, be rectified by using a thicker metal film. However, the graphene transfer technique described in Section 3.1 had a high failure rate with metal films thicker than 100 nm. Transmitted pulses, measured using an 80-nm-thick PGL, could still support few-picosecond pulses with suitable signal-to-noise ratios and, hence, this thickness was used for all graphene terahertz devices.

When analysing terahertz time-domain measurements, there are typically three main features which can be analysed: the main pulse; reflections from impedance mismatches; and resonances that are excited by the main pulse. The amplitude of the "output" pulse in Figure 4.3 appears to be larger than the amplitude of the "input" pulse, although it is clear that there are no active components in the system and, hence, there cannot be gain.

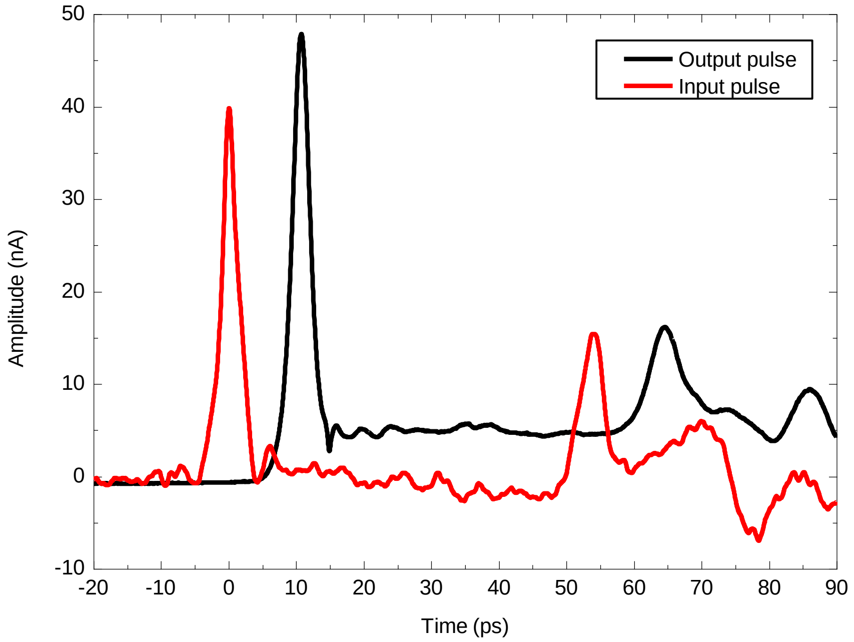

Figure 4.3: The "input" and "output" pulse measurement for a straight PGL line.

This larger amplitude is an illustration of the variation in switch properties across the device due to micro-cracking and stresses, a result of the van der Waals transfer process. For this reason, caution should be used when comparing the amplitude of two sets of results that are not tested using the same switches. In this instance the same generation switch (S-L1) was used, and indicated that S-R1 is more efficient as detection switch than S-L2. Furthermore, the "input" pulse measurement has greater noise levels than the "output" pulse, as can be observed by the short time period fluctuations (<2 ps) along the total length of the scan.

The time difference between the two pulses in Figure 4.3 is 10.8 ps, and corresponds to a velocity of 1.85×10^{8} m s^{-1}. However, as described in Section 3.2.5, this is a coarse evaluation of velocity and a more accurate measurement can be determined from the forward and reverse "output" pulse measurements plotted in Figure 4.5, where the velocity is 1.67×10^{8} m s^{-1}. This value is consistent with previous devices that were measured using the same permittivity quartz substrate and the PGL dimension.

The full width at half maximum (FWHM) is often used to characterise the carrier dynamics of the LT-GaAs, and also gives an estimation of the total bandwidth of the pulse, where a smaller FWHM generally indicated a broader bandwidth. For the straight device, the "input" pulse FWHM is 2.7 ps and broadens to 3.1 ps at the output, which is a typical result of phase dispersion. An in depth study of the dispersion of a similar 2 mm PGL has previously been investigated by Gacemi *et al*, where a linear dispersion relation was found below 600 GHz as shown in Figure 4.4.[39] Above 600 GHz, increased dispersion and attenuation was attributed to an increased confinement of the propagating

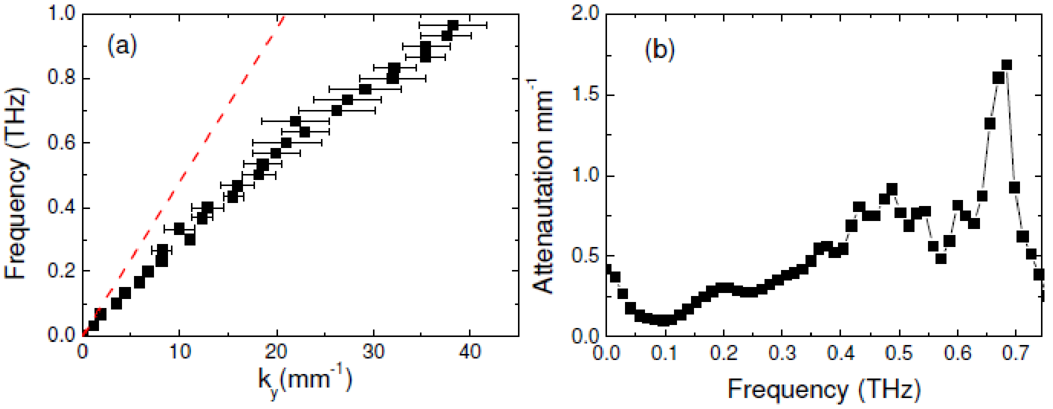

Figure 4.4: The propagation properties of a THz pulse on a 5 µm wide PGL line measured up to 2 mm from the reference pulse as recorded by Gacemi *et al.* Ref 39. a) The dispersion relation (black) with the plane wave dispersion in red. b) Electric field attenuation as a function of frequency at 2 mm.

mode in the substrate. This is in good agreement with the FFT data of Figure 4.5 where the noise levels are drastically increased in the output pulse above 500 GHz. The values of FWHM, measured on device D1, are relatively large in comparison to other "input" pulse measurements using the same switch geometry, which can be as low as 1.65 ps on device D3. This demonstrates the variance of carrier properties that also vary from one LT-GaAs transfer to another.

Reflections from other features on the waveguide are seen at ~54 ps in the "input" pulse scan and ~65 ps in the "output" pulse. These are unusual for this type of device, as they were the same polarity as the main peak (indicating an open-circuit feature as described in Section 4.3), and arrived >10 ps earlier than the short-circuit reflection at the bond pads was expected. Therefore, it was evident that these must originate from a defect in the device. The location of the defect can be determined to be 4.5 mm away from the main switch, where the bond pads are located 6.5 mm away. This defect, a small break caused by the metal lift-off process, was subsequently identified using optical microscopy and was found to be in the expected position. As the defect was so far away from the switch region, it was not detrimental to the other measurements other than slightly decreasing the reflection-free time window from 70 ps to 50 ps and, hence, the fast Fourier transform (FFT) resolution is decreased from ~15 GHz to 12 GHz.

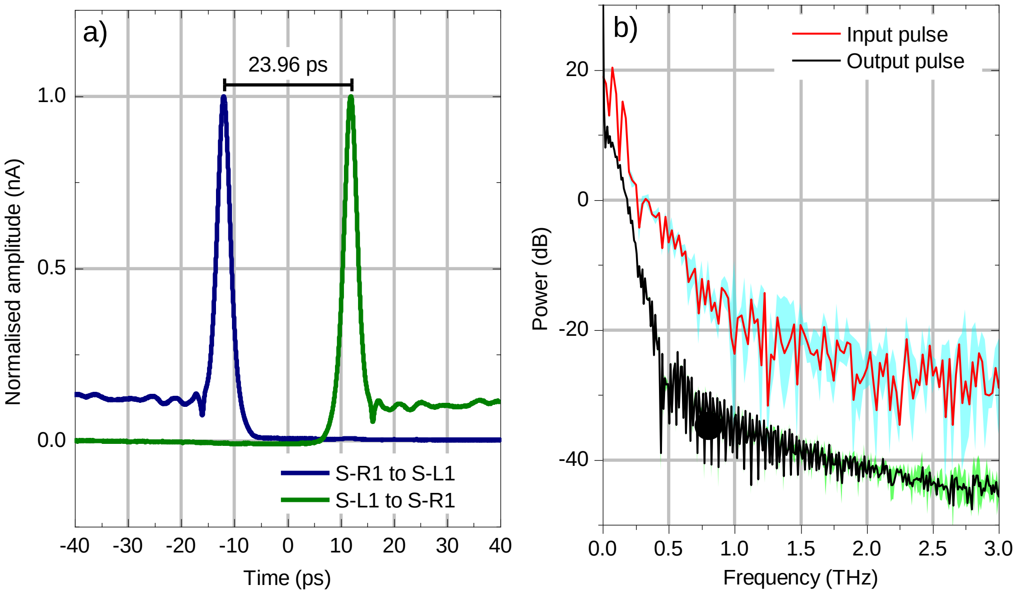

Figure 4.5: (a) Time of flight measuring the propagation velocity of the PGL. (b) Average FFT power spectrum of five scans measured at the "input" (red, with blue standard deviation) and "output" (black, green standard deviation) locations.

The small oscillations that are observed immediately after the main pulse are caused by reflections in the probe arms. The upper probe arms consisted of a single 30-µm-wide PGL that ran directly to the bond pads and did not contribute to these oscillations. However, the lower probe arms were also shared with the adjacent design and produced Fabry-Pérot like oscillations. The splitting point between S-L2 and SG-L1 caused a lower impedance interface, followed by a higher impedance interface when the pulse arrives at the opposing switch. This was overlooked in the design phase, and meant that all pulses on this device were followed by oscillations of varying intensity with a 4.5 ps period. In the time-domain, the oscillations can be seen, but the amplitude relative to the background is small. Resonances can, sometimes, be seen more clearly in the frequency-domain by calculating the FFT of the pulse measurement. The 4.5 ps period corresponds to a small feature at ~220 GHz on the "input" pulse trace, and is even weaker in the "output" pulse trace. Although this resonance is small for device S, it is mentioned because it is much more apparent in the measurements of SG-50 and XG-50, where both the generation switch probe arm produces the Fabry-Pérot oscillations and is seen clearly in both the time- and frequency-domain.

The spectral range of the "input" and "output" pulses can also be determined from the FFT spectra, where the power level for the "input" pulse becomes indiscernible from the noise floor at a little under 1 THz. The FFT of the "output" pulse shows a clean signal up to 400 GHz and then becomes very noisy, which is consistent with the FWHM of the respective switches. Further reference measurements of the other designs included on device D1 could not be performed as the quality of the LT-GaAs switches was insufficient to take pulse measurements. A second device was then fabricated to test how the variation of design S was altered by the presence of graphene.

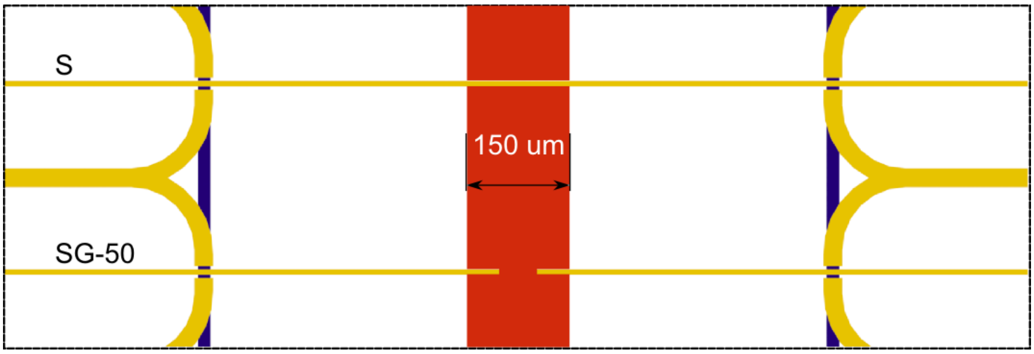

Figure 4.6: Illustration of graphene configuration for device D2, with a 150 µm wide channel of graphene from the top to the bottom of the device.

4.4 Characterisation of Goubau lines with graphene

Device D2 was fabricated using the same PGL design and dimensions as Section 4.3, but with a 150-μm-wide graphene channel that was 4-mm-long perpendicular to the direction of the PGL, as shown in Figure 4.6. This graphene strip electrically connected the centre of the seven devices on the chip to each other. The resistance of the graphene between metal contacts of device SG-50 was 3 kΩ and, therefore, the two-terminal sheet resistance per square must be larger than 0.54 kΩ/□ (assuming that the minimum channel width was the width of the PGL, 9 μm).

The normalised "input" and "output" time-domain results for the continuous PGL design "S", with graphene, are plotted in Figure 4.7. The relative arrival time of the "output" pulse is similar to Section 4.3, and hence no significant change to the average permittivity is observed, which is expected for an atomically thin sample. A clear indication that graphene was in contact with the transmission line can be inferred from the time-domain scan, where the negative polarity reflection of the "input" pulse is detected at 11.5 ps. This reflection, which originated from the transition between the PGL and the lower impedance graphene interface, occurs ~1 mm away from the switch and propagates a total length of ~2 mm. This distance is the same as the "output" pulse and, hence, they arrive in the time-domain at the same time.

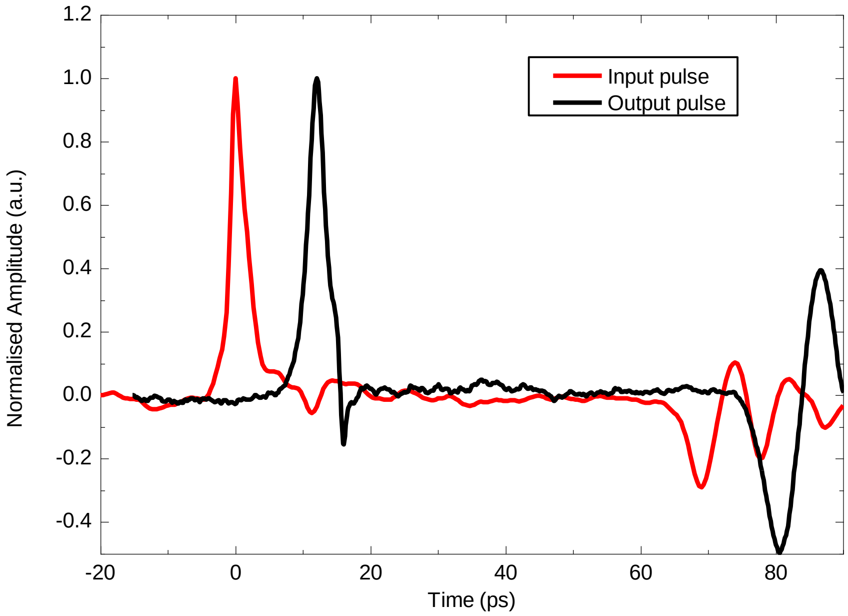

Figure 4.7: Normalised "input" and "output" pulses for a straight 2-mm-long PGL line with a 150-μm-wide graphene channel in the middle. The "input" pulse has an amplitude of 5.55 nA and a 2.6 ps FWHM. The "output" pulse amplitude is 2.68 nA with a FWHM of 2.97 ps.

The reflections that occur after 60 ps are caused by the lower impedance bond pads at the far ends of the PGL, and the shortest path arrived after a total distance of 13 mm with a velocity of approximately 1.88×10^8 m s^{-1}. This is faster than the 1.67×10^8 m s^{-1} measured in Section 4.3, where the difference is attributed to the formation of a (faster) CPW mode propagating between the centre conductor and probe arms. The "output" pulse reflection is about twice as large in amplitude than the "input" pulse reflection. This is because the total path length from the "input" switch to the bond pad and then back to the output switch is the same for both left and right bond pads. Therefore the two reflections arrive in phase, and constructively interfere. However, the "input" pulse reflections that occur at the left and right bond pads travel different path lengths and do not arrive with the same phase.

Other than the reflection from the graphene region, the "input" pulse is very similar to the device with no graphene in Section 4.3 and has a FWHM of 2.6 ps. The "output" pulse, with a FWHM of ~3 ps, has a very distinctive difference to the non-graphene device in the form of a sharp negative spike ~4 ps after the main pulse. This is due to interactions between the pulse and the graphene section, where the shunt inductance, capacitance and resistance of the graphene will change the shape of the pulse. A shunt inductance would act as a differentiator in this configuration, which is a possible explanation for the sharp negative spike. However, the FFT of "input" and "output"

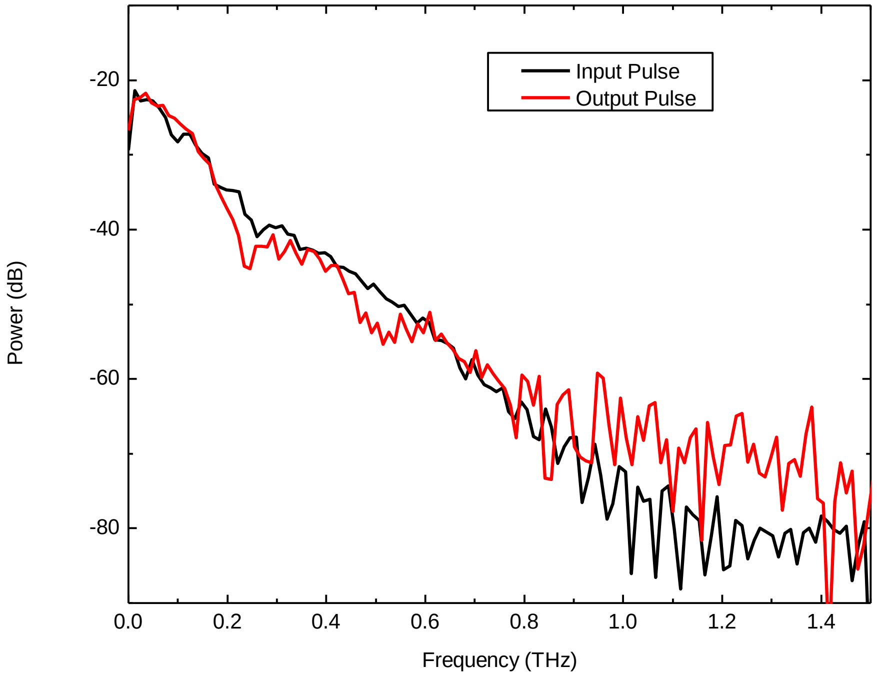

Figure 4.8: FFT spectrum for the input and output pulses for the Device D2 and design S.

pulses (Figure 4.8) reveal a very similar frequency response which does not vary by more than 6 dB from DC though to 800 GHz. The lack of frequency dependency indicates that the reactive elements (capacitance and inductance) have a negligible influence on the pulse and the change in shape is more likely to be a result of the graphene's resistive effects.

Using device D2, the design SG-50 was also tested by generating pulses from SG-L1 and detecting them at SG-R1. The normalised "input" and "output" measurements are shown in Figure 4.9. The gap in the PGL is observed to produce a reflection at 11.7 ps in the "input" pulse measurement, the amplitude of which is ~40 % of the main pulse and is positive in polarity. The "output" pulse measurement, on the other hand, is distinctly different and displays a large resonance with a period in the range of 5.16 ± 0.86 ps, which exponentially decays with a time constant of ~6.3 ps. The negative pulse immediately after the main pulse is caused by a series capacitance (or parallel inductance). With the addition of a gap to the PGL of this design, this type of response would be expected. However, this only accounts for the first positive and negative pulses and not necessarily for the oscillations seen from 16 ps to 45 ps.

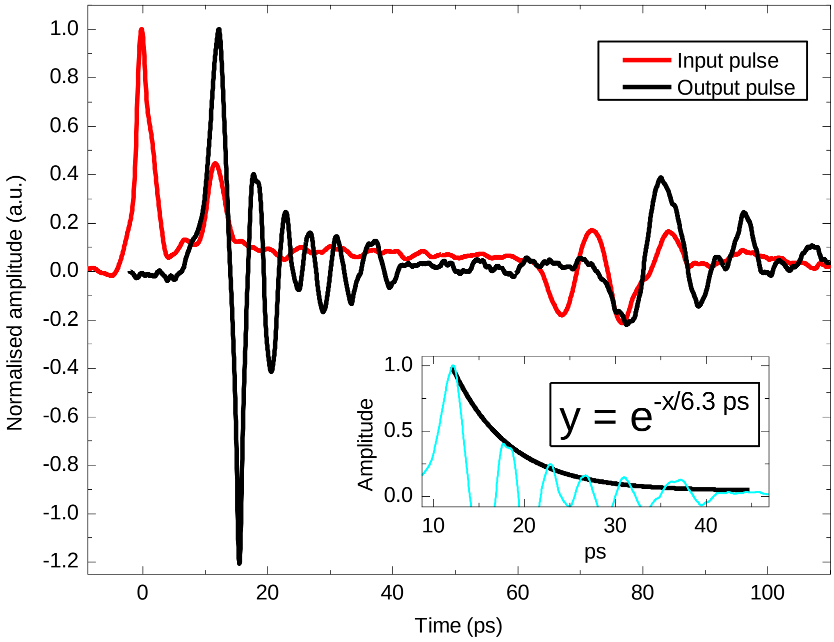

Figure 4.9: "Input" and "output" pulse for a gapped 2-mm-long PGL line (SG-50) with a 150-µm-wide graphene channel in the middle (device D2). The "output" pulse peak arrives 12.49 ps after the main pulse. The pulses have been normalised by dividing by the most maximum positive value. The exponential fit of the "output" pulse envelope is shown inset.

Before the possible sources of these oscillations are discussed, it is convenient to determine their representation in the frequency-domain. Large, sharp features in the time-domain produce high frequency components and, hence, an increased bandwidth would be expected to be due to the large negative peak at 15.6 ps. The FFT of the "input" pulse was subtracted from the FFT of the "output" (Figure 4.10) to obtain the differential frequency response. This allowed a clearer observation of the frequency components that contribute to the oscillation. The peak of the resonance in the frequency-domain occurs at 800 GHz and has a response up to 1.5 THz. This behaviour can be explained by the capacitor-like response caused by the 50 μm separation of the two PGL graphene contacts, where the higher frequencies couple more effectively than the lower frequencies, and DC is blocked entirely. This leads to the spectrum seen in Figure 4.10, where there is a 25 dB difference between DC and 800 GHz.

There are a few possible mechanisms by which dampened oscillations can occur in a complex on-chip time-domain system such as this, including by plasmon resonances and by Fabry-Pérot oscillations. The latter may occur at multiple locations e.g. the pulse can be reflected between the metal/graphene interfaces at the 50 μm separated PGLs or between the edges of the 150 μm graphene channel. This would account for the repetitions of the pulse in the time-domain. Fabry-Pérot cavities typically produce sharp

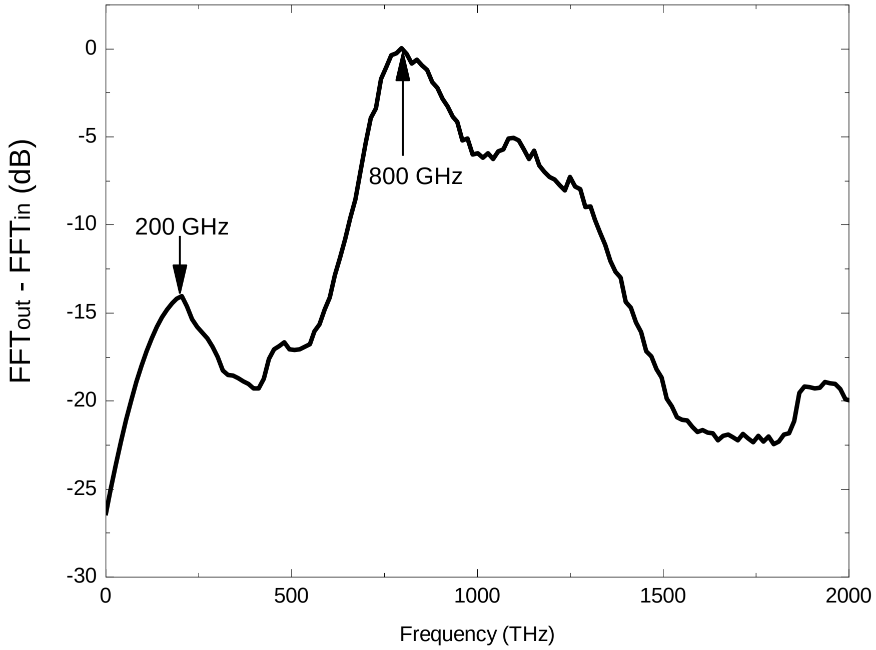

Figure 4.10: Differential FFT of the "input" and "output" pulse measurements of a 2-mm-long PGL line with a 150-μm-wide graphene channel spanning the width of the 50-μm-long gap. The resolution of the data is 14 GHz. (N.B. subtraction of the two FFTs in dB is the same as division in a linear scale)

resonances in the frequency-domain. If a period of 1.25 ps is used, corresponding to the largest resonance of the system at 800 GHz, a velocity of 40 × 10^6 m s^{-1} is required for a 50 μm gap or 120 × 10^6 m s^{-1} for a 150 μm channel. These velocities are slow for a typical metal PGL waveguide on a low permittivity substrate and could be an indication of strong coupling of the terahertz field to the graphene, where higher confinement results in slower velocities. As discussed in Section 2.4.4, excited plasmon modes in graphene display confinement up to 40 times greater than free-space.

4.5 Characterisation of cross-geometry graphene

A third device was fabricated, D3, in which the graphene region was defined into channels between the PGL contacts, as indicated in red in Figure 4.2. The 2 mm cross geometry, XG-50, was tested and its "input" pulse and corresponding FFT are shown in Figure 4.11. In the time-domain, the main pulse has a FWHM of 1.9 ps and a reflection of this pulse is seen at ~12.5 ps. As the path from the switch to the graphene is not a straight line, the total propagation distance is 2.14 mm, and not 2 mm as it was with device XG-50. Therefore the pulse velocity is 1.71 × 10^8 m s^{-1}, in good agreement with previous measurements. An "input" measurement was taken at each of the four switches and differences were found in the amplitude of the reflection from 42 % to 54 %. The FWHM of the main peak was 1.8 ± 0.2 ps when sampled on the left side of the device,

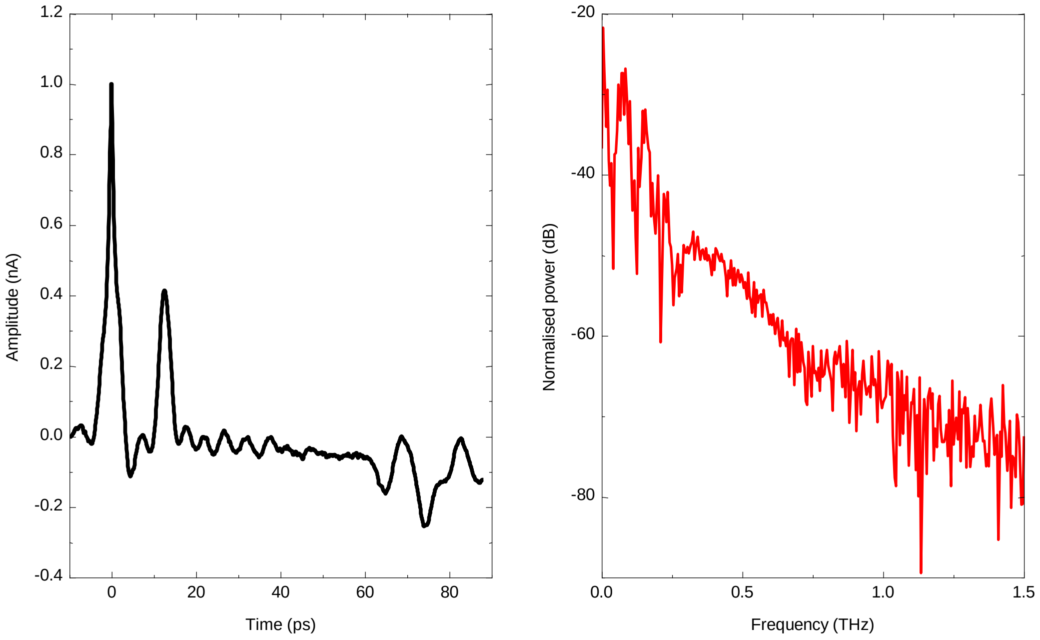

Figure 4.11 (a) "Input" pulse of the cross geometry device as generated at X-L1 and detected at X-L2. (b) FFT of the "input" pulse.

and 2.6 ± 0.2 ps on the right side of the device due to the variance of the LT-GaAs material.

The “input” pulse in the frequency-domain displays a clear resonance at 220 GHz which is from the probe arms, as discussed earlier. There is also a ~80 GHz feature which corresponds to a waveform period of 12.5 ps and is due to the main pulse and its reflection being interpreted as a single wave in the FFT function. The frequencies produced by the “input” pulse (X-L1 to X-L2) extend up to ~3 THz, but the spectrum becomes slightly noisier after 600 GHz.

For simplicity, not all combinations of “output” pulse are shown. The two generation switches that were selected to be shown were chosen from the left side of the device due to their lower FWHM “input” pulses. Figure 4.12 shows the “output” pulses where distinct features were observed for each of the three possible pulse directions. To prevent confusion the paths will be referred to as:

- Forward – the pulse travels directly across the graphene cross to the opposing PGL e.g. from X-L1 to X-R4.
- 90° opposite – the pulse path bends 90° at the graphene region and is detected at the opposite side of the device e.g. from X-L1 to X-R1.
- 90° return – the pulse path bends 90° at the graphene region and is detected on the same side of the device e.g. from X-L1 to X-L4.

The pulses detected by the inside switches X-R2 and X-R3 can be seen to oscillate much more energetically. This is because the probe arm is in close proximity to two PGL lines, each with approximately equal strength pulses traveling along them. The unwanted signal on the opposite PGL will arrive with a phase delay due to the longer path length. By making the assumption that this same interference does not reach the outer switches (X-R1 or X-R4) an approximation of the cross-talk can be obtained by subtracting the signal detected at X-R3 (inner) from the signal detected at X-R4 (outer). The result (not shown) was strong oscillations starting at 1 ps, with a period of ~4.5 ps (220 GHz) caused by the resonant probe arm. Therefore, in the following analysis of “output” pulses, pulses detected by the inside switches X-R2 and X-R3 are only relevant in the time range from -15 ps to 1 ps.

As the structure of this device is quite complex, there are some propagation paths, from one switch to another, that are shorter than the path through the graphene. Because of this, features can be observed before the ‘graphene path’ arrival at 0 ps. The most prominent of which is found on the ‘90° return’ path of the beam (e.g. X-L1 to X-L4), where a sharp rise in amplitude is observed at -7.2 ps due to direct coupling across the probe arm. The amplitude of the signal then decays slowly as the falling edge of the direct pulse coincides with the rising edge of the main pulse.

The "90° opposite", and "forward" path do not share a probe contact with the emission switch and, therefore, the amplitude of the oscillations is lower. The rising edge of each of these pulses begin at the same time, however, they differ very slightly as the forward path includes a small peak at -4.2 ps, best illustrated by the pulse from X-L4 to X-R2. If this peak is considered to be a discrete pulse that is generated at the same time as the main pulse, its velocity is ~2.7×10^{8} m s^{-1} which is too fast for waveguide propagation on quartz. If this is the case, then the small peak cannot have travelled along the PGL and, hence, did not pass through the graphene and, therefore, cannot provide any information on the properties of graphene.

The 90° geometry was specifically selected to reduce cross-coupling, as predicted by simulations using the finite element method (Ansoft HFSS), in which it was established that frequencies above 400 GHz are strongly attenuated in comparison to "straight" designs.[117] Similar 90° designs were also used in mm-wave measurements of graphene.[34] presumably to also reduce cross-coupling between the transmission lines. The measurements of this device show that the oscillations of the "90° opposite" path in Figure 4.12 are the most inhibited, when compared to the other measurements, where X-L1 to X-R1 is the best example of this. However, the overall differences between "forward" and "90° opposite" paths are small, and the peak-to-peak amplitudes do not show any significant attenuation for either path length. This may be due to the close proximity of the four graphene contacts in relation to the wavelength of the signal (>300 μm), leading to cross coupling beyond the levels predicted in the continuous-wave simulations.

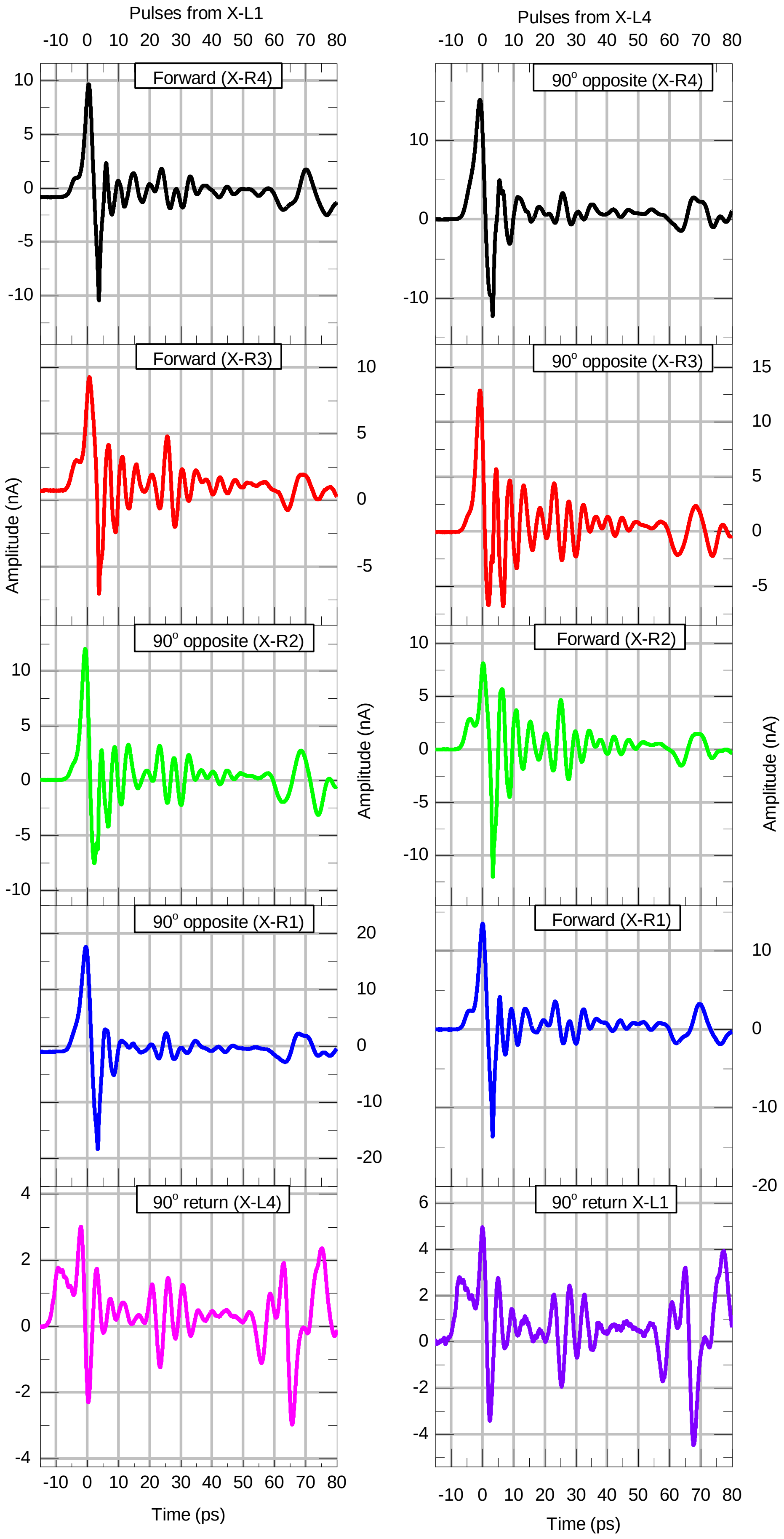

Figure 4.12: All possible "output" pulse combinations from switches X-L1 and X-L4.

In each of the measurements the amplitude of the oscillation is observed to briefly increase between 20 and 35 ps. The timing of this would correspond to a reflection from ~1 mm away from the detection switch, and could possibly be from a reflection at the detection switch that travels back towards the graphene region and returns to the switch. However, the measurements in Section 4.3 did not observe any reflections from the switch regions and, therefore, this is unlikely to be the source. Other sources of this feature should therefore be considered, including slow velocity plasmon propagation through the graphene.

The plasmon velocity in graphene has previously been measured using time-domain measurements,[34,129] and for other two dimensional electron gasses.[54] The time of flight of the plasmon through graphene was calculated in these experiments by comparing the arrival time of the cross-talk and the arrival time of the plasmon-coupled pulse. As the propagation distance was known and the cross-coupled pulse velocity has a much larger velocity, the plasmon velocity was established. This value is reported to be as high as 8×10^6 m s^{-1} and as low as 1×10^6 m s^{-1} (the Fermi velocity). For the pulses in Figure 4.12, the features around 25 ps correspond to a velocity of 2×10^6 m s^{-1}. This correlation is supportive in the case of plasmons, but is not a particularly strong proof of their presence due to the other oscillations that are present nearby in the time-domain. The experiments reported in literature changed the carrier concentration or applied magnetic field to manipulate the plasmons and change their behaviour.

However, an experimental configuration to test these variables could not be set up within the timeframe of this project.

The frequency responses of the signal generated at switch X-L4 and detected at each of the "output" switches is shown in Figure 4.13, where each of the signals is normalised to the mean square amplitude of the signal. For the measurements detected at the inner probe arm, which displayed the largest oscillations in the time-domain, larger peaks in power can be seen at 220 GHz. For all signals, the majority of the energy is confined to the sub-THz (<300 GHz) band.

Overall, the OC-THz-TDS measurements of this device demonstrated a number of features that are specific to this complex structure that are not typically seen in more common single wire PGL spectroscopy devices. The pulse scans and FFT spectra so far have all provided an introduction to the dynamics of the geometry but it is apparent that from these measurements, not a great deal can be directly attributed to the response of graphene. Modulation of the carrier dynamics of graphene is therefore

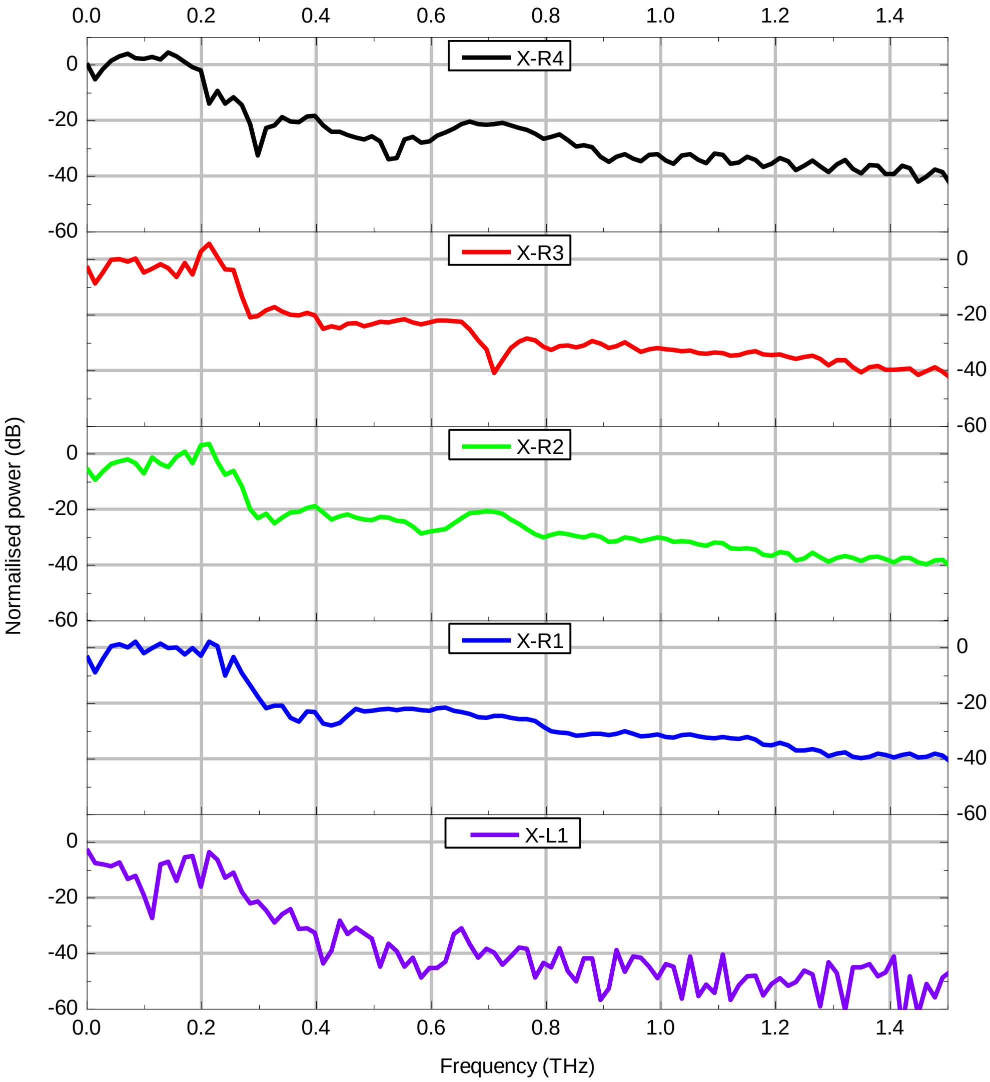

Figure 4.13: FFT of all "output" pulses generated at X-L4.

needed to allow a "locked-in" signal to be produced. This is done by measuring the difference signal from in one graphene state as it transitions to another, thus removing all the non-graphene components of the signal, such as probe arm resonances. Measuring the THz response of graphene under optical illumination was tested with this device and the setup and results of this experiment are described in the following section.

4.6 Optical pump – terahertz probe measurements of graphene

Optical excitation of graphene at room temperature has been demonstrated to display hot-carrier dynamics,[9] which are typically only observable in classical semiconductors at lower temperatures.[130,131] The techniques that are used to observe this response include

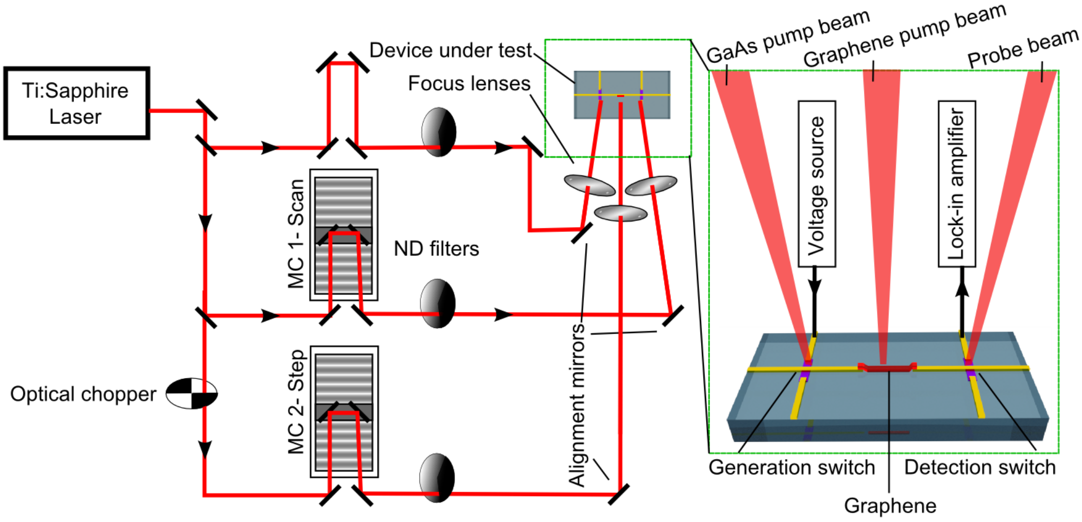

Figure 4.14: On-Chip optical-pump terahertz-probe schematic configuration. Each of the three path lengths from the Ti:Sapphire laser to the chip are approximately the same length. MC 1 and MC 2 are the motion stages that are used to control the two path lengths. The PGL design shown is for illustrative purposes only.

optical-pump optical-probe (OPOP) and optical-pump terahertz-probe (OPTP)[10,11,13] measurements. These use similar techniques to FS-THz-TDS to measure carrier dynamics with a sub-picosecond resolution. OPOP measures the change in the optical conductivity of graphene as a function of graphene optical excitation, but this only probes the high energy carrier distribution.[132] This is a particularly ineffective method for measuring hot-carriers in graphene because they gradually lose energy through many collisions and transfer energy via Auger scattering, rather than a single recombination event. This creates many lower energy carriers in the system that are not probed by OPOP.[10] OPTP, on the other hand, is much better suited to detecting changes in the distribution in gapless graphene, due to the lower energies associated with THz radiation.

Conventionally OPTP measurements are conducted using a modified FS-THz-TDS system. An additional motion controlled beam path is added to directly excite the sample under test. These measurements can observe the variation in graphene conductivity by monitoring the THz pulse amplitude as it passes through photoexcited graphene. If the graphene optical pump beam is faster than the graphene carrier dynamics, the hot-carrier relaxation time can be measured. To date, no known OPTP measurements of graphene have been conducted using an on-chip configuration. By using PGL waveguides as graphene contacts, the THz field interaction with the graphene is distinctly different and may produce enhanced results. To test this, the on- chip OPTP system configuration illustrated in Figure 4.14 was designed and implemented.

In this configuration it is important to note that the lock-in amplifier would detect whichever signal is chopped. Hence, if the optical chopper is positioned on only the "GaAs pump" or "probe" beam path, the full THz signal will be measured. However, when the chopper is on the "graphene pump" beam path, the conductivity is modulated. The resultant signal is the component of the "main" terahertz pulse that is altered by the conductivity change of the graphene. To obtain the largest signal amplitude, each of the ND filters was set to allow the maximum laser power to the chip. The splitting and optical chopping of the beams resulted in uneven powers at each illumination position. The power of each, before optical chopping, was ~10 mW for the GaAs pump, ~20 mW for the graphene pump, and ~9 mW for the probe beam, where each spot had a FWHM of ~24 μm. The duty cycle of the optical chopper was 50 % resulting in the power being halved for the chopped beam. The most powerful beam was used to pump the graphene so that the largest modulation of the signal could be achieved.

The PGL design XG-50 on device D3 (as characterised in Section 4.3) was selected for testing as it had been shown to have good LT-GaAs and graphene properties. Before measurements were made, the third beam path had to be calibrated. As the laser had a temporal profile, the optical pulse must arrive at the graphene in the same time range as the THz pulse. Therefore, the stage position that corresponded to this had to be evaluated. To check that the motion stage and optics were installed correctly, the "GaAs pump" and "graphene probe" beams were temporarily aligned to the "input" pulse

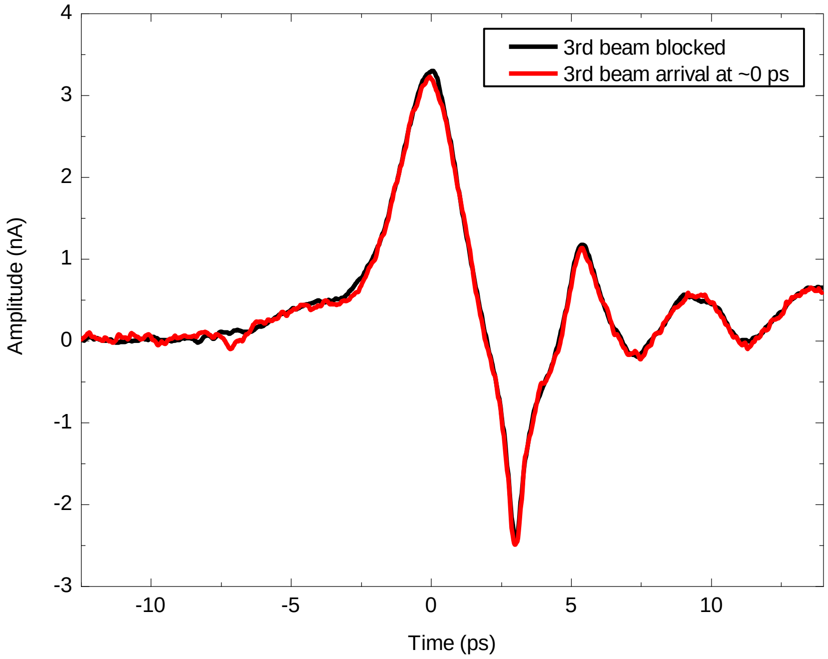

Figure 4.15: "Output" pulses as measured from X-L1 to X-R4, with and without illumination at the graphene region.

configuration and the time delay of MC 2 could then be calibrated. After normal operation of the third beam was verified, the "graphene probe" beam was positioned at the PGL/graphene interface by aligning to the photo-thermoelectric current (see Section 2.4.5). By using graphene picosecond pulse detection techniques, described in Chapter 5, an exact time delay between the "GaAs pump" beam and the "graphene pump" beam could be established. The time of flight from the generation switch to the graphene was ~6 ps for a propagation distance of 1 mm.

To obtain an understanding of what proportion of the THz signal was being modulated, two full terahertz scans were performed (with the "GaAs probe" beam chopped), with and without "graphene probe" beam illumination. These are plotted in Figure 4.15 and it is clear that it was difficult to notice any major differences in the pulse above the background noise level.

The difference configuration was then set up as shown in Figure 4.14, where only the graphene THz photoconductivity modulation was measured. As the setup had two computer controlled motion stages, multivariable measurements could be taken, where the time-domain scan was measured as a function of the stage MC 2 position (graphene illumination time). Figure 4.16 shows the result of these measurements where the solid traces from left to right on the x-axis are the THz scan difference signals, measured by sweeping MC 1. It should be noted that the amplitude of the pulse is not in phase with the larger peak and may represent increased transparency or absorption, and the time 0 ps in this instance corresponds to the beginning of the scan and not the peak of the pulse as in other measurements. The position of stage MC 2, plotted from front to back on the y-axis, represents the change in arrival time of the graphene probe beam. The largest modulation of the signal (i.e. the largest current value), is expected when the optical pulse arrives at the graphene at the same time as the THz pulse. This can be seen at stage position 32.2 mm.

The power of the "graphene pump" modulated signal, in comparison to the total transmitted pulse power (Figure 4.15) is −46 dB, and is almost undetectable on a linear scale, even in ideal noise conditions. In free space OPTP measurements the conductivity of graphene is modulated and the entire terahertz pulse has to travel through the graphene sheet, hence, a larger modulation is observed of ~5 % (−13 dB).[133] The polarity of optical modulation of the terahertz conductivity has been reported to be a function of the Fermi energy in the graphene, where values below 100 meV result in optically induced terahertz transparency, and Fermi energies above this have increased terahertz absorption due to longer scattering rates.[37] As the graphene used in this experiment had a Fermi level of 286 meV, optically induced absorption is expected. In contrast to the free space OPTP experiments, graphene configured parallel to the pulse propagation, such as in this experiment, is not acting as a transmission medium in the same way as free space OPTP, and could be considered to be a variable conductivity transmission line. The change in signal, therefore, could either be due to the change in the graphene transmission line properties, or the modulation of plasmon signals traveling inside the graphene layer itself.

As mentioned before, the plasmon velocity is much slower than the PGL mode velocity. The peak signal in these measurements corresponds to the arrival time of the PGL mode, and the plasmon propagation is expected to arrive tens of picoseconds after this. It can be deduced that the main signal here is not associated with plasmons and is instead the modulation of behaviour of graphene acting as a transmission line. It should also be

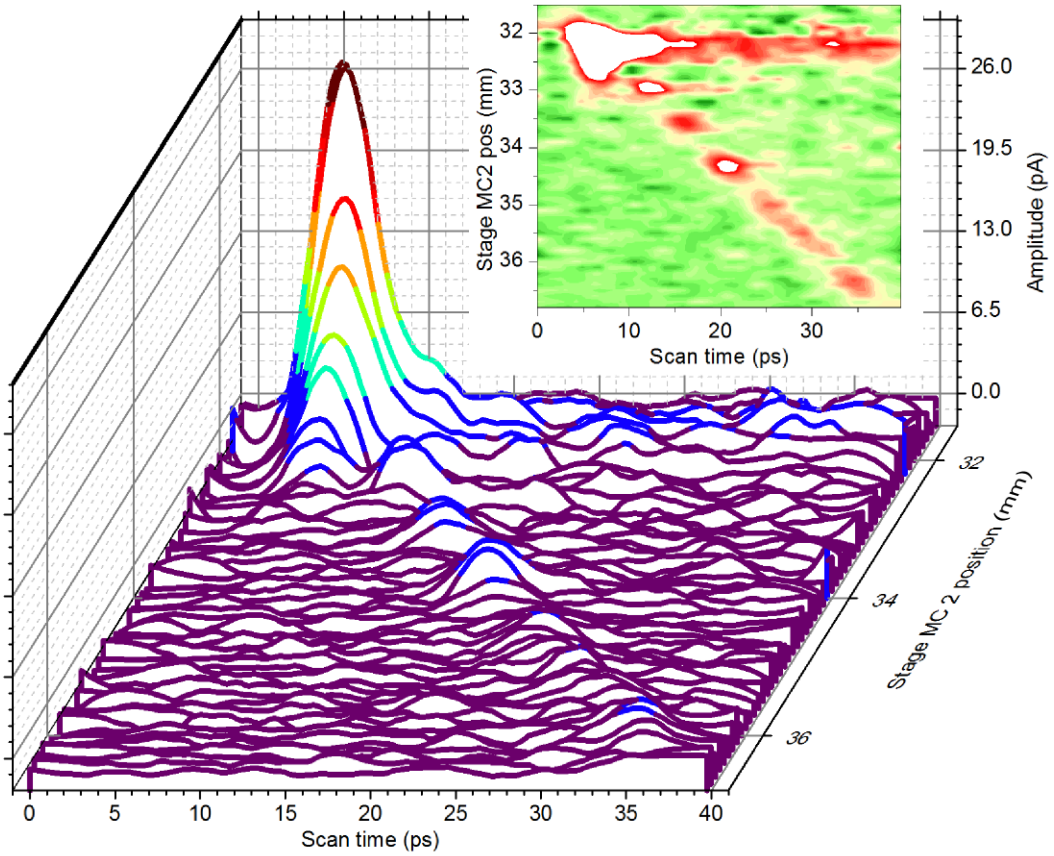

Figure 4.16: Optical-pump terahertz-probe measurements for pulses generated at X-L1. X-R4 was illuminated by the probe beam and scanned from 0 to 40 ps. The graphene region probe was incrementally stepped after each scan by 0.1 mm in the range 31.5 to 36.8 mm. The colour scale is a guide for the eye. (inset) 2D contour image of the same data. The colour scale has been arbitrarily adjusted to emphasise the diagonal feature.

noted that the feature observed at ~25 ps in Section 4.5 is also not seen and that feature must be attributed to a non-graphene based feature, such as a reflection.

An interesting feature of Figure 4.16 is the small pulse which can be observed in most scans, which is highlighted in the inset, appearing across the diagonal (top-left to bottom-right). This behaviour represented a small amplitude pulse with an increased delay for larger values of stage MC 2 position and was found to be independent of the signal generated by the GaAs probe beam. This evidence indicated that a pulse was being generated at the graphene region under excitation by the graphene probe beam, without the need of an external bias. Photoexcited carriers near the graphene/metal interface are accelerated due to a diode-like semiconductor interface, formed by different graphene doping levels at the gold and quartz. Picosecond timescale photocurrent from un-biased graphene has previously been reported,[40] and the photo-thermoelectric mechanisms that are responsible for this effect are discussed in more detail in Chapter 5.

For the purposes of understanding the change in pulse propagation with optical graphene probe, the main peak contains the most information. From the left to the right of this peak shows the gating properties of the graphene as the THz pulse passes over it. From the top to the bottom of the pulse (on the y-axis) directly shows the graphene temporal change in conductivity. The latter value is typically the only result which is analysed in

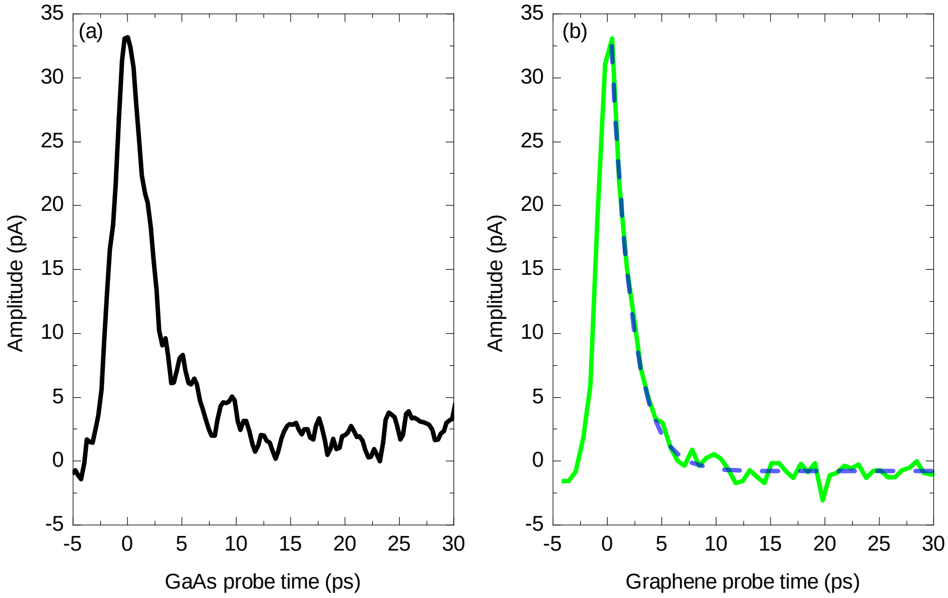

Figure 4.17: Single dimension plots extracted from the OPTP data. (a) The THz scan taken with the probe beam fixed at 32.2 mm. (b) The data taken along the y-axis at the maximum pulse position. The blue dashed line is the exponential decay fit of the pulse after 0 ps with a time constant of 1.9 ps.

OPTP measurements. For clarity, each of these two cases are extracted from the raw data and plotted in Figure 4.17.

Figure 4.17 (a) is the change in the THz "output" pulse when the graphene is illuminated with a 100-fs-long duration laser pulse. The result is a convolution of the incident terahertz pulse and the temporal graphene conductivity change. As the FWHM of the peak is 4.2 ps wide, and the THz pulse is known to be in the 1.65 to 3 ps range, it can be understood that the time-scale for the change in graphene conductivity is also in the few-picosecond range. This means that the carriers in graphene are excited very quickly and relax in a matter of picoseconds as opposed to nanoseconds for intrinsic semiconductors. These fast carrier dynamics are well known to be attributed to the photo-thermoelectric effect in graphene,[115] and the relaxation rate is consistent with OPTP measurements of CVD graphene using perpendicular THz interaction with the sample.[13]

A more accurate measurement of the electron-hole generation and recombination rate is shown in Figure 4.17 (b). This shows the variation in peak THz pulse amplitude as a function of the graphene sampling pulse arrival time. As the graphene is optically excited, its conductivity changes, and this variation in conductivity affects the amplitude of the pulse. Therefore, the change in amplitude directly represents the relaxation dynamics of the graphene, rather than a convolution of it with the THz pulse.

Previous OPTP measurements of graphene have established that the relaxation dynamics of graphene are described by a hot-carrier system.[115] Carrier-carrier collisions in the first 100 fs after the "graphene pump" illumination result in the photoexcited electrons gradually losing energy through impact scattering (or Auger scattering), whilst secondary hot electrons are promoted from below the chemical potential. Initially, this conserves the energy of the system in an electronically conducting state rather than losing the energy to the lattice and hence the electron temperature exceeds the lattice temperature. The cooling of hot electrons is achieved through phonon emission, where optical phonons are only emitted above 200 meV, because of the strong carbon-carbon bonds. Below this energy acoustic phonons emission occurs, but is inefficient due to a mismatch between the Fermi and sound velocities.[134] The hot-carrier cooling rate has been reported to be in the region of 1 to 100 ps.[115] The cooling rate for the experimental data presented here has an exponential decay with a time constant of 1.9 ps is plotted as a blue dashed line in Figure 4.17, and is very similar to the values obtained in free-space OPTP measurements of monolayer graphene.[10,106,133]

The effect of the terahertz conductivity of graphene using an on-chip OPTP configuration is complex. The polarity of the signal could indicate a decrease in conductivity if the graphene is modelled as a lossy load, or it could also indicate an increase in conductivity if it is modelled as a continuous transmission line. Free-space measurements of hot-carriers are a much more appropriate method of measuring this, and have shown that the terahertz conductivity is affected differently for multi-layer and mono-layer graphene. For multi-layer graphene an increase in conductivity is observed (decrease in signal) which is expected due to increased carrier concentration (Drude model).[11,12,26] Mono-layer graphene, however, has demonstrated decreased conductivity at low doping levels.[10,106,133] This mechanism behind optically induced "bleaching" is debated, but has been attributed to either an electron-phonon scattering induced suppression of free-carrier conductivity,[133] or stimulated emission of THz radiation.[106]

Although an on-chip OPTP experimental configuration has complimented the data recorded using similar free-space systems, it has not demonstrated any advantages to measuring the properties of graphene in this way. It has, however, confirmed that the relaxation dynamics of hot-carriers in graphene are of the same order of magnitude as LT-GaAs. Materials that have ultrafast carrier dynamics are rare and may have technological relevance to terahertz applications. One such application, photoconductive switching, is discussed in detail in the following chapter.

4.7 Conclusion

The development of on-chip THz TDS systems for graphene has been demonstrated. A multi device on-chip system was designed to improve the yield and throughput of graphene devices. Testing of this device revealed that relatively strong oscillations were generated from the probe arms, but did not prohibit measurements from being made. The traditional "output" pulse spectroscopy results of graphene were mostly inconclusive as differentiation effects from the capacitance of the graphene probes dominated the time and frequency-domain information. This made it very apparent that a differential type measurement had to be made using magnetic fields, carrier concentration, or carrier excitation. The latter was chosen and the on-chip optical-pump terahertz-probe configuration was expanded to the existing OC-THz-TDS system. The results showed very small modulation properties, but transient carrier dynamics were observed with durations in the region of a few-ps.

Chapter 5: Graphene terahertz emitters and detectors

5.1 Introduction

Gallium arsenide (GaAs) is used extensively in high speed electronics, where low temperature grown GaAs (LT-GaAs) is of particular importance to the terahertz frequency range. It is used as an emitter/detector in THz-TDS systems, where both the material and the femtosecond lasers required to excite the carriers are costly (the latter costing ~£100k at the time of writing), therefore, a great deal of research into alternative lower band gap materials such as InGaAs has been conducted.[135] These will allow use of the 1.55 μm wavelength lasers, which are relatively cheap, since they have been extensively developed by the telecommunications industry. As graphene has zero bandgap, has fast carrier dynamics, and can be produced in a number of cost effective ways, it has the potential to be a powerful tool in the development of terahertz devices; alongside, or instead of, LT-GaAs.

This chapter presents the results of experiments on graphene-based photoconductive emitters and detectors as a compliment to LT-GaAs on-chip terahertz devices. Graphene, in some respects, is less than ideal compared to other photoconductive materials, owing to its relatively high conductivity under dark conditions. However, it is demonstrated here that it can generate and detect pulses at THz frequencies very efficiently. Pulses detected by graphene are shown to linearly respond to the incident electromagnetic field and at lower laser probe powers. A sub-linear amplitude relationship with higher laser powers is also shown, owing to larger carrier concentrations affecting the mobility of the graphene sheet. Graphene-generated pulses are also demonstrated, and have a similar response under applied field and laser power. Finally, the first steps towards on-chip pulse generation and detection using only graphene are discussed, alongside an estimation of the intrinsic response times of the devices which were developed. Please note that the main results contained in this chapter were published in Nano Letters.[136]

5.2 On-chip graphene terahertz detectors

5.2.1 Experimental setup

Photoconductive detection of THz pulses was performed using the OC-THz-TDS device D3 and specifically geometry XG-50, as discussed in Chapter 4. This device had the ability to test both the generation and detection of pulses from any combination of LT-GaAs and graphene switches. This section predominantly discusses results from the device as shown in Figure 5.1, where the graphene area used had a cross-shaped geometry with four 9-mm-wide planar Goubau line (PGL) contacts, each integrated with a pair of LT-GaAs switches for THz pulse emission. The distance between the left and right switches was 2 mm, and the length of the PGL from each LT-GaAs emitter to the graphene contact was 1.07 mm. For simplicity, the notation used in this chapter differs from Chapter 4, as only the results from two LT-GaAs switches are presented. Data was collected using the other switches on the device, but the differences were very subtle and do not add to the discussion. The primary LT-GaAs switch, LTA, was the emitter/detector for graphene pulses, however, LTB was also used for "input" pulse measurements in combination with LTA. GO1 refers to the closest graphene/metal interface and GO2 is the furthest away.

On-chip measurement techniques similar to those discussed in Chapter 4 were used to obtain "input" pulse measurements from the LT-GaAs switch pairs throughout. To achieve beam alignment to the graphene/metal interface, for the graphene pulse detection measurements discussed in the current chapter, the position of maximum graphene photocurrent (generated by the photo-thermoelectric effect) had first to be located. A lock-in amplifier was connected to C3, while the opposing contact C2 was grounded, and the perpendicular contacts, C1 and C4, were left floating so that photocurrent could not be generated by these areas. The points GO1 and GO2 represent the two locations of highest magnitude DC photocurrent of opposing sign, which could then be alternated by changing the reference phase of the lock-in amplifier by 180°. The switch used for terahertz pulse emission was biased using a Keithley source meter connected to contact P1 as shown in Figure 5.1 (a). In order to obtain a "conventional" pulse polarity, whereby the leading edge shows a rise in current when generated by a

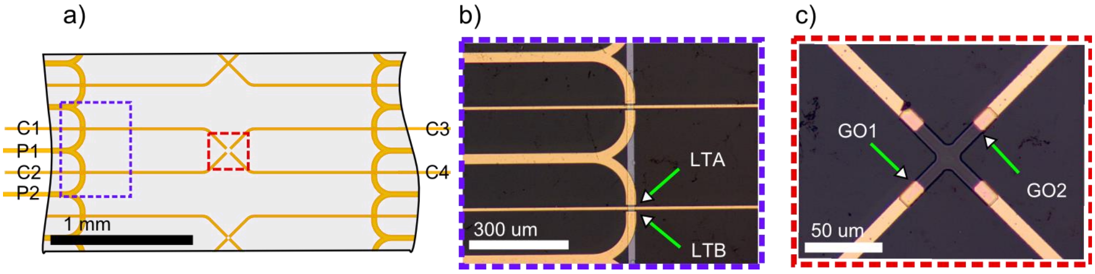

Figure 5.1: Experimental device geometry. (a) Schematic of 2 mm X-geometry device with 50 μm gap. Graphene contacts labelled C1 – C4. LT-GaAs probe arms labelled P1 and P2. (b) Optical image of LT-GaAs switch region with 30 μm probe arms and 9-μm-wide PGLs. (c) Optical image of graphene and PGL contacts. The distance from GO1 to GO2 is 50 μm and the graphene width is 9 μm.

positive voltage, the lock-in amplifier was phase locked to the most positive real signal obtained at GO2.

The laser beam was aligned to the LT-GaAs switch using a 100 mm focal length lens to produce a beam spot of 24 μm. The chopped probe beam used for the graphene switch was either focussed to 24 μm using a similar lens, or to ~5.5 μm using a 35 mm focal length 10 × NIR objective lens. The typical operating power when employing a 24 μm spot size was 10 mW, and 1mW when using the 5.5 μm spot (in order to minimise the risk of damage to the graphene). The LT-GaAs bias voltage used was 30 V in all cases, unless explicitly stated later.

Other devices were tested to support the results and, geometrically, were iterative modifications of the aforementioned device. These modifications consist of:

- Another cross-geometry, fabricated with a 30 μm separation from GO1 to GO2 with the same 9 μm width. All other dimensions were unchanged.
- A two-terminal graphene geometry with two straight PGL contacts (rather than four meeting at a cross). The graphene patch in this case was a 5 × 9 μm rectangle and was located 500 μm away from the LT-GaAs switches.

All geometries were fabricated on 500-μm-thick quartz using a 350-nm-thick LT-GaAs layer annealed ex-situ at 575 °C. The gold was 80nm thick and the CVD graphene, purchased from Graphene Square, was transferred using PMMA and attached to the top surface of the contacts. The PMMA layer was then removed, replaced with S1813, and optical photolithography was then used to mask the desired graphene channels from a 3 minute, 50 W plasma ash. The S1813 remained on the device throughout testing to provide structural support at the edges of the 80 nm gold contacts, and to minimise carrier concentration fluctuations due to atmospheric absorptions.

5.2.2 Results and discussion

OC-THz-TDS detection of a few-picosecond pulse is demonstrated in Figure 5.2 (a) using a cross-geometry graphene switch with detection occurring at GO1. This is plotted (normalised) alongside the reference "input" pulse (LTA to LTB) in Figure 5.2 (b). The observed response is similar to that of LT-GaAs switches, and displays a fast response time with a FWHM below 3 ps. Also present in the signal, however, is a DC current contribution (which is not typically seen in LT-GaAs) of a similar order of magnitude to that of the pulse. The dispersion of the pulse detected at GO1 for this device is quantified to a 67 % increase in the FWHM of the "input" pulse, and may be expected to arise owing to a combination of the carrier dynamics in the graphene, and the dispersion produced by the PGL. As discussed later in this thesis, the pulse width detected by graphene is a function of optical power and detection spot location, and can vary from 2.8 ps to 3.7 ps with similar "input" pulses.

To evaluate what contribution of the dispersion is from the PGL, a comparison of two pulses detected with graphene and LT-GaAs using similar switch geometries would be conducted. This was not possible due to time constraints, however, two pulses were compared that had similar FWHM values of ~1.65 ps, one detected at graphene, 1.07 mm away from the generation switch, and the other by LT-GaAs, 2 mm away from the generation switch. These are shown in the inset of Figure 5.2, where the FWHM with respect to the propagation distance indicates that the carrier dynamics of the graphene are slightly slower than that of LT-GaAs, assuming increased phase dispersion on the extra length of PGL line. There are many more variables between these measurements that will affect the detected pulse dynamics, including switch geometry, but the important outcome of this is that graphene has excellent properties for photodetecting picosecond pulses with no (intentional) modification to its composition. This is something that very few standard semiconducting materials can achieve.

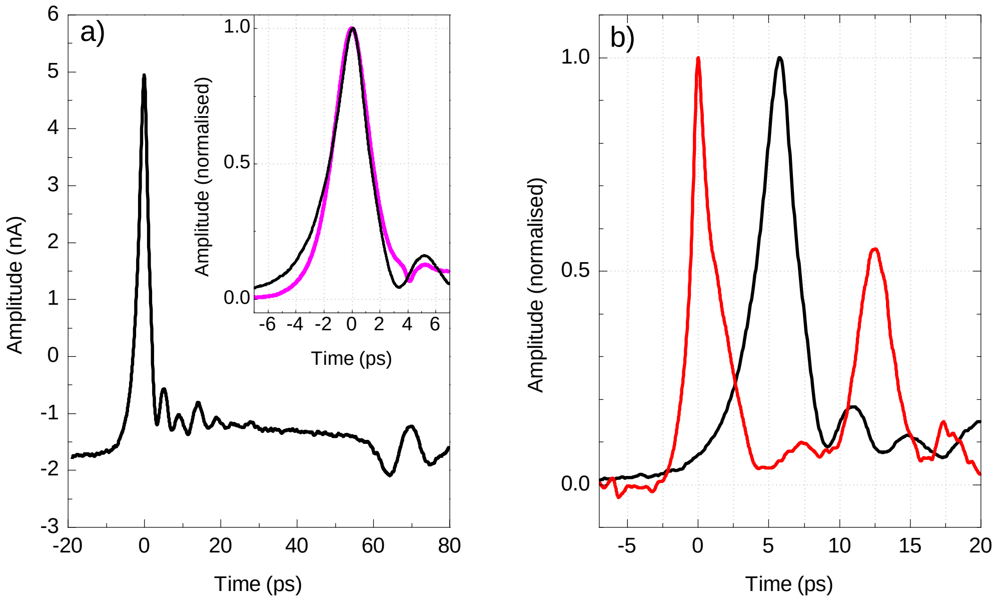

Figure 5.2: Detection of picosecond pulses emitted by LT-GaAs and detected by graphene. (a) Raw pulse detection. Demonstrating a signal amplitude greater than 6 nA at 10 mW laser power with a DC offset of -1.8 nA. Features at 60 ps are due to bond pads. Inset) Comparison of graphene detected pulse after 1.07 mm (black) and LT-GaAs detected pulse in another device after 2 mm (pink). (b) LT-GaAs "input" pulse (red) and graphene detected pulse (black) measured in the same scan range showing pulse propagation times. The reflection of the "input" pulse at 12.5 ps is due to the impedance mismatch at GO1.

As the characteristics of the pulses detected by graphene and LT-GaAs were so similar, it was vital to rule out any residual LT-GaAs contamination of the sample surface, which could contribute to the pulse detected at GO1. To do this, two methods were used. First, Raman spectroscopy of the device was conducted very close to the GO1 switch area and compared to a reference sample of quartz and LT-GaAs. The Raman data (Figure 5.3) from near the graphene switch was effectively identical to the quartz reference and, critically, showed no photoluminescence at 290 cm^{-1} (the strongest resonance observed in LT-GaAs). For the second method, separate devices were fabricated where special care was taken to completely spatially separate the area where the LT-GaAs was transferred/etched and the location of the graphene detection switch. It was found that such devices were also capable of detecting similar THz pulses and, hence, this effect was not due to LT-GaAs. These devices are discussed in detail in Chapter 6.

As the influence of contamination was ruled out, a more detailed analysis of the results was conducted to understand the performance of graphene as a detector of picosecond pulses. The time-domain spectra of graphene showed oscillations immediately after the main pulse and decay within 20 – 25 ps of the peak, the strongest of which occurred with a period of 4.5 ps (~220 GHz in the frequency-domain). The source of this resonance was the design of the probe arms, and has been discussed in Section 4.3. The FFT of this

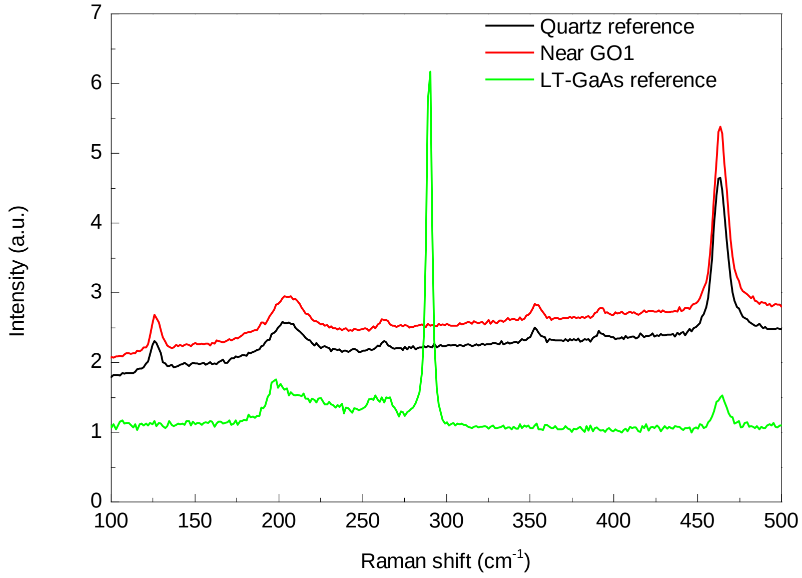

Figure 5.3: Raman spectra for clean quartz (black), LT-GaAs as measured near LTA (green) and an area of quartz very close to the graphene/metal interface GO1 (red). The scan of area near GO1 was repeated for 5 distinct locations but no peak at 290 cm^{-1} was found.

pulse, plotted in Figure 5.4, was directly compared both with the "output" pulse which passed over the graphene gap and with the "input" pulse. The "input" pulse produced frequencies beyond 2 THz before approaching the noise floor. The graphene pulse signal fell below the noise floor above 600 GHz and the "output" pulse approached the noise floor sharply after 200 GHz. The graphene detected pulse displayed clean spectral response and low standard deviation up to 250 GHz, although the resonance expected at 220 GHz (as seen in the time-domain), was barely observable due to its relative amplitude to the main pulse and the fast dampening rate of the oscillations.

In order to gain an insight into the maximum operating frequency of the graphene detector, all the detection pulses for a range of devices were compared. It was observed that for all three different geometries that the FFT begins to increase in noise/standard deviation at 250 GHz, and falls below the noise floor at 600 ± 100 GHz. This frequency bandwidth may be limited by a number of factors including the switch geometry or a limit imposed by the graphene carrier dynamics. Dedicated studies of each of these factors are suggested for future work in order to determine if any fundamental properties of graphene limit its performance.

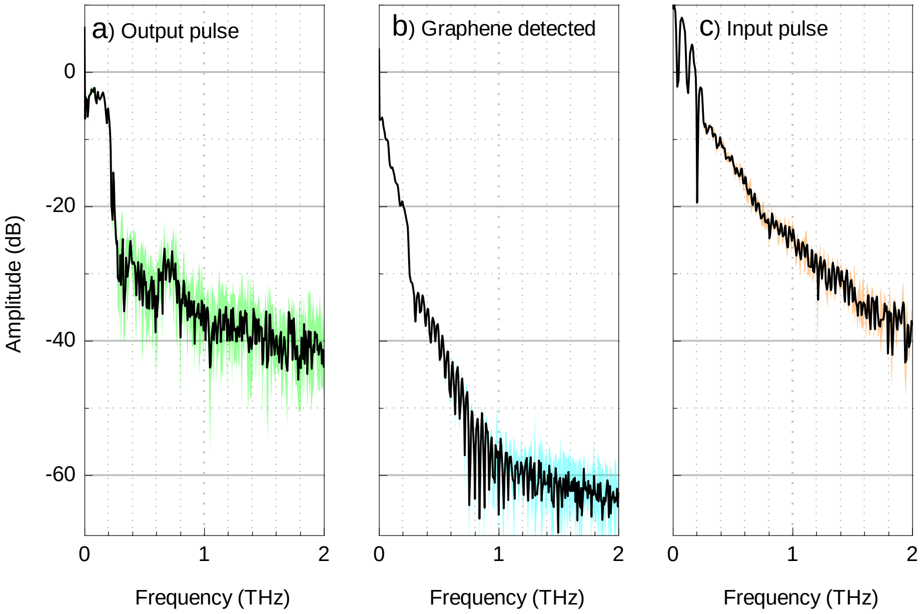

Figure 5.4: Frequency-domain data for terahertz pulses detected after passing over the graphene, at the graphene and at the emission source. Frequency averaged data over 3 scans is shown in black and ±1 standard deviation is plotted in colour. (a) "Output" pulse after passing through the graphene/gap region. (b) Graphene detection at GO1. (c) "Input" pulse for the same device.

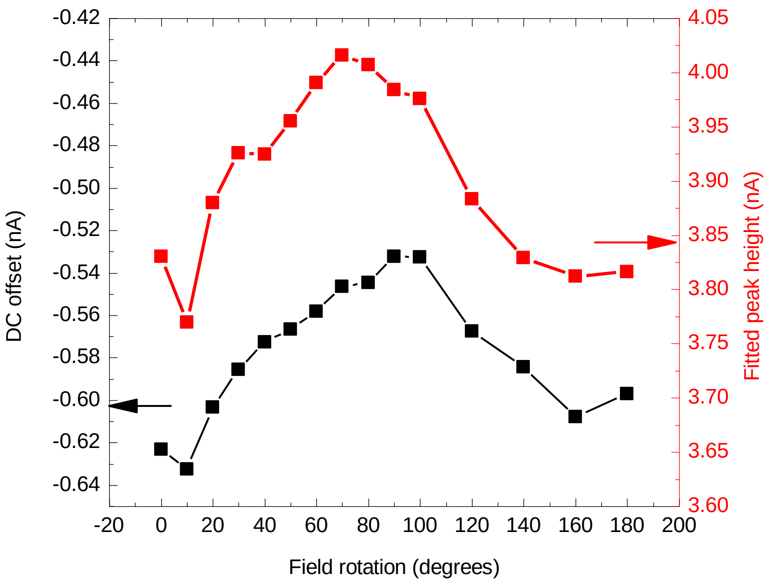

Figure 5.5: Variation of DC offset (black) and total peak height (red) as a function of probe beam polarisation.

To investigate the mechanisms by which graphene detects the terahertz pulse, an understanding of how the graphene is interacting with the light is necessary. As graphene is heavily researched at lower frequencies in comparison to THz frequencies, the DC component of the graphene detected pulse will be discussed first. The two mechanisms responsible for DC photocurrent generation in graphene consist of the conventional inner photoelectric effect that is seen in typical III-V semiconductors, and the photo-thermoelectric effect which is discussed in detail in Section 2.4.5. The dependence of polarisation on the DC offset was studied by Echtermeyer *et al* and can be used to determine the overall contribution of each effect.[137] The effect of polarisation on both the DC offset and the height of the pulse are shown in Figure 5.5. The results indicated that the PTE effect was the dominant mechanism since the rotation of the polarisation by 90 ° only changed the AC amplitude by ~7 % and the DC offset by ~18 % of the total effect.

In order to explain the variance of the photocurrent with illumination, it should be understood that the PTE voltage is given by[138]

$$V_{PTE} = (S_1 - S_2)\Delta T \tag{5-1}$$

where S_1 and S_2 are the Seebeck coefficients for the graphene at each side of a junction and ΔT is the temperature increase in the hot electrons. In this device, the Seebeck coefficients S_1 and S_2 represent the graphene area that is in contact with the quartz substrate and S1813, and the area that is in contact with the gold and S1813 respectively. In order to generate a photocurrent, the beam must illuminate both regions. When the spot is entirely over one of these two areas, no difference in Seebeck coefficients means that no photovoltage will be generated as $(S_1 - S_2) = 0$. At the graphene/metal interface, however, a photovoltage is produced under illumination due to the contribution of the two distinct concentrations in graphene at either side of the interface. It should be noted that because the graphene in these devices is transferred above the gold, both sections of the graphene are generating hot carriers. Using numerical calculations based on density-functional theory developed by Khomyakov *et al*,[139] the carrier concentration of the graphene-on-gold is a p-type doping approximated to be $2.6 \times 10^{12}\ \mathrm{cm}^{-2}$ (estimation based on un-doped graphene at $T = 0$). The carrier concentration of the graphene in the quartz is determined to also be p-type by using Raman spectroscopy (as described in Section 3.3.2), but is expected to be 2 or 3 times larger than the gold region at $(6 \pm 2) \times 10^{12}\ \mathrm{cm}^{-2}$. This forms a p'-p interface that, when illuminated with 10 mW of power, generated a DC current of the magnitude nano-amps through 4 kΩ of graphene. The polarity of the current was also observed to reverse sign when the beam position moved from GO1 to GO2, as this had the effect of flipping the concentrations relative to the measurement apparatus and, hence, the reversal of the direction of the current. It was observed, however, that the polarity of the THz pulse remained the same at these two measurement points, indicating that the current generation by the PTE effect is not directly attributed to the detection of the fast THz pulse.

It is proposed that the AC detection mechanism is due to a local change in the conductivity, and hence an increased current flow is seen at the sampling time when an AC voltage bias is created by the incident THz field. As graphene absorbs 2.3 % of all incident light[8] and almost all photons generate e-h pairs, the estimated change of the carrier concentration when the sampling beam illuminates the graphene is

$$\delta n(P) = \alpha \frac{P}{SrE_g}, \tag{5-2}$$

where α is the fine-structure constant, P is the average illuminating power (20 mW), E_g is the energy of the laser (1.6 eV), r is the number of pulses per second, and S is the area of the spot. An expected change in concentration is in the region of $\sim 6 \times 10^{11}\ \mathrm{cm}^{-2}$, which is one order of magnitude smaller than the doping level of the graphene. However, this number only accounts for the carriers that are excited immediately after excitation, and carrier multiplication is known to occur in graphene.[10] This means that the true number of carriers is estimated to be as large as 4 carriers per absorbed photon when using a laser energy of 1.6 eV and a Fermi energy of 286 meV (as determined from Raman spectroscopy of this sample).[140]

To further investigate the AC dynamics, measurements were taken at the same location for a range of different terahertz field magnitudes in order to determine if the detection was a linear process. The results, obtained by measuring the "input" pulse and the pulse detected at GO1 whilst varying the LT-GaAs generation bias, are plotted in Figure 5.6. They show that for a linearly scaling pulse amplitude of "input" signal from the LT-GaAs, the response of the graphene was also linear. In parameter fitting of the pulse detected at GO1 using a Lorentz peak fit for the range of –10 ps to 2 ps, it is also observed that the area under the curve scales linearly with the THz field. This is a typical (and desirable) characteristic for a THz photoconductive switch employed in

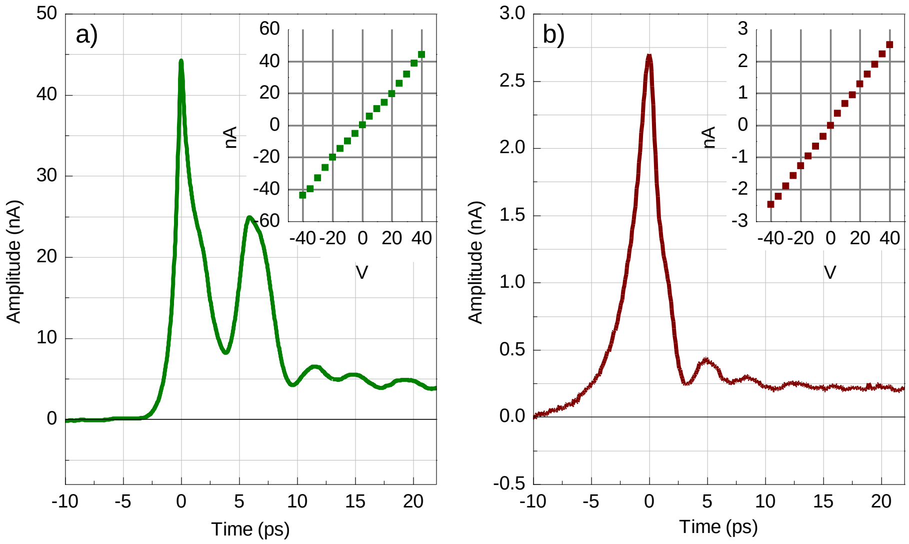

Figure 5.6: Pulse amplitude as a function of LTA bias voltage for the straight geometry device. (a) "Input" pulse at 40 V with reflection at 6 ps for shorter 1 mm propagation distance with maximum amplitudes for each bias voltage inset. (b) Graphene detected pulse for straight device at 40 V, also with maximum at each bias shown in the inset.

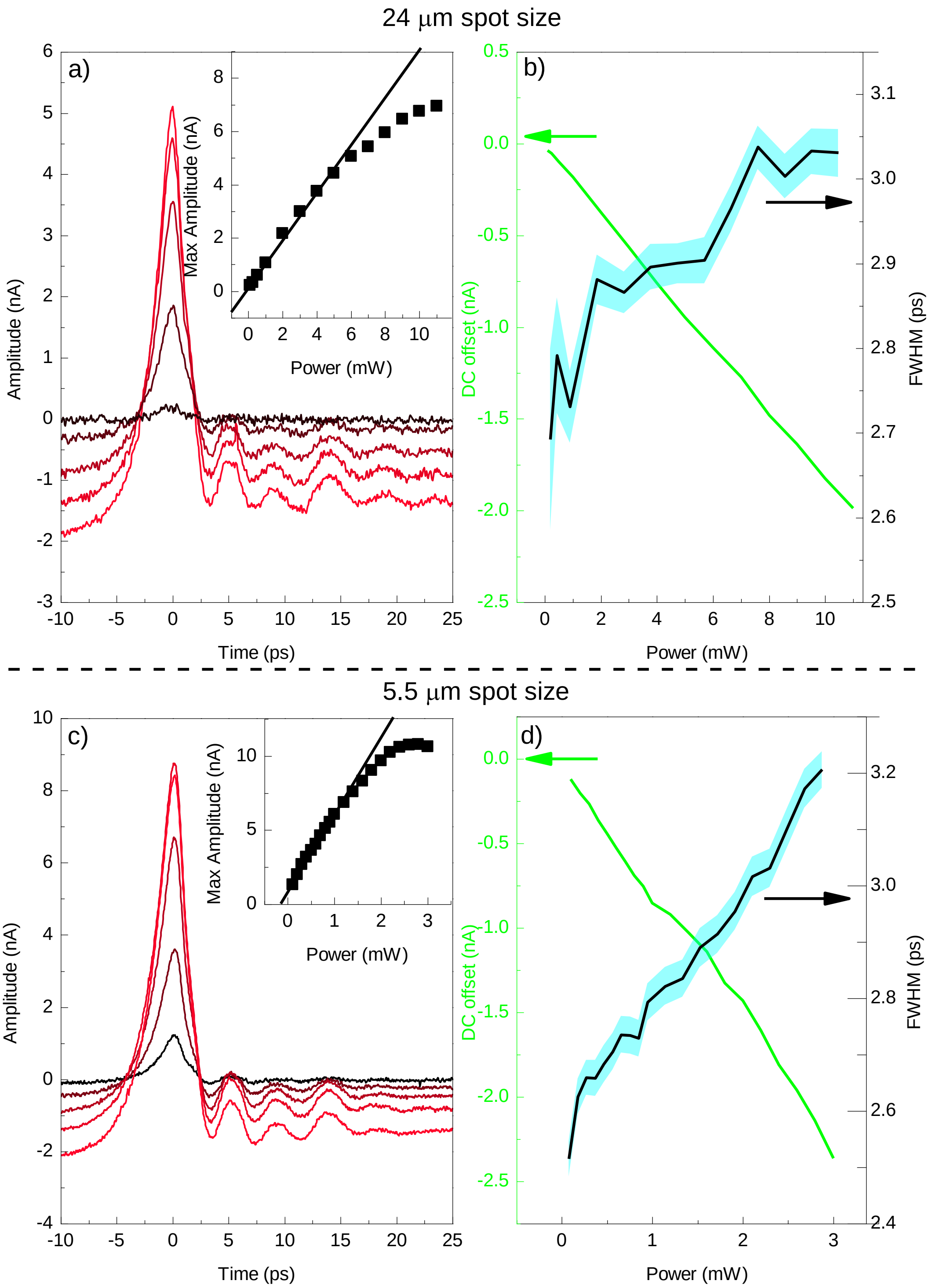

Figure 5.7 Graphene detected pulses as a function of probe beam power using large and small spot sizes. (a) Pulse measurements for an evenly incremented range of powers from 0.1 to 11 mW for the 24 μm spot size. Inset is the maximum amplitude for each measured power with a linear fit to guide the eye. (b) The DC offset (green) and FWHM (black/blue) as a function of power using the 24 μm spot. The blue shadow is the standard deviation of the fit. (c) Pulse variance with evenly spaced powers in the range 0.1 to 3 mW for the 5.5 μm spot. The inset shows maximum amplitude for each power. (d) DC offset and FWHM for each corresponding power in (c).

OC-THz-TDS, since it does not need a non-linear scaling function to be applied to the detected pulse, and an accurate frequency response can be obtained.

The pulse amplitude measured at GO1 was not linear as a function of probe power, however. The full pulse is shown in Figure 5.7 (a) as a function of probe powers, while the inset shows the relationship between maximum amplitude of the pulse and the maximum power used. A linear dependency was found for the lower powers, and a sub-linear response is observed at higher powers. The crossover point for these two responses occurs at around 4 mW, from whereupon it then increases with a power-law dependence, with an exponent equal to ~0.6. In this high power regime the conductivity change is proportional both to the change in carrier concentration and change the in mobility under laser illumination $\delta\sigma(P) \sim e\mu\delta n(P) + en_0\delta\mu(P)$, where n_0 is the carrier concentration without illumination. Below 4 mW the laser power is low enough that the light produces a negligible change in mobility and, hence, the conductivity change is directly proportional to concentration $\delta\sigma(P) \sim e\mu\delta n(P)$.

Graphene-based detection of THz pulses was repeated using a smaller 5.5 μm spot size and using the rectangular strip geometry in order to decrease the spatial region of illumination (device D4, design SG-50). The response using a smaller spot is shown in Figure 5.8 (a), with a direct comparison of the pulse detected using each spot size for the same power as shown in Figure 5.7 (c). The profile of both pulses was very similar, but there was a significant increase in amplitude for the smaller spot. To understand why this

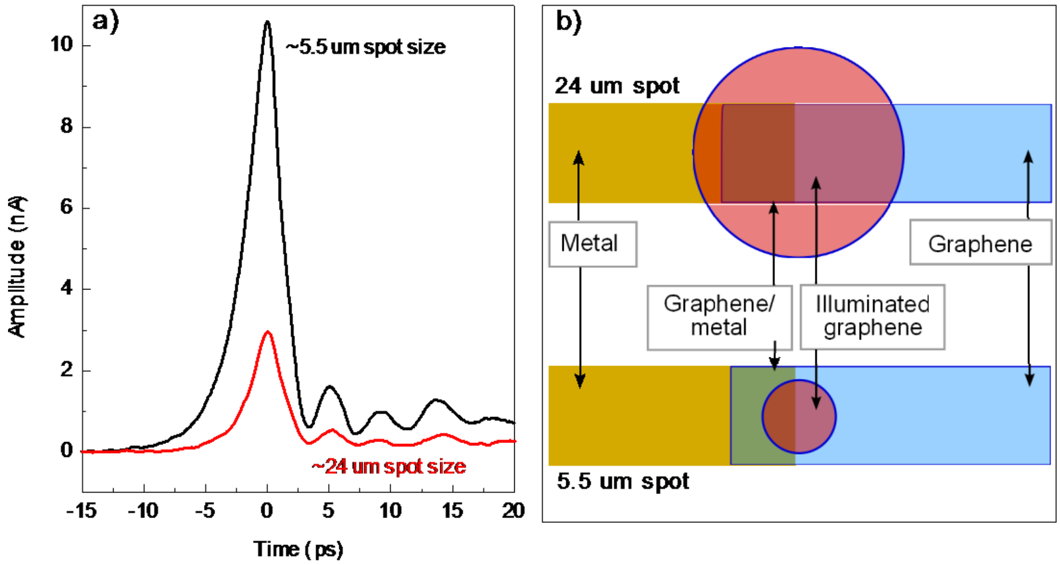

Figure 5.8: "Input" pulse amplitude for large and small spot sizes. (a) Direct comparison of large and small spot size using 3 mW powers. (b) Schematic of the spot size in comparison to the PGL/graphene interface. The red circle represents the FWHM of the beam.

occurs, the configuration of the graphene/metal interface is illustrated in Figure 5.8 (b) where the FWHM of the laser spot, which contains 94 % of the lasers power, is overlaid in red. A large portion of the power of the larger spot is not incident on graphene and either hits the quartz or is reflected by the PGL. The smaller spot, however, concentrates almost all of its power onto the graphene leading to a significantly higher carrier population per unit area.

In addition to the offset and peak amplitude changing as a function of illumination, the FWHM of the pulse was also observed to increase by up to 19 % over the range of powers measured as shown in Figure 5.7 (b) and (d). This behaviour was not observed in LT-GaAs "output" pulse measurements to the same extent; they only varied by 5 % over a similar power range. The FWHM scales linearly for the entire range of measurements and is much more apparent when using 5.5 μm spot sizes. A cause of this could be due to an increase in hot-carrier temperature at higher powers, and hence causing the slower pulse dynamics. In order to understand this fully, however, the pulse dependency as a function of bath temperature should be measured, but this could not be performed with the experimental facilities available.

The power absorbed by the graphene is not the only consideration when using varied spot sizes; the distribution of power across the width of the switch is also an important factor. If the illumination of the beam is considered to be approximately uniform when the spot is double that of the width of the graphene (w), the lumped element representation is simplified as the conductivity change is across the entire width of the switch. When the spot is reduced to a size where it is smaller than w, the lumped element model becomes more complex as the parallel resistance of non-illuminated graphene regions will reduce the resultant modulation. For this reason it is expected that as the spot sizes become significantly less than w, they may produce diminishingly lower pulse amplitudes.

5.3 Picosecond pulse emission by biased graphene switches

5.3.1 Experimental setup

The configuration for the generation of picosecond pulses from graphene required some small modifications from the detection scheme and is shown in Figure 5.9. The Keithley source-meter was applied directly across the graphene strip and the lock-in amplifier was connected to an LT-GaAs detection probe. To ensure the DC bias did not affect the detector switch, the PGL connecting from the graphene to the detection switch was

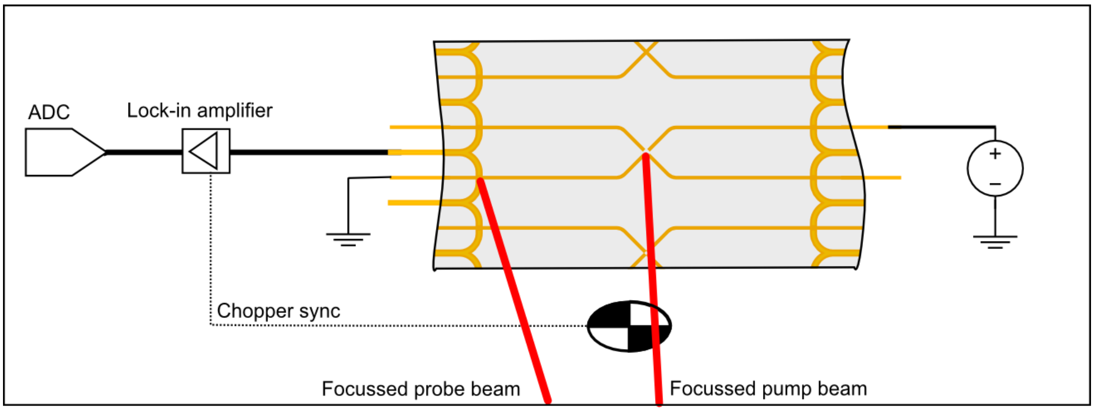

Figure 5.9: Configuration of experimental apparatus used to measure a pulse generated by graphene. The LTA switch is connected to the lock-in amplifier and the bias is applied across the graphene sheet.

always connected to ground. Other than the connections to the electrical apparatus, the devices used for the measurements remain the same as the previous section, with no further modifications required.

5.3.2 Results and discussion

The application of LT-GaAs as a photoconductive material for emission and detection is useful since it would allow complete on-chip terahertz devices to be fabricated without extra semiconducting materials. In Section 5.2 the photoconductive properties of graphene as a detector were presented as the key method of detection. These principles are reinforced in this section which discusses graphene as a generation mechanism for pulses. It is found that although pulse generation is possible, the comparatively low “dark” resistance of the graphene (4 kΩ) creates very large DC currents that produce much more shot noise in comparison to LT-GaAs. For the measurement apparatus used, this restricted the maximum applicable voltage to 0.4 V and therefore limited the resulting detected signal. Very conservative bias voltages were chosen as to not damage the device under room temperature operation. It was found that currents less than 100 μA did not cause resistance fluctuations, were proven to be very stable, and demonstrated effective pulse generation.

Terahertz pulses generated by graphene and detected by LT-GaAs as a function of DC bias voltage are shown in Figure 5.10 (a). The amplitude was found to scale linearly with bias voltage, while the FWHM was 3 ps, with no DC offset observed. The oscillations with period of 4.5 ps are still present. Another important feature of the results is that a small positive pulse is observed at zero bias, plotted in Figure 5.10 (b), and is summed with both the positive and negative biased pulses. In the case of pulse

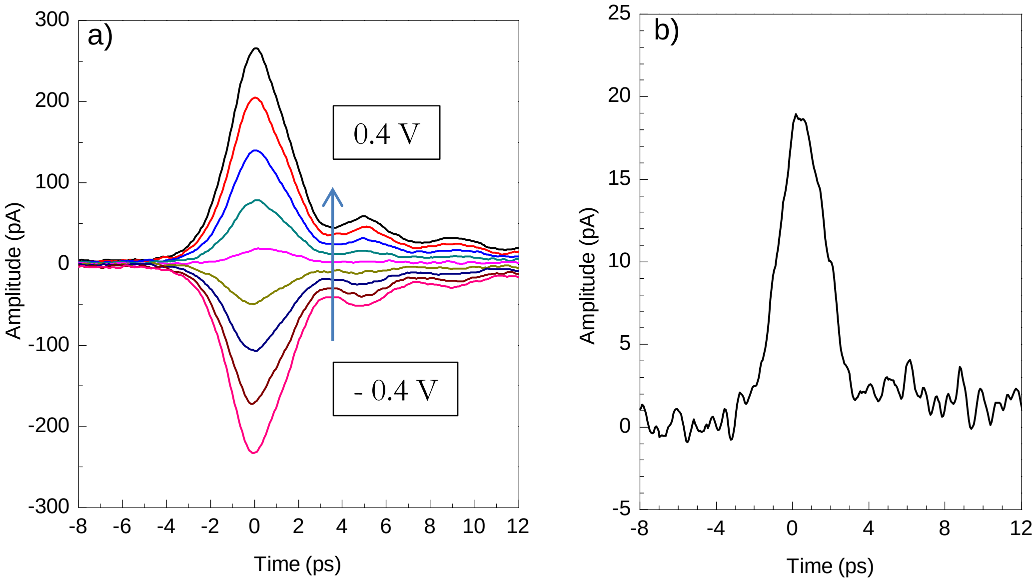

Figure 5.10: Time-domain plot of the pulse generated at the graphene switch GO1 and detected at LTA. (a) Pulses generated by graphene with a bias from -0.4 V to 0.4 V with an increment of 0.1 V. (b) The pulse shape generated by graphene when the voltage source is replaced with a shunt to ground.

generation with LT-GaAs, this behaviour is also present but is caused by the photo-Dember effect where the excited electrons have a faster mobility than the holes,[141,142] which creates a resultant electrical field under pulsed excitation. However, the band

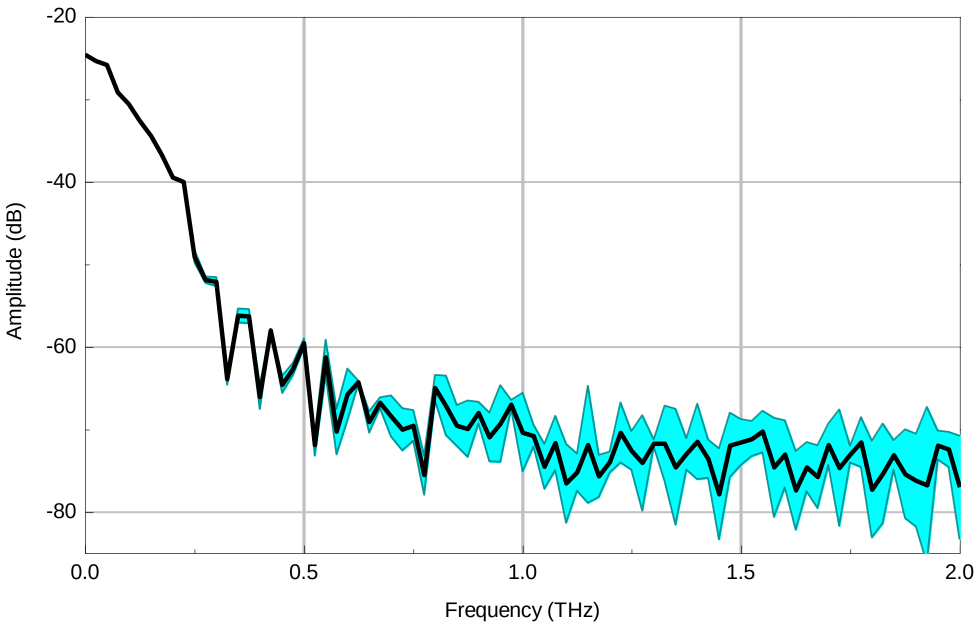

Figure 5.11: Fast Fourier transform of pulses generated by graphene with a bias of 0.3V and detected by LT-GaAs. The black line is the average of three scans and the surrounding blue region is the standard deviation.

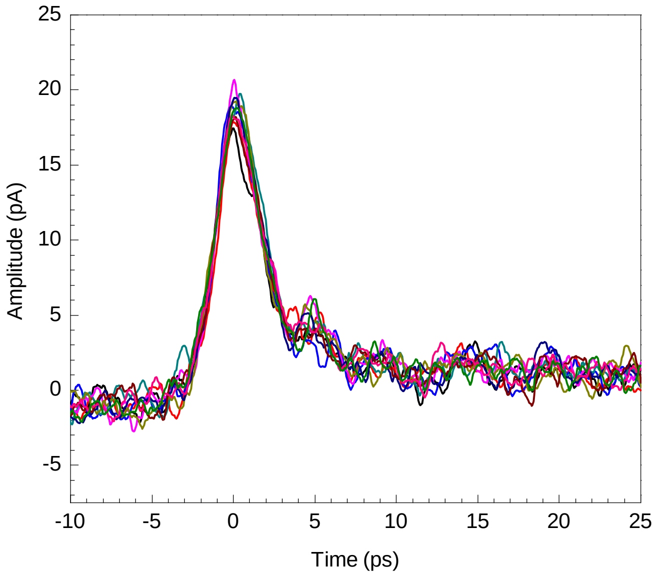

Figure 5.12: Plot of generated pulse as the beam polarisation is incremented from 0-180 $^{\mathrm{O}}$ in increments of 20$^{\mathrm{O}}$ all results recorded using a 0.4 V bias.

structure of pristine graphene means that the effective mass of electrons and holes is equal, so the photo-Dember effect is not valid. Photoexcited pulse generation was, however, reported by Prechtel *et al* for freely suspended graphene and was attributed the photo-thermoelectric effect and the built-in electric fields that are created when gradients in carrier concentration are present.[40]

It was found that a Lorentzian fit of this zero-bias pulse generated by graphene across all the devices tested can have a FWHM as large as 3.9 ps, but it can also be as low as 2 ps. The data plotted in Figure 5.10 has a FWHM of 3.2 ps for all biased pulses, but a value of 2.9 ps when no bias is applied. As the FWHM has a direct effect on the bandwidth of the pulse, this indicates a similar bandwidth for biased graphene generation as for that of graphene pulse detection. A longer time window around the pulse was measured to obtain an increased FFT resolution, and is displayed in Figure 5.11. The lower frequencies showed low noise levels up to 300 GHz, but the signal did not drop below the noise floor until 500 GHz. The FFT of other pulses from graphene using different geometries are consistent with this in terms of bandwidth (within a range of ±100 GHz) even though the signal amplitude can be up to an order of magnitude smaller.

The effects of polarisation on the pump beam were recorded over a range of polarisations (Figure 5.12) in order to check if the mechanisms were in any way different to that of the generation scheme. No difference was observed in the peak amplitude or offset. It should be noted that the low signal levels produced in the graphene generation technique meant

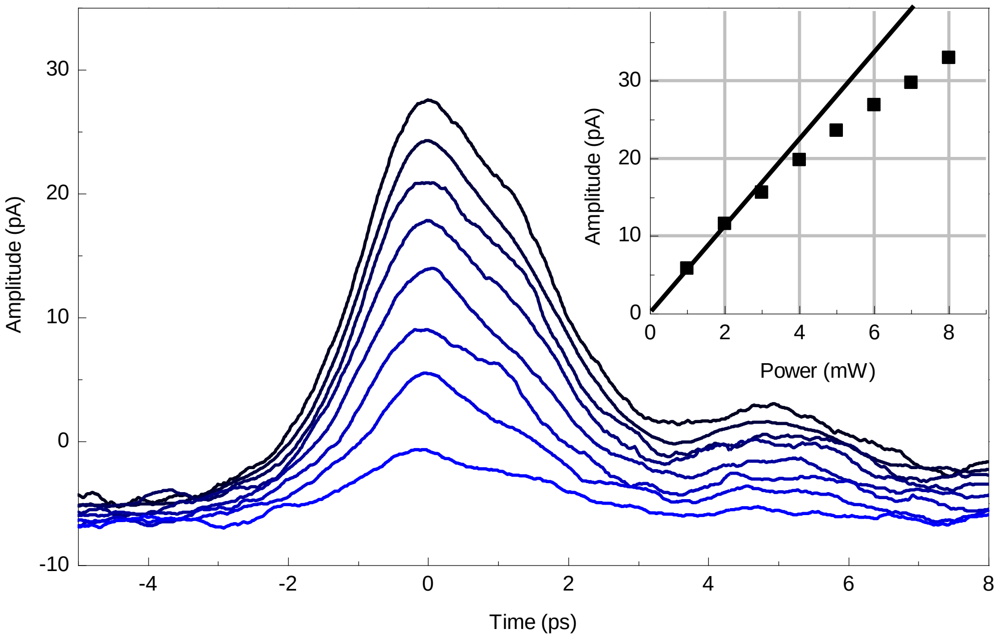

Figure 5.13: Pulses generated by graphene and detected by LT-GaAs over the range of powers from 1 – 8 mW in increments of 1 mW for a bias of 0.4 V. The inset shows the maximum amplitude of a Lorentz-fitting in squares with a solid line as a guide to the eye to the region of linearity.

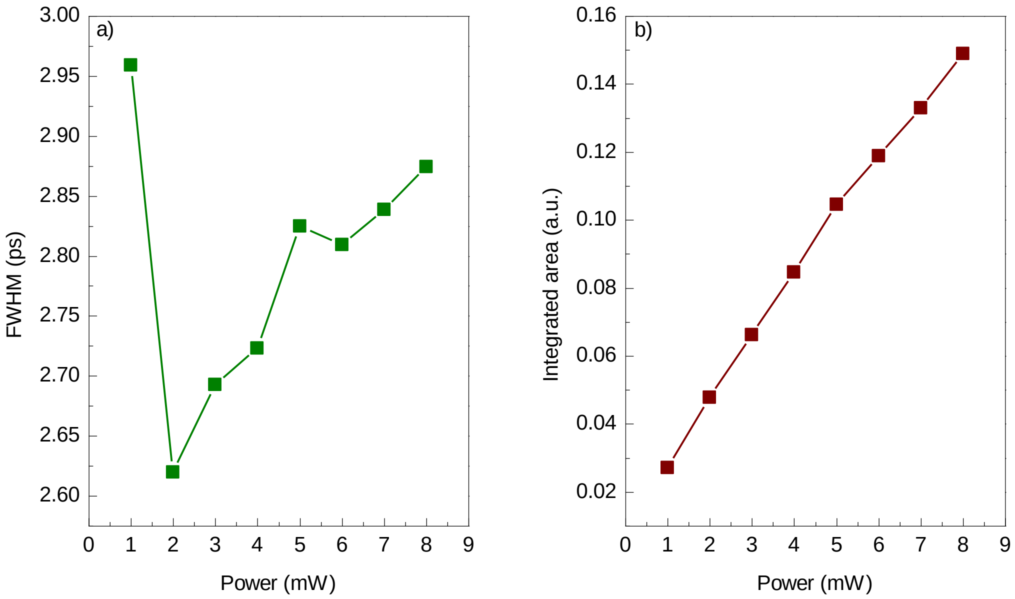

Figure 5.14: FWHM (a) and integrated area (b) of the fitted curves as a function of power for 0.4 V and 10 mW laser power at the LT-GaAs detection switch.

that OC-THz-TDS scans are much noisier for comparable scan time constants and velocities using the graphene detection methods.

When investigating graphene detection in the previous section, a non-linear variance with power was found. In graphene generation, a similar response was found and the results are shown in Figure 5.13. Parameter fitting to each of the pulses, generated at varying powers, indicated that the total time-integrated charge of the pulses scale almost linearly, as shown in Figure 5.14 (b). These results show that as the power is increased, the total number of hot-carriers that are generated also scale linearly, but the increased carriers in the conduction band slows the cooling rate. In a practical sense, this may limit the potential of graphene at much high powers, when using the same conditions of this experimental setup. However, the initial doping level of the graphene in these measurements is also relatively high, and it is possible that devices with lower carrier concentrations may demonstrate much better performance at higher powers.

5.4 All-graphene THz generation and detection devices

The picosecond pulse generation and detection in graphene so far in this chapter was demonstrated in conjunction with LT-GaAs due to its excellent signal to noise properties, and so that it could be used as a benchmark for comparison of results. However, if graphene is to be used as a replacement of GaAs in high bandwidth electronic devices, demonstration of simultaneous pulse generation and detection graphene must be shown on the same device. This section reports the first step to achieving this goal, and in

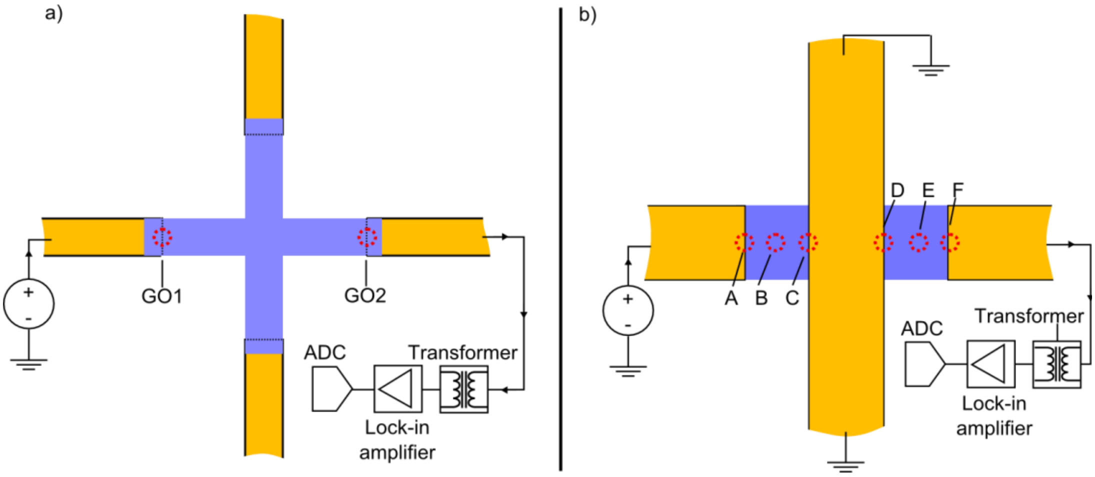

Figure 5.15: Experimental device configuration for measurement of pulse generation and detection using graphene. (a) Device D3. Generation and detection at opposite ends of a 50um graphene strip, where the circles at GO1 (GO2) represent laser alignment for generation (detection) beams. Au contacts and graphene are 9 µm wide, the distance from GO1 to GO2 is 50 µm. (b) Device D5. A conventional "input" pulse configuration with 6 potential illumination locations (A to F). The width of Au and graphene is 30 µm, while the separation from A to C was 40 µm.

particular discusses the autocorrelation of ultrafast laser signals in two graphene devices, one in the cross-geometry device discussed already, with the other being a pair of switches joined by a 30-µm-wide PGL.

5.4.1 Experimental setup

In order to measure pulses using all graphene on-chip systems, two separate experimental systems were setup as shown in Figure 5.15. Each system was used in two configurations, the first being for measuring autocorrelation of the graphene's carrier dynamics, where both beams were aligned to GO2 on device D3 (Figure 5.15 (a)), or position F on device D5 (Figure 5.15 (b)). Both the pump and probe beams were chopped so that they could be aligned to the location of maximum photocurrent, a bias was applied for a source-meter and the grounds on the centre contact of D5 had to be disconnected. A transformer was required in each measurement to allow high current DC bias without overloading the input of the lock-in amplifier. The second configuration was designed to try and detect an "input" pulse by creating spatial separation between the generation and detection beams. This allowed the pulse to propagate a small distance through graphene

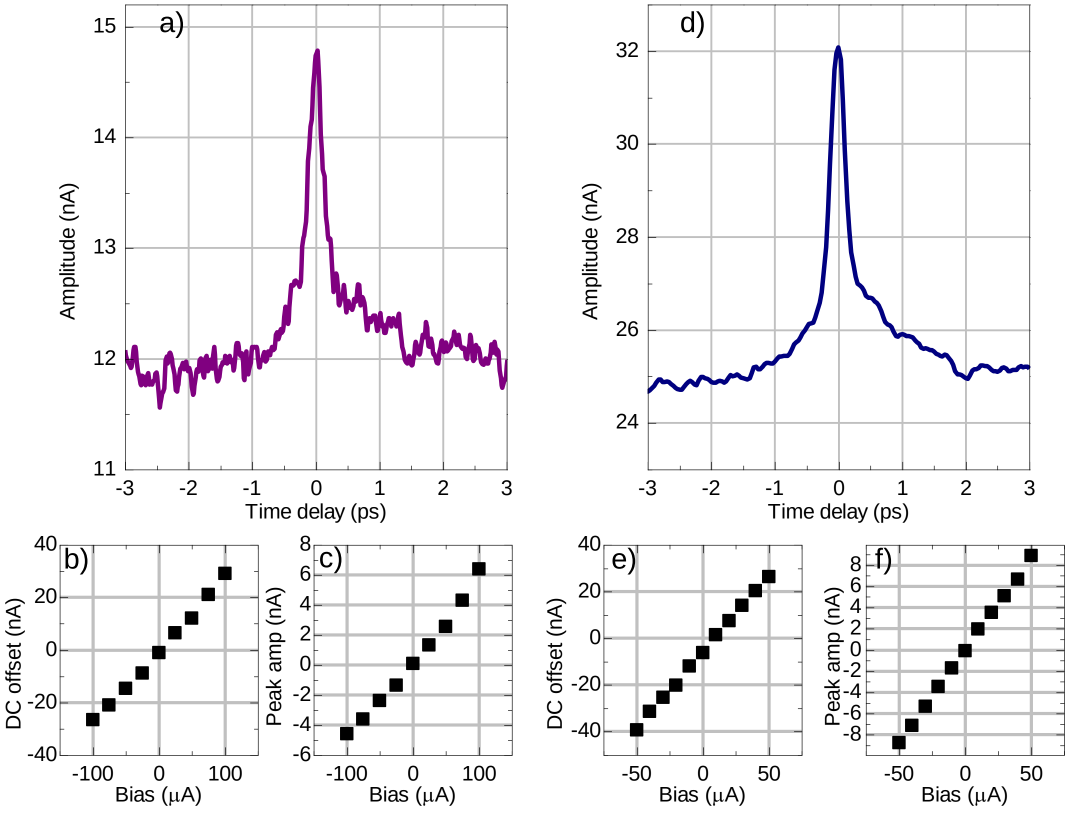

Figure 5.16: Autocorrelation measurements of graphene on two geometries using a 110 fs FWHM laser pulse. (a) Correlation measurement for GO2 on the X-shape geometry for a 50 µA bias. (b) and (c) are the DC offset and amplitude of the peak as a function of bias. (d), (e) and (f) are the same measurements repeated at position F on the rectangular geometry.

or metal before being detected. For device D3 this required the pump beam at GO1 and the probe beam at GO2. In device D5 the generation switch configuration was tested at A, B and C, and the detection switch location was aligned to D, E or F. The locations A to F are each defined by the photocurrent generated at that location, where A, C, D and F are positions of maximum DC magnitude. The locations B and E are positions of zero DC offset current.

5.4.2 Results and discussion

In order to measure the carrier dynamics of the graphene and verify the THz-TDS system was operating correctly, the intrinsic response time was measured for each of the experimental devices using the autocorrelation techniques described in Section 2.2.3.1. Each device was measured for a range of bias currents, where the full scans at 50 μA are plotted in Figure 5.16 (a) and (d). Furthermore, the amplitude and offset values for each bias current is shown in Figure 5.16 (b), (c), (e) and (f) are also plotted to show the dependence of autocorrelation scales linearly with applied current. The DC offset signal is also observed to scale linearly but a non-zero intercept at zero bias current is also apparent. This corresponds to the photo-thermoelectric current generated at the graphene/metal interface producing a bias current of its own. The non-locked-in DC signal was also measured to evaluate to total level of optical modulation that is applied. As graphene is a gapless semiconductor and, in these devices, had a DC resistance of ~750 Ω/□, the on/off ratios were not expected to be very high. The modulation caused by the optically chopped signal was found to be less than ~0.1 % of the biased DC signal, using a combined illumination power of ~20 mW. The FWHM of the peaks are ~350 fs and the shape is caused by saturation of carrier generation and occurs when the first pulse pumps the carriers out of their relaxed state and the second pulse arrives before all the carriers in that area have fallen back into equilibrium. In ideal experimental conditions, the peak is symmetrical as both pulses hit exactly the same spot with the same power and at the same angle. However, these measurements were taken with two beams that each pass through a different set of optics, each therefore hitting the graphene at slightly different angles and, hence, asymmetrical features are seen at ±200 fs. Therefore, exact values of carrier lifetime for graphene in this configuration cannot be precisely determined, but an estimate of the time where most carriers return to a relaxed state lies between 1 – 2 ps.

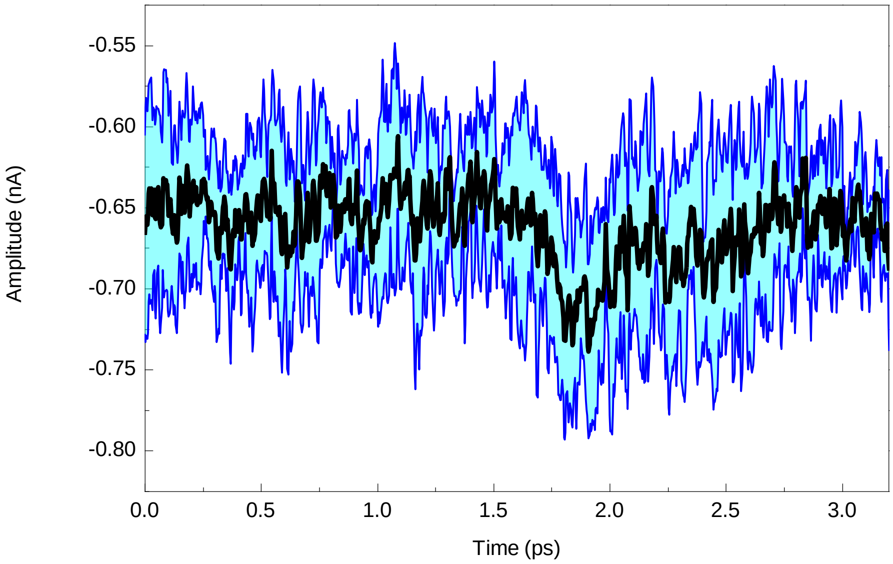

Figure 5.17: Scan of low amplitude signal detected at position D and generated at position A using a -200 μA bias. The black line is the average of 5 scans and the surrounding blue region is the standard deviation.

Although correlation measurements of the graphene were useful to understand the carrier dynamics, they were also used to calibrate the scan window to try to observe if simultaneous pulse generation and detection was possible. In device D3, bias currents up to ±250 μA were used. The photo-modulation of these resulted in locked-in currents of ±34 nA, although no clear pulses was seen, even when using a large number of averages and long lock-in time constants were used. Device D5 allowed a greater level of flexibility in terms of the range of measurements that were possible, and every combination of generation position (A, B and C) with detection position (D, E and F) was attempted using a range of bias currents up to 2 mA, where the best signal obtained is plotted in Figure 5.17. Although small features were noticed at the expected positions after 5 or more averages, these were very small in relation to the noise of the measurement and it was determined that these could simply be caused by weak correlation of the beam across the centre conductor.

A possible method for increasing the dark resistance of the graphene, and potentially improving the measurement sensitivity, is to partially damage it, so that sheet resistance is increased. This was attempted with device D5 by placing it in an oxygen plasma asher for 1 minute at 50 W, but this proved to be too long and damaged the graphene so that it would not conduct at all.

5.5 Conclusion

The application of graphene as a terahertz photoconductive detector has been demonstrated in this chapter at operating frequencies up to 600 GHz. The results were obtained by using a standard system for measuring LT-GaAs on-chip THz devices with no special modifications required other than the graphene switches under test. The DC photocurrent mechanism was attributed the photo-thermoelectric effect and was used as the primary method for aligning the beam to known locations on the device. The photoconductive mechanism was discussed and comparisons of frequency response, pulse profile and amplitude with respect to LT-GaAs were given. The possibility of residual LT-GaAs in the region was also ruled out through Raman spectroscopy, with further evidence to be presented in the next chapter.

The operation of graphene as a photoconductive emitter was also presented where pulses were generated under applied voltage biases of ±0.4 V. The pulses were detected by LT-GaAs and also produced a small pulse with no applied voltage due to the photo-thermoelectric effect and built-in fields at the junction. Similar pulse generation in graphene has been reported in the literature under zero applied bias,[40] but the addition of bias voltages here has significantly improved the amplitude of the signals that can be measured.

Pulse detection and generation using only graphene was also attempted. The pico-amp pulse generation, low photoconductivity modulation of graphene and high dark current all made the recovery of the signal difficult, even with high sensitivity lock-in techniques and filters. Nonetheless, the results on autocorrelation of signals contained in this chapter indicate that the concept should be possible and further independent investigations for optimising pulse generation and detection respectively, could pave the way for complete OC-THz-TDS systems that do not require III-V semiconductors.

These results show much promise for graphene's future in high-speed and THz electronic applications, especially due to the relatively low cost and less demanding fabrication techniques in comparison to LT-GaAs. However, the understanding and performance of graphene THz photoconductive devices require improvements before they can be widely used. One possibility for future work would be to investigate graphene-based pulse generation as a function of carrier concentration. This, however, could be rather difficult, owing to the screening effects that would be introduced by the proximity of conductive gating material such as Si or ionic gels, typically used to achieve different concentrations.

Chapter 6: Spatially resolved pulse detection using graphene

6.1 Introduction

The on-chip graphene pulse detection methods discussed in the previous chapter focussed on a single detection position, where the probe beam generated the largest negative photocurrent across the graphene. This was done to allow accurate and repeatable alignment and, hence, a direct comparison of the results was used to build an understanding of the mechanisms at work.

In this chapter, the properties of few-picosecond pulses detected by graphene are presented as a function of probe beam position. It is expected that by spatially resolving the pulses across the detection region by scanning the NIR probe beam position, would provide information on how the graphene interacts with the terahertz (THz) electromagnetic radiation over sub-mm distances. In addition, these measurements may also determine which components of the switch design influence the pulse detection properties, allowing for more efficient designs in the future. One- and two-dimensional scanning was used with three different device geometries. The first, a rectangular 50 μm × 9 μm switch, showed enhanced detection properties immediately after the graphene/metal interface, and displayed dispersion across the short propagation distance. The second and third devices terminated the planar Goubau line (PGL) in the radial centre of a semicircle (100 μm and 200 μm respectively) in order to explore the pulse dynamics without the influence of an opposing PGL contact.

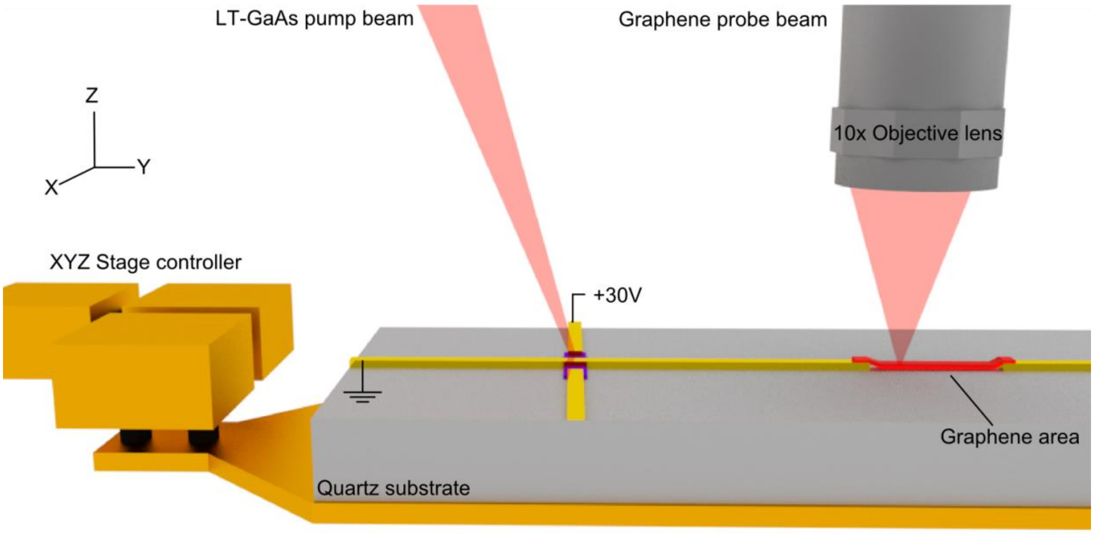

Figure 6.1: Schematic of the experimental setup used for mapping pulses detected by graphene that were generated by an LT-GaAs switch. The 60-μm-long and 9-μm-wide graphene strip overlaps the Au by 5 μm at each side of the 50-μm-long PGL gap.

6.2 Linear results

6.2.1 Experimental setup

The work presented in this section was conducted to determine the linear properties of pulse detection across graphene. Provisional measurements were taken using the setup discussed in Chapter 5 by scanning the probe alignment mirror along the graphene strip area. Although variations in pulse properties were found, there was no way to accurately determine the absolute position of the beam on the graphene area, thus how this related to the geometry of the device. To achieve this, the experimental configuration shown in Figure 6.1 was used instead, in which the device D4 (design SG-50) was directly mounted to a computer-controlled 3-axis linear translation stage with a 10 mm range in each dimension and a resolution of 125 nm. The 10x NIR objective lens was aligned to be parallel with the Z direction and focus of the optical probe beam to the graphene/metal interface was conducted manually using joystick control. All further measurements were conducted by measuring a THz scan and then incrementally stepping the motion in the Y-direction.

The stage was capable of computer control using proprietary software. However, this was unnecessary as the pump beam had to be aligned to the LT-GaAs switch for every measurement. Therefore, all measurements were recorded and positioned independently which placed a practical limitation on the resolution that could be achieved. It was found that the stages used for X and Y control were not calibrated precisely, and required correction factors to scale the position readout to the features on the device. Drift of the stage over time was determined not to be an issue as the stage was cycled multiple times between the two graphene/metal interfaces, at which the current was most positive and most negative; the signal measured at each of these positions remained constant, indicating negligible stage drift over time.

6.2.2 Measurement techniques

Each of the measurements of this setup used an LT-GaAs excitation switch with a pump beam of 10 mW, 24 μm spot size, and a DC bias voltage of +30 V. The graphene probe beam was chopped at 2.8 kHz, and a 1 mW average optical power was focussed into a spot size of 5.5 μm (determined by knife-edge measurements). To record the spatial variation of the OC-THz-TDS measurements, the stage/device was moved in the Y direction relative to the graphene probe beam. For each stage position the pump beam had to be manually aligned to the LT-GaAs, and the photocurrent measured by the Keithley source meter was thus the same for each measurement.

6.2.3 Results and analysis

Each of the time-domain scans recorded the DC offset, generated by the photo-thermoelectric effect, [9] and the AC signal, that contains the THz information. The data collected for a straight line traversed between the nearest graphene/metal interface (0 μm) and the furthest (50 μm) is shown in Figure 6.2 (a). To calibrate the stage, the known positions of the two graphene/metal interfaces were used as a reference. A DC photo-thermoelectric current, measured by a lock-in amplifier, was generated when the beam was aligned to each of the interfaces, and was found to be negligible elsewhere. The change in Y position the graphene/metal interfaces was known to be 50 μm, and the software readout indicated a distance of 104 μm. Therefore, a scaling factor of 0.48 was applied to all subsequent measurements. In addition to accounting for errors in the calibration, this value also accounts for any scaling caused if the sample was not mounted exactly plane-parallel to the movement of the stage. However, for these measurements this contribution was considered to be negligible, since the alignment angle of the beam from 90° to 80° relative to the sample could only contribute a ~2 % change in the position readout, which would be difficult to resolve in the measurements.

The DC component, relative to the generation switch, was positive for the closer graphene/metal contact and negative at the further contact. If the interface is considered to be a point like photocurrent source, the profile of the peaks would be expected to be Gaussian with a FWHM of 5.5 μm due to the profile of the illuminating beam. The fitted Gaussian FWHM for the peaks at 0 μm and 50 μm are calculated to be 4.4 ± 0.2 μm and 7.2 ± 0.3 μm respectively. The variation of these values is expected to be from a combination of factors including the spatial resolution of the scan (2.6 μm), beam diffusion within the ~1 μm thick S1813 and reflections from the back of the substrate.

To plot the parameters in Figure 6.2, a Lorentzian peak fitting algorithm was performed on the data obtained at each location. The pulse shape, shown in Figure 6.3 (a), has oscillations immediately after the peak that did not fit the Lorentzian function and, hence, only the range from −17 ps to 4 ps was used.

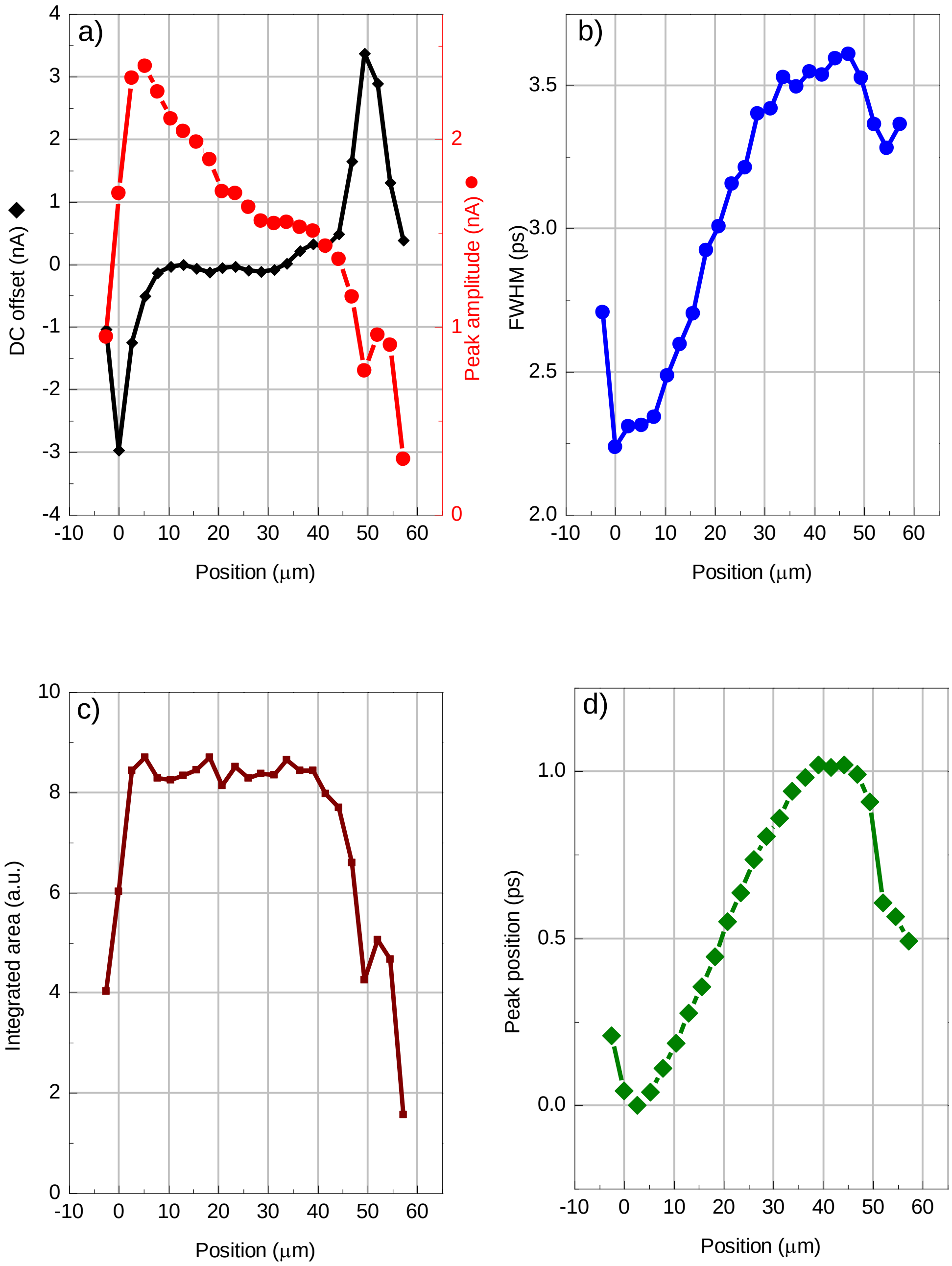

Figure 6.2: The Lorentzian fitting parameters used to model each detected pulse across the 60-μm-long graphene region. The spatial resolution of the measurements was 2.6 μm. The plotted parameters include DC offset and peak pulse amplitude (a), FWHM (b), the area of each pulse (c), and the relative arrival time the peak amplitude (d).

A comparison of the DC offset alongside the pulse amplitude is shown in Figure 6.2 (a) where the AC peak pulse amplitude did not occur precisely at the metal interface, but instead ~5.2 μm away. At this beam position, the full energy of the laser was focussed onto the graphene which is located immediately next to the metal contact. The larger amplitude is because the conductivity of the illuminated graphene above the gold contact is insignificant in comparison to the high conductivity of the gold. Therefore, it does not alter the total current through the system under illumination. This means that almost the entire contribution of the AC signal is a detected by the graphene above the quartz substrate.

The higher pulse amplitude observed 5.2 μm from the interface is also expected to be caused by the contrast of strong THz field confinement at the metal edges, and the lower confinement towards the centre of the graphene sheet. This is because the current flow is not only dependent on the conductivity of the graphene, but also on the electric field across the illuminated graphene region. To illustrate the enhancement of pulse amplitude close to metal features, time-domain pulses measured at locations 0 μm and 5.2 μm, with the DC component removed, are shown in Figure 6.3 (a). The lower amplitude pulse was detected at the nearest graphene/metal interface and the other is the location of maximum pulse amplitude. This measurement was repeated using a larger spot size of 24 μm, shown in Figure 6.3 (b). In each case, an increase in pulse amplitude was seen by moving the probe laser from the interface to the inner edge of the contact, increasing by

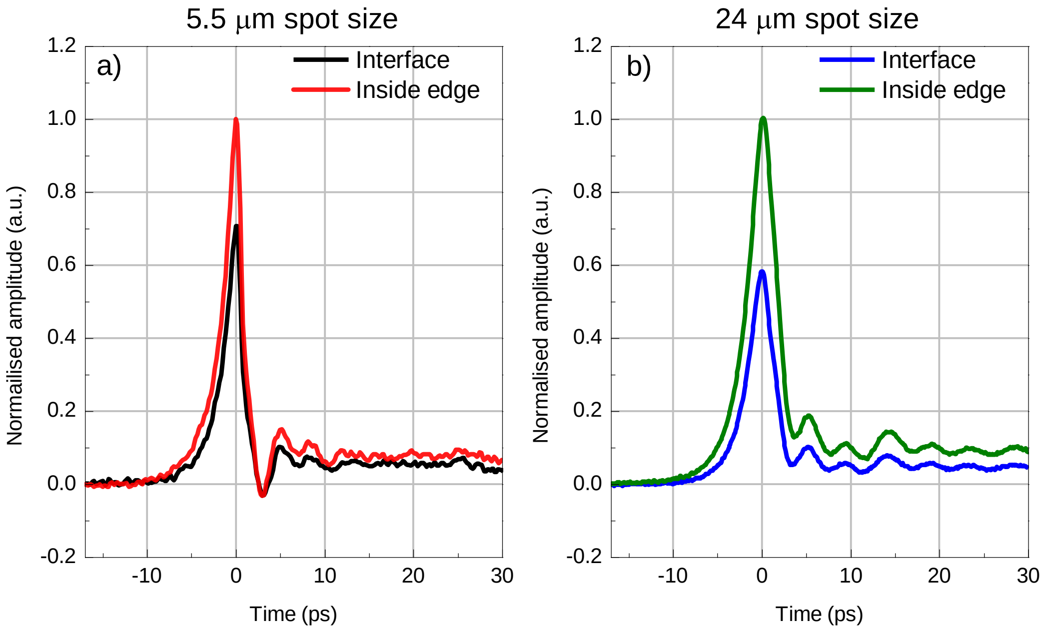

Figure 6.3: A comparison of pulses detected at the interface and inside edge of the nearest graphene/metal interface, with DC offsets removed. (a) 5.5 μm laser spot size (1mW power). The black line was measured at the interface and the red line is measured 5.2 μm away, towards the centre of the graphene. (b) 24 μm laser spot size (10 mW power). The blue trace was measured at the graphene/ metal interface and the green trace is measured towards the centre of the graphene. No measurement stage was used so the pulse was aligned to the maximum pulse amplitude.

~40 % when using the smaller spot and by ~65 % when using the larger spot. The enhanced effect on the larger spot can be explained by considering the change in magnitude of the field across the spot size, where a larger spot size leads to a large change in field.

The peak amplitude of the pulse gradually decreases across the length of the graphene channel. Upon first inspection this was thought to be caused by the total field strength decreasing as the detection location moved further away from the metal edge. However, in addition to pulse amplitude, the shape of the pulse also changed as a function of position. This indicated that although the peak field strength changed, the time-averaged field strength may not.

The FWHM and integrated area of the pulse are shown in Figure 6.2 (b) and (c) respectively. In a large region between the metal contacts, as the pulse amplitude decreases, the FWHM increases proportionally so that the total charge of the pulse remains the same. This is expected to be because the two metal PGL contacts act as a parallel plate capacitor, where the field lines across the switch are parallel. This would cause a frequency dependent phase change to be induced along the gap, causing a broadening of the FWHM. However, this explanation does not take into account that the pulse may be coupled to the graphene. In this case, confinement to the graphene would cause strong resonances (Fabry-Pérot) at the interfaces unless the characteristic impedance of the graphene and metal PGL were exactly the same. The only oscillation that is observed is that of probe arm at 220 GHz, as discussed in Section 4.3. It should be noted that the characteristic impedance for each material in this PGL configuration cannot be calculated (as discussed in Section 2.3), it is highly unlikely they would be similar due to the drastic differences between the Au and graphene properties. The FWHM data that occurs before 0 μm and after 50 μm are seen to deviate from the trend of the other fitted data. This is, in part, is owing to the small signal-to-noise ratio at the edge (~18 dB) compared to the centre of the graphene (~48 dB), affecting the convergence of the resultant fit, although the offset and pulse amplitude are still very close to that of the original pulses.

A further method to determine whether the graphene was acting like a transmission line is to calculate the pulse propagation velocity by measuring the arrival time at each location. If the pulse propagates along the graphene with a slower velocity than that of free space propagation, an approximate value of the modified relative permittivity, ϵ_r, can be calculated. The peak position, as measured across the length of the strip, is shown in Figure 6.2 (d). The pulse travels ~33 μm in a time of 1 ps, corresponding to a velocity of 33 × 10^6 m s^{-1}. It is expected this value may vary slightly from errors caused by the relatively small propagation distance and the realignment of the pump beam for each measurement. The angle of the pump beam to the surface of the device was ~30° from the surface and corresponded to a laser path reduction of 25 μm over a 50 μm movement range. In terms of an optical pulse travelling in free space, this accounts for a time difference of −83 fs from the reported value for the far contact in Figure 6.2 (d) and would only slightly raise the pulse velocity to 36 × 10^6 m s^{-1}. If the graphene was acting as a transmission line, this would represent an effective permittivity of 70 (using equation 2-4) which is significantly higher than the values reported in literature, indicating that it is unlikely to be acting as a transmission line.

6.3 Semi-circle device results

To understand the pulse propagation dynamics near graphene with an alternative switch configuration, the device shown in Figure 6.4 (a) was fabricated. The geometry of the device consisted of a single pair of LT-GaAs switches that generate a pulse into a 500-μm-long PGL, where it is terminated at the radial centre of a graphene semi-circle. The circumference edge of the graphene is contacted by a gold ground plane. The motivation for looking at this geometry was to enable study of the terahertz field detection in two-dimensional space as the pulse propagates away from the PGL/graphene interface. A

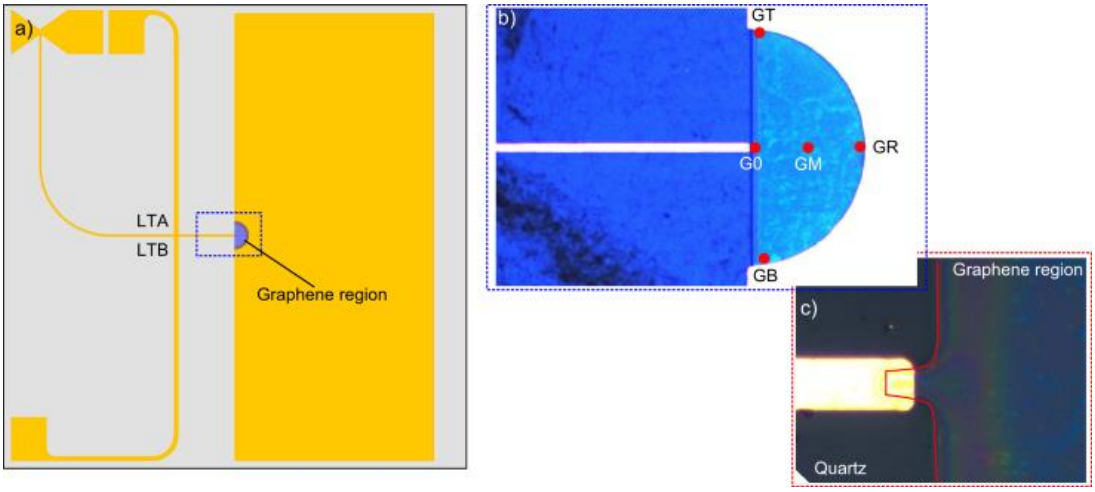

Figure 6.4: The device geometry used for detecting pulses in a semi-circle region of graphene as used for 100 μm and 200 μm (pictured) radius devices. (a) The schematic of the entire device where the edge of the grey box is 4 mm × 4 mm. (b) A micrograph of the fabricated device where the lighter blue region is the graphene/S1813 and the representative switch locations are shown as red spots. The distance from G0 to GR, GT or GB is ~200 μm. (c) A higher magnification of the 9-μm-wide PGL contacting the graphene/S1813 region, with the edge of the S1813 shown in red.

larger semi-circle graphene region was used, rather than a rectangular strip of graphene as discussed in Section 6.2, as this was expected to allow a clearer observation of the terahertz field by making the distance between contacts larger, and imaging the variation with beam as a function of probe position.

Since the devices used in this chapter had only one pair of LT-GaAs switches, rather than two pairs either side of the graphene region, the opportunity was taken to fabricate the graphene switch in an area where no LT-GaAs had been transferred. This differed from previously mentioned devices as each of the graphene regions were fabricated on an area of the device where LT-GaAs had been transferred and etched away. Although Raman spectroscopy of these devices validated no trace of GaAs residue to be found in these etched regions, the semi-circle devices took an extra step to ensure this was correct. This was conducted by etching a single LT-GaAs rail at the edge of the transferred material (<500 μm) and marking the quartz substrate to indicate which side the graphene switch should be fabricated on so that it is clear of the etched LT-GaAs region. The fabrication steps then proceeded as described in Chapter 3 and Section 5.2.1.

6.3.1 Experimental setup

This section presents data collected from two similar devices and using two different OC-THz-TDS systems. The first device used a semi-circle with a 100 μm radius and was tested on the same OC-THz-TDS system, as discussed in Chapter 4. The second device used a 200 μm radius semi-circle, which after characterisation on the original OC-THz-TDS system, was tested using a second system that added the capability of mapping each optical beam via computer control. This system was significantly more versatile for OC-THz-TDS pulse mapping, where the pump and probe beams were coupled to fibre optics that could be independently scanned across the switches of the device.

The mapping system, illustrated in Figure 6.5, used a 70 fs pulsewidth, 80 MHz pulsed Ti:Sapphire laser centred at ~780nm to drive an OC-THz-TDS setup where the pump and probe beam were independently coupled to 10 m long solid core silica optical fibres. The ends of each fibre were mounted in fibre ferrules which were connected to a set of piezoelectric translation stages, enabling independent control of the position of each optical beam. Both beams were focussed onto the device using a single optical lens. The advantage of the mapping system is that the translation stages had been configured to work with the THz-TDS software and had the ability to programmatically map THz pulses in across a designated region. The piezoelectric control system was open-loop and was controlled by an "attocube" motion controller and interfaced to a computer via GBIP connection. Other than the XY control of the pump and probe beam, the only

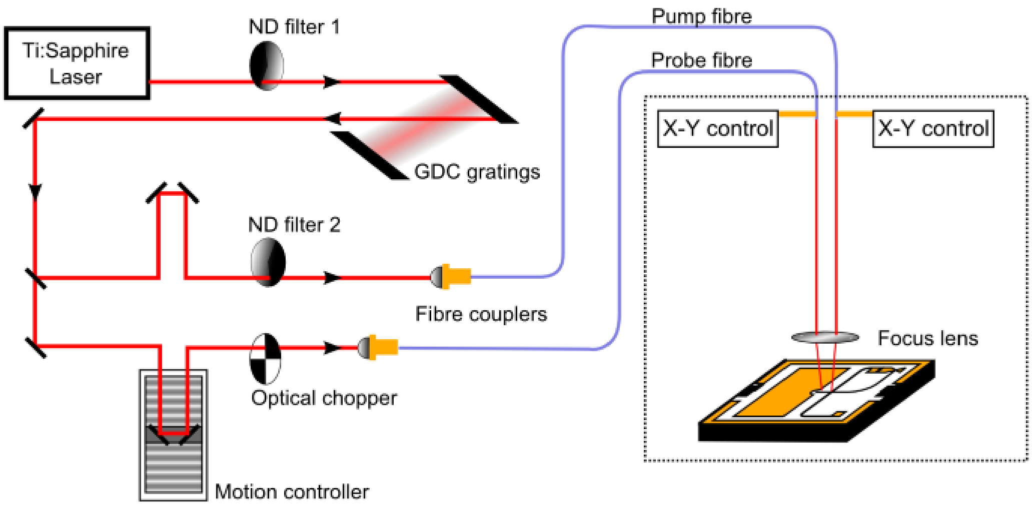

Figure 6.5: Experimental schematic of the mapping OC-THz-TDS system. The grating dispersion compensator (GDC) was used to negatively chirp the pulse to balance the dispersion from the fibre optic waveguides.

functional difference in the path of this system over the previous system is the fibre optics and the grating dispersion compensator (GDC), which resulted in a 130 fs pulse width at the device. The GDC gratings were found to be power sensitive and caused expansion and contraction oscillations when a combined laser power larger than 7 mW was used. This caused a time varying alignment to all subsequent optical components and so the powers of the beams were limited to 3.5 mW each.

6.3.2 Measurement techniques

For the measurements that required mapping of THz pulse detection using graphene, only the probe beam was scanned under automatic operation and the pump beam remained fixed on the LT-GaAs. The scanning XY stages required calibration as the open-loop operation meant that position feedback was not possible. Piezoelectric motion stages do not move by equal magnitudes in forward (positive voltage) and backward (negative voltage) motion. Therefore, a correction factor was calculated independently for positive and negative voltages in X and Y to ensure that the beam would return to its starting position before the next line was scanned. This was done by scanning the known features of LT-GaAs and incrementally changing the correction factor to reduce skewing of the photocurrent image. Some of the results still display slight skewing as it was not practical to calibrate the correction factor every time the resolution was changed.

6.3.3 Results and analysis

The geometry of the semi-circle device consisted of some key changes to the previously discussed devices in this work. In order to measure the device in the fibre optic system, the device was required to fit in a 5 mm × 5 mm recess of a ceramic chip package. This meant that parasitic regions were much shorter, decreasing the intrinsic resolution of the device in the frequency-domain determined by reflections from bonding pads. On the other hand, an advantage of this design over the previous geometry is that the probe arm geometry was modified so that Fabry-Pérot oscillations were not produced, and allowed a more sensitive detection of resonances or reflections. The "input" pulse and the pulse detected by graphene are shown in Figure 6.6. As this device only had one pair of LT-GaAs switches, the pulse velocity measurement technique discussed in Section 3.2.5 could not be used. An approximation of the velocity can be made from the "input" pulse reflection at the PGL/graphene interface, located 500 μm away, which arrived ~6 ps later. This corresponded to a velocity of 1.66×10^8 m s^{-1} which was consistent with previous measurements using the same 9-μm-wide PGL geometry.

As the power of the scanning system was limited to 3.5 mW per beam, each device was first evaluated in the non-scanning OC-THz-TDS system using 2 mW pump and probe beams. The characteristics of each device varied and allowed different measurements to be performed on each device. The 200 μm device performed optimally at lower powers due to better LT-GaAs switch properties. This meant that lower time constants could be used and scan times were lower, factors that were very important when recording thousands of different detection locations. The 100 μm device produced very weak

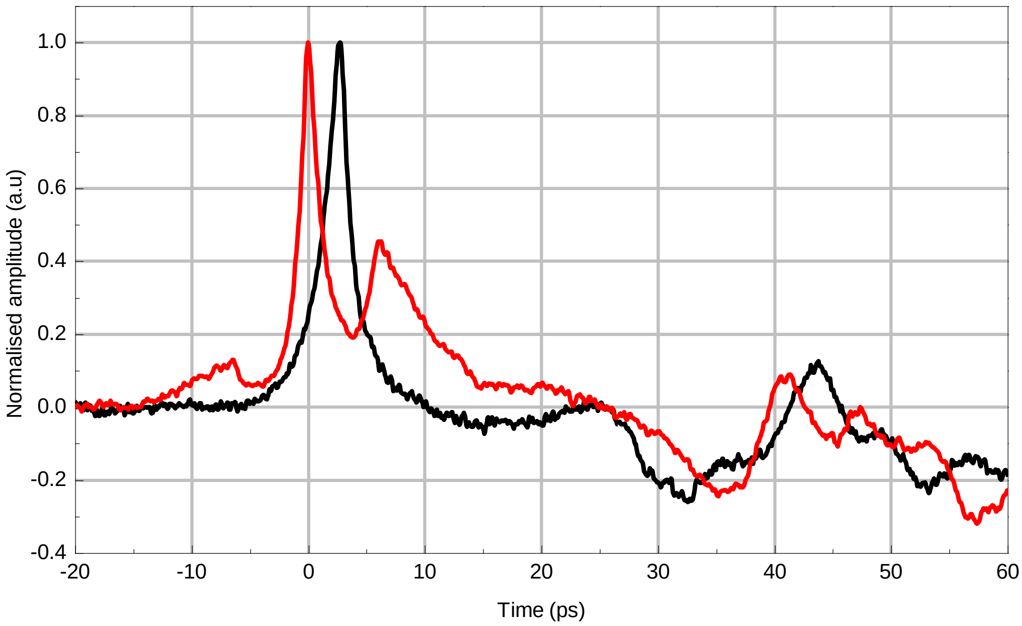

Figure 6.6: Pulses generated by LT-GaAs and detected at the "input" (red) and by the graphene switch at G0 (black). The features after 25 ps originate from the bond pads of the device.

pulses at 2 mW powers. At higher powers, however, the smaller graphene region allowed good graphene pulse detection properties across the entire sheet.

Pulses detected by graphene using the 100 μm device were measured at key locations across the graphene sheet, as shown in Figure 6.4. The pulses detected at five points of the 100 μm radius graphene semi-circle on the are shown in Figure 6.7, where the inset of each pulse scan shows the approximate detection location indicated by a red spot. Each position was located by moving horizontally or vertically away from position G0. The top (GT), bottom (GB) and right (GR) locations were determined by aligning to the most positive DC photocurrents found at the metal interface, and the middle location (GM) was determined to be approximately half way between G0 and GR.

Each of the main pulses differed by amplitude, offset and arrival time of the detected pulse. The Lorentzian peak fit parameters for each pulse is given in Table 6.1, where the fit was performed for the values from -8 ps to 2 ps.

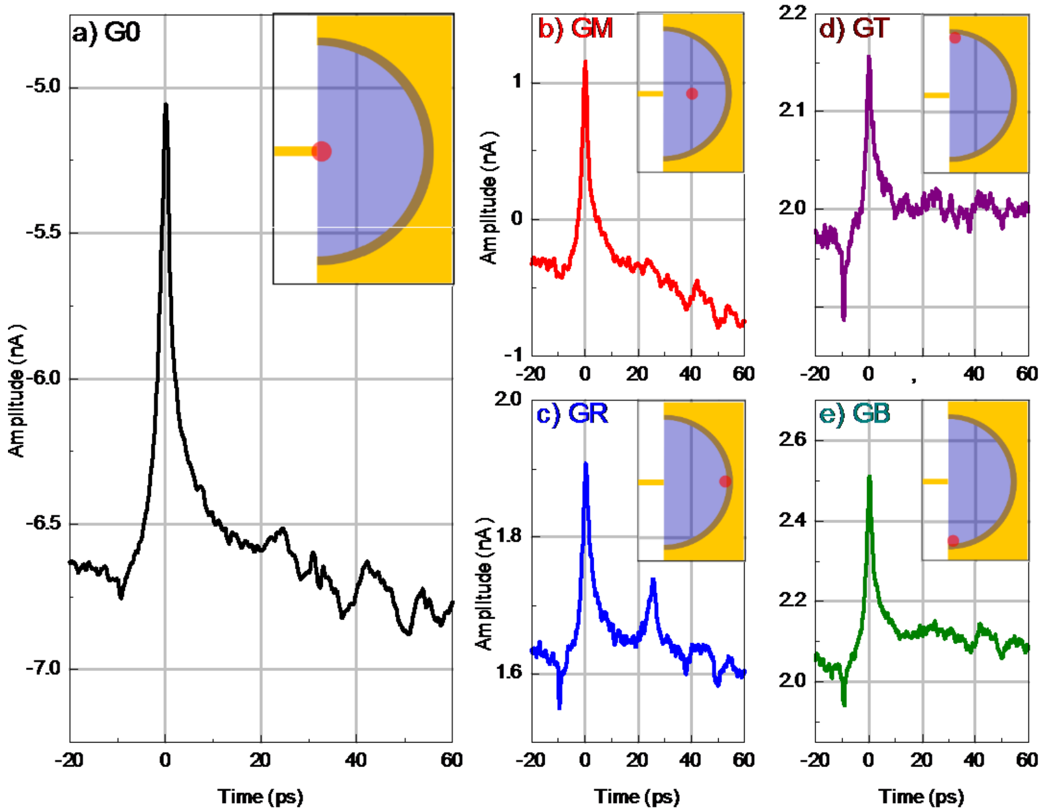

Figure 6.7: Pulses generated by LT-GaAs and detected at 5 locations on a graphene semi-circle geometry switch. Each time-domain plot is inset with a schematic of the corresponding detection location. (a) Location G0, the PGL/graphene interface. (b) The middle graphene region, GM. (c) The right hand side graphene/metal interface, GR, horizontally aligned from G0. (d) The top interface, GT, vertically above G0. (e) The interface, GB, vertically below G0.

Table 6.1: Pulse and offset parameters as recorded at 5 locations on a graphene semi-circle geometry switch.

Location	Pulse amplitude (nA)	DC component (nA)	Arrival time (Δfs)
G0	1.53	-6.67	0
GM	1.46	-0.39	69
GR	0.28	1.61	406
GT	0.17	1.96	218
GB	0.44	2.03	275

The DC component as a function of location shows similar results to those demonstrated for the straight device in Section 6.2, where the illumination location G0 produces a negative current and the illumination locations at the opposing contact each produce a positive current. It is clear that at the location G0 the photocurrent was significantly higher than the locations GT, GR and GB. There are two interesting mechanisms that must be considered to understand why this is the case. First, when a single edge location is illuminated (GT, GR or GB), the surrounding non-illuminated areas act as resistive shunts to ground, reducing the current that flows from the ground plane to G0. e.g. If the location GR is illuminated, current will flow from here towards all metal edges, including GT, GB and G0. Secondly, when each of the circumference locations are illuminated, a greater total current is expected to be produced to that of G0, as the area of the graphene/metal interface under illumination by the 24 μm beam is also larger. The net effect is that a larger initial current is created under illumination at the edge in comparison to G0, although the proportion of the current that is measured by the lock-in is lower, owing to the resistive effects of the non-illuminated graphene regions.

The time of flight for the pulse across a distance of 100 μm from G0 to GR corresponds to a velocity of 2.46×10^8 m s^{-1}. If correct, this would indicate very weak confinement of the pulse across the graphene region, results which do not reflect the response seen for the straight device. It is also calculated, however, that the same process applied to location GT would result in a velocity of 4.58×10^8 m s^{-1} which is clearly incorrect. A closer inspection of the Lorentzian pulse fitting showed that although amplitude and offset data could be accurately reconstructed, the exact pulse shape was complex and changed slightly at each location, potentially shifting pulse centre parameter. The time at which the highest current was produced was subsequently investigated, and also returned similarly erroneous velocities. As the propagation distance is small in comparison to the wavelength of the pulse, a small amount of noise had significant effects on the location of the centre of the pulse. This was a major motivation for conducting later measurements which used the 200 μm semi-circle device to reduce the measurement error.

The width of the pulse was found to be 3.2 ± 0.2 ps for each of the scans, which is typical in comparison to the values for graphene detection throughout this thesis. However, the same pulse broadening as a function of distance, seen in Section 6.2, was not observed. Another unique feature of these results is the features observed at −9 ps at all locations and the large peak at 25 ps at location GR. What was unique about these features is that the amplitude varied as a function of detection location and was not linked to any physical features of the device. It is proposed that they are a result of optical pulse reflections from the gold at the back of the device. This device was not bonded to the chip holder using black Apiezon wax, as used in all other devices, but instead transparent PMMA was used. It is expected that when the beam hits the edge of the metal, it is scattered, travels through the quartz, reflects off the metallic chip package below and hits the LT-GaAs "input" switch. The velocity of the optical pulse in quartz (permittivity 3.8) is 1.54×10^8 m s^{-1} and the shortest reflection path possible is 1.12 mm equivalent to a time of 7.46 ps. As the probe beam must occur in advance of the pump beam to account for the propagation delay, this would be seen at −7.46 ps on the time-domain plot. This, however, assumes that the thickness of the PMMA is negligible, which explains why the full 9 ps advance in time is not accounted for. The relative permittivity of PMMA can vary from 2.8 to 4; if, for convenience, a value of 3.8 is also chosen the PMMA thickness must be 154 μm in order to account for a value of ~9 ps.

The amplitudes of each of the main pulses were observed to decrease as the detection location moved away from the PGL, towards the circumference of the semi-circle. A further decrease in pulse amplitude was observed when detected at the top region (GT). This could be expected if the mode formed on the PGL was launched towards the position GR at the graphene/metal interface i.e. the PGL operated as a directional antenna. However, the amplitude of the pulse detected at GB contradicts this as it is larger than both GT and GR. Changes in the graphene properties at this location were considered, but the PTE current generated at GT, GR and GB did not indicate any significant changes to the properties of the graphene, and the values do not correlate with the pulse amplitude. Alternatively, the pulse amplitude may be larger at the bottom detection location because the beam illuminated a metal feature, such as the 90° corner of the ground plane, where enhanced confinement of the field may have produced a larger pulse.

Overall, the 100 μm device showed a range of unexpected behaviour, including features at −9 ps, very small variations in pulse FWHM over the length of the graphene, and non-symmetrical pulse amplitudes between GB and GT. It is expected that almost all of these characteristics are due to the influence of optical reflections from the rear side of the device, or variations in the properties of the graphene. All fabrication steps were identical to the 200 μm device, other than the PMMA bonding to the chip package and it is clear from the results that follow that these behaviours are not replicated.

As a variation in pulse detection at a range of positions was shown to produce interesting results, pulse mapping on the 200 μm device was performed. Before mapping the terahertz pulses, both the device and the OC-THz-TDS mapping system needed to be characterised. The device was initially characterised using the same system as the 100 μm device and the performance was deemed to be better (than the 200 μm device) at lower powers because of higher SNR switches and black Apiezon wax prevented reflections from the metal backplane of the chip package. The device was then transferred to the mapping system where the photocurrent produced by the LT-GaAs switches under zero bias was scanned to calibrate the piezo stages. Figure 6.8 shows these results, where the

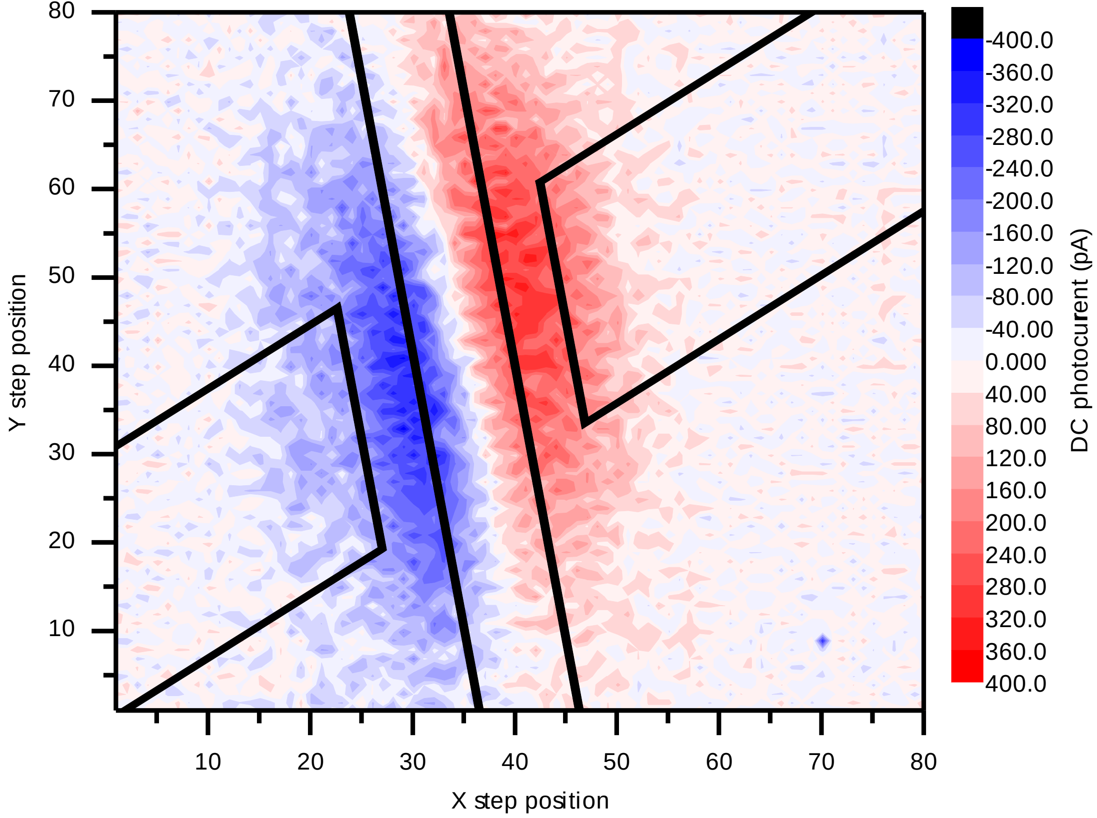

Figure 6.8: DC photocurrent map of the LT-GaAs switch. The top right contact was connected to a lock-in amplifier and the centre conductor and bottom left contact were grounded. The black lines indicate the approximate location of the metal regions and display some slight skewing.

approximate locations of the metal centre conductor and switches are overlaid in black. The level of image skewing can clearly be seen in these results and was caused by a combination of the open-loop control configuration of the stages and the different voltages required to produce equal forward and reverse step sizes in the piezoelectric motors.

As each scan resolution required independent calibration, two resolutions were chosen corresponding to ~1 μm for small areas and ~5 μm for larger areas. Further results in the chapter have all been plotted in terms of distance based on these figures for clarity. However, the lack of features to calibrate the piezoelectric stages means that these are estimates of scale in each case.

The DC photocurrent map for the graphene region is shown in Figure 6.9 and was recorded using a ~5 μm resolution and with a 2 mW beam. The red region in the middle indicated the location of the PGL/graphene interface (G0), which produced a current of 650 pA. The darker blue semi-circle to the right of this is the graphene/ground plane interface produced a current of approximately −120 pA. It should be noted that for this measurement the lock-in was connected directly to the PGL on the left and hence the DC polarity was inverted relative to the previous measurements of this chapter. The location GR, to the right of G0, displayed photocurrent that was a similar level to the background of the rest of the device, potentially indicating defects in the graphene quality or poor contact to the metal in that region. The OC-THz-TDS measurements were recorded at discrete locations across the device but the only detectable pulses were recorded near to the location G0. The reason for this is attributed to the lower laser powers that had to be used in this system and, hence, the signal was unable to be detected above the background noise levels, even with high levels of averaging. This limited measurements of factors such as propagation velocity, which was one reason this 200 μm device was fabricated, however, mapping of the G0 region with a high resolution still produced some notable results.

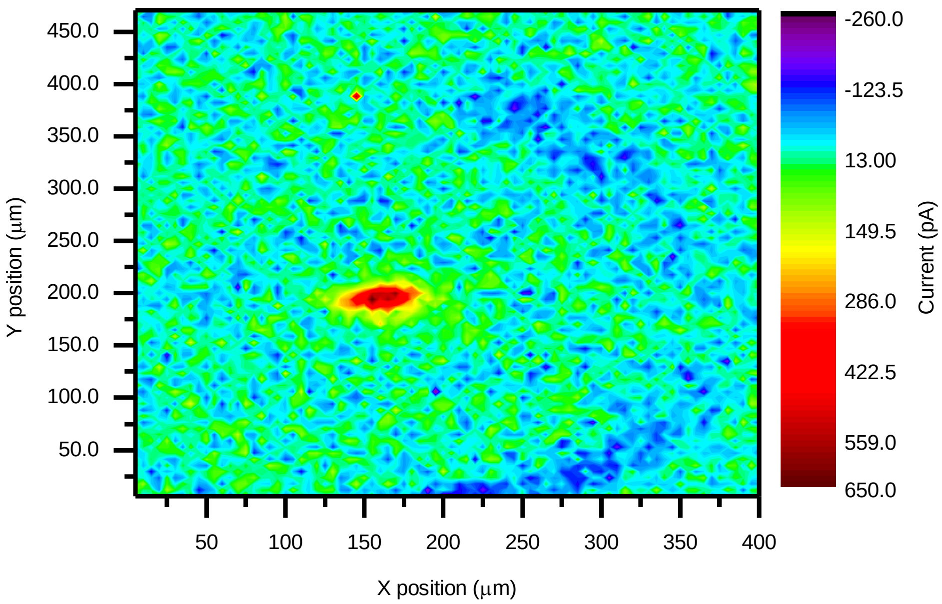

Figure 6.9: DC photocurrent map of the graphene semi-circle switch. The area G0, producing the largest photocurrent is indicated in red and the circumference of the graphene/metal contact produced negative photocurrent, in blue.

The DC offset component for the region around G0 is shown in Figure 6.10, where a full time-domain scan was taken for each pixel using a ~1 μm step calibration. For each scan location the DC current was determined by averaging the first 15 data points of the

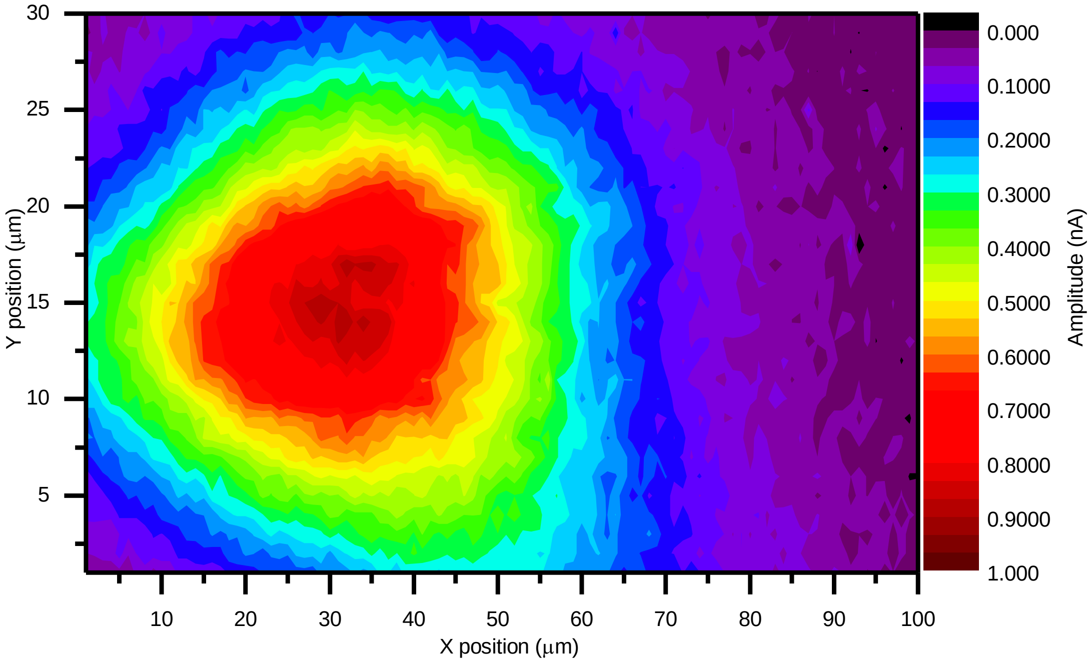

Figure 6.10: High resolution DC photocurrent map of the PGL/graphene contact G0. Each data point is the average value of 15 measurements.

time-domain scan. An area of 30 × 100 pixels in X and Y was recorded to focus on the key pulse detection locations whilst keeping scan times to a sensible limit. The scan took 65 hours to complete using a 60 V bias at the LT-GaAs switch, and the time window measured only the DC background level, rising edge and peak pulse amplitude. Each individual row was found to have a Gaussian distribution of DC current from left to right. In order to obtain an estimate of the beam profile, a point-like current source and Gaussian beam profile was assumed. The FWHM was 7 μm for column 30 and 30 μm row 15, which indicated an elliptical beam pattern.

To plot the pulse amplitude information, each pulse was fitted to a Lorentzian curve and the height parameter was mapped to every pixel. This information is plotted in Figure 6.11. In general the pulse amplitude as a function of position looks very similar to the DC offset data, but the key difference is that the location of peak pulse amplitude is 8 μm further toward the graphene region. This increased pulse amplitude was observed previously in the straight device where the largest pulse amplitude was 5.5 μm away from the PGL/metal interface. However, unlike the straight device, the pulse amplitude beyond this point decays much faster, at the same rate of the DC photocurrent, and is almost undetectable 40 μm away from the PGL/graphene interface. If the confinement of the graphene is very high, a pulse amplitude relationship proportional to 1/r would be

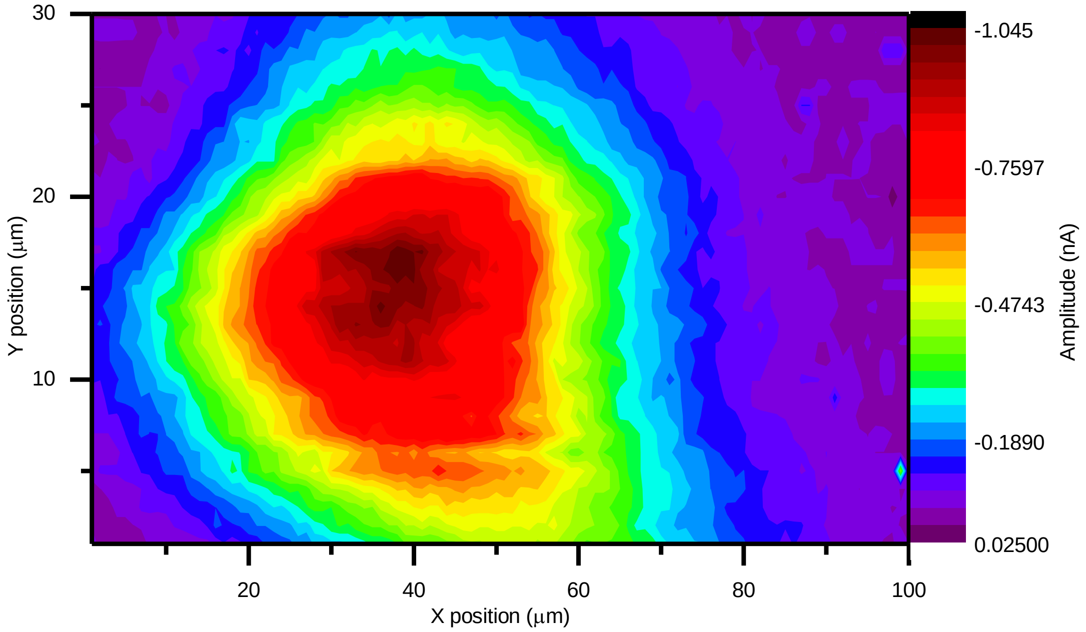

Figure 6.11: The pulse amplitude as detected by graphene at the location G0. All pulses were generated by a 3.5 mW beam at a switch bias of 60 V and detected using a 3.5mW beam on the graphene. The amplitude was determined by a Lorentzian fit of the pulse shape and all values are taken from the same measurement set as Figure 6.10 and, hence, are directly comparable.

expected for a pulse moving away from the centre of a semi-circle of graphene, where r is the radial distance from the PGL. As this is not seen, negligible confinement is expected; where the amplitude of the pulse would decay proportional to $1/r^2$.

This now opens the question of why the pulse was seen clearly across the 50 μm straight device, but not the 200 μm device. First of all, differences in fabrication across each of the three devices may change parameters such as LT-GaAs switch efficiency and graphene carrier concentration. As the "input" pulse and PTE effect are of a similar magnitude in each device, this is not considered to be the reason why the pulse is not detected across the 200 μm span. Therefore, it is proposed that pulse detection is not due to the confinement of the pulse to graphene but predominantly to the confinement of the field between metal features of the device, where the total length between these features determines how much field is present to drive the electrons across the illuminated region of graphene.

Another important factor in the ability of each of these devices to detect a pulse, which would specifically inhibit the detection on the semi-circle devices, is the degree to which the modulation of photoconductivity varies with as a function of distance away from the PGL area. When the pulse illuminates the PGL interface, it has the effect of changing the resistivity analogous to a variable resistor in series with a static resistance. As the pulse moves away from the centre, the analogy changes to a variable resistor in parallel with an increasingly large static resistance. This decreases the magnitude of photoconductive modulation as the detection spot moves away. In all, the number of variables that change as a function of location for the semi-circle geometry makes it a very complex system which creates more questions than answers in the early stages of investigation into graphene pulse detection.

To complement the pulse amplitude information, the area of each pulse from the Lorentzian fitted data is plotted in Figure 6.12, using the same data set used for the offset and amplitude figures above. Anomalous data that did not show satisfactory convergence is illustrated as a grey pixel, where black and white pixels are data points that exceed the negative and positive limits of the colour scale respectively. The rate at which the magnitude decays away from the centre follows a close relationship to the amplitude data, indicating that negligible dispersion is introduced in the relatively small scan region measured.

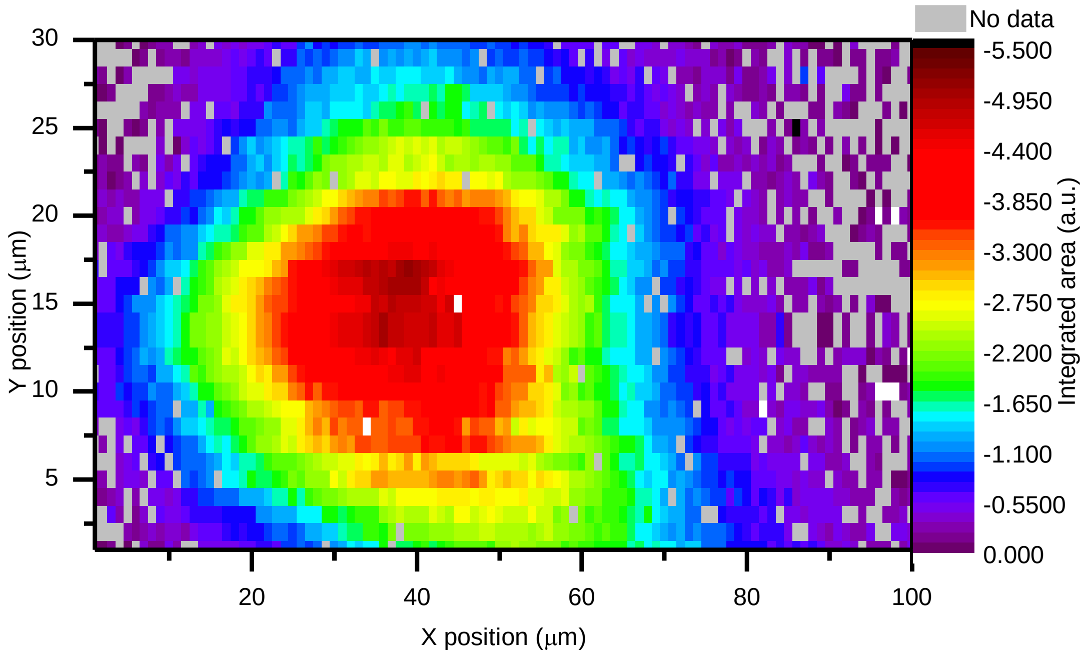

Figure 6.12: The integrated area of each of the pulses detected around the region of G0. The grey pixels represent values that did not converge to a satisfactory level and returned anomalous values. Also taken from the same data set as 6.10 and 6.11.

Two-dimensional mapping of picosecond pulse detection by graphene was measured was to gain an understanding of the influence of the switch geometry on the pulse detection properties. The data has shown that the area immediately next to the PGL/metal interface (G0) is the ideal location for optical sampling as it creates the greatest modulation of the measured current. The non-illuminated areas of the graphene act as a parasitic load to the signal and, ideally, should be minimised wherever possible. With this being said, graphene regions that are smaller than the spot size would not harvest the optical energy efficiently, and may be difficult to align to as the PTE current from either side of the switch will cancel out. Therefore, from the data collected in these measurements, it is hypothesised that the best detection switch geometry is a square graphene channel with the dimensions equal to the FWHM of the optical beam. However, graphene switches that are oriented perpendicular to the terahertz field, in the same manner as the LT-GaAs, have not been investigated, and may reveal improved signal properties.

6.4 Conclusion

Across all of the devices discussed in this chapter, the only consistent responses were seen in the DC offset and pulse amplitude which are detected near the end of the

PGL/graphene interface; and that the maximum pulse amplitude is produced slightly further away that the region of maximum DC current. These similarities are thought to be due to the same PGL dimensions used throughout and similar properties of the graphene itself. Where the devices differ in the performance as the detection position is further away from the end of the PGL line. It was discussed that this would be caused by the profile of the graphene changing relative to the spot size as well as the level confinement of the electric field to the metal features. The acceptable values found for pulse velocity across each span of graphene varied from 33×10^{6} m s^{-1} to 2.46×10^{8} m s^{-1}, but doubt is shed on the accuracy of these results based on the fact that across some spans of graphene velocities in excess of the speed of light would be required.

The 50 μm straight device allowed observation of pulse detection across the entire length of the graphene strip, displaying attenuation, pulse broadening and a gradual increase in arrival time as the pulse moved away from the nearest graphene interface. In the 100 μm semi-circle device pulses were also detected across the entire sheet all the way to the circumference of the graphene. Some of the measurements of this device displayed position dependent features in the time-domain that were attributed to optical pulse reflections from the back of the device. A 200 μm semi-circle was than fabricated using black Apiezon wax to remove these reflections and, after initial testing in the non-scanning setup, it was tested in the piezo stage scanning OC-THz-TDS system. Although the DC component of the signal was observed at all metal/graphene interfaces, no pulses were detected anywhere other than the central PGL/graphene interface.

Chapter 7: Conclusion and future work

7.1 Conclusion

This thesis presents studies of the interaction between graphene and terahertz frequency electromagnetic radiation. The work presented contributes to a deeper understanding of the picosecond time-scale carrier dynamics of graphene. On a technological level, the work demonstrated new techniques for the incorporation of graphene with semiconductor photonic switches on low permittivity substrates. The main conclusion reached is that graphene has the potential to be an important tool in the future of some terahertz device applications, and particularly for terahertz detection.

The design and fabrication techniques adopted several new engineering decisions to increase the device yield, and also to reduce electronic failure during testing. Chapter 3 described the operation of the testing system and the measurement techniques used throughout the thesis. Examples of these techniques were provided for a range of LT-GaAs growth temperatures to illustrate what properties are important when developing a terahertz photoconductive switch. Raman analysis of graphene was used to characterise the devices developed throughout the thesis.

Demonstration of terahertz pulses traveling through adjacently aligned graphene channels found that a large proportion of the signal change was due to the changes in terahertz waveguides. By modulating the graphene with optical pulses, the differential signal could be obtained, removing the cross talk and interference from the rest of the high frequency resonances. It was shown that on-chip optical pump terahertz probe measurements of graphene did not out-perform similar free-space systems used in literature. However, the same picosecond timescale carrier dynamics were observed, demonstrating the potential of graphene to operate at frequencies beyond that of many other semiconductors.

By generating pulses with LT-GaAs and optically sampling the graphene region in Chapter 5, outstanding high frequency photodetector properties were demonstrated where the carrier lifetimes were of the same order of magnitude as LT-GaAs. Graphene terahertz pulse detection was demonstrated to be capable of resolving frequencies over 600 GHz, where the amplitude and pulse width were studied as a function of laser spot size, laser power and bias voltage. Using the same photo-thermoelectric effect, pulse generation by graphene and detection by LT-GaAs was also investigated, so opening a route towards solely graphene-based THz-frequency sensors.

To obtain a deeper understanding of the operation of the dynamics of graphene THz detection, mapping of the probe spot location with respect to the THz pulse was studied in Chapter 6. Measurements along the length of a 50 μm long graphene channel indicated the presence of interesting charge dynamics, particularly in that the charge is conserved over this length. Phase dispersion was also observed, analysis of which identified the graphene region closest to the metal contact as the best location for THz field detection.

2D mapping of larger graphene structures emphasised that the strength of the electric field and an even coverage of the sampling beam onto the width of the graphene channel are both very important factors in the operation of graphene THz detectors.

The main limitations of this work was that there was insufficient time to study these effects as a function of the more fundamental properties of graphene – including its behaviour in magnetic fields, electric fields, and at lower temperatures. These were either limited because of the timeframe of the project, or because of concerns for the interaction of the terahertz radiation with the materials needed to implement them. However, routes towards these investigations are discussed in future work in Section 7.2.

Overall, the work presented in this thesis supports the argument that the fast carrier dynamics of photoexcited carriers realised in graphene could be useful in a number of THz frequency applications. At present conventional semiconductor materials are being pushed to their limits in attempts to utilise the terahertz "gap" and the results presented here pave the way for graphene-based on-chip terahertz sensors.

7.2 Future work

The most progressive direction that this work could take would be to investigate the feasibility of an all-graphene on-chip terahertz device. This work was partially undertaken in Section 5.4 but a more in depth investigation would require iterative steps towards improving the generation and detection efficiency. If this type of device could be shown to operate with cheaper, longer wavelength (1.55 μm wavelength) femtosecond lasers, a disruptive leap in the set-up cost of OC-THz-TDS systems could follow.

As the higher field confinement of on-chip terahertz systems has demonstrated reasonable signal to noise ratios, additional work could also be conducted into developing graphene components for FS-THz-TDS systems. Graphene terahertz detectors were briefly attempted at earlier stages of this project, although no pulse was measured. Since then, a deeper understanding of the detection mechanisms have been developed and documented in this thesis, which will hopefully be of use to future measurements.

In order to obtain a more fundamental understanding of the carrier dynamics in graphene, similar THz spectroscopy measurements to those of Chapter 4 could be repeated under low temperature and under magnetic field. By doing this, studies of edge magnetoplasmons could be conducted in graphene with increased temporal resolution, supporting and expanding upon existing results in the literature.

Finally, it is suggested that measurements if the dependence of carrier concentration on THz pulse generation or detection could be measured. From the outset of this project the field effect manipulation of carrier concentration could only be conducted using a universal back gate, which would screen most of the THz radiation, or via a localised top gate, which would require fabrication techniques not available in the time-frame of the project. This could reveal tuneable dynamics of the graphene such as tuneable plasmon resonances or Pauli blocking.

References

1. Chan, W. L., Deibel, J. & Mittleman, D. M. Imaging with terahertz radiation. *Reports on Progress in Physics* **70,** 1325–1379 (2007).
2. Jepsen, P. U., Cooke, D. G. & Koch, M. Terahertz spectroscopy and imaging - Modern techniques and applications. *Laser and Photonics Reviews* **5,** 124–166 (2011).
3. Kleine-Ostmann, T. & Nagatsuma, T. A review on terahertz communications research. *Journal of Infrared, Millimeter, and Terahertz Waves* **32,** 143–171 (2011).
4. Davies, A. G., Burnett, A. D., Fan, W., Linfield, E. H. & Cunningham, J. E. Terahertz spectroscopy of explosives and drugs. *Materials Today* **11,** 18–26 (2008).
5. Novoselov, K. S., Geim, A. K., Morozov, S. V., Jiang, D., Zhang, Y., Dubonos, S. V., Grigorieva, I. V. & Firsov, A. A. Electric field effect in atomically thin carbon films. *Science* **306,** 666–669 (2004).
6. Morozov, S. V., Novoselov, K. S., Katsnelson, M. I., Schedin, F., Elias, D. C., Jaszczak, J. A. & Geim, A. K. Giant intrinsic carrier mobilities in graphene and its bilayer. *Physical Review Letters* **100,** 016602 (2008).
7. Dean, C. R., Young, A. F., Meric, I., Lee, C., Wang, L., Sorgenfrei, S., Watanabe, K., Taniguchi, T., Kim, P. & Shepard, K. L. Boron nitride substrates for high-quality graphene electronics. *Nature nanotechnology* **5,** 722–726 (2010).
8. Nair, R. R., Blake, P., Grigorenko, A. N., Novoselov, K. S., Booth, T. J., Stauber, T., Peres, N. M. R. & Geim, A. K. Fine structure constant defines visual transparency of graphene. *Science* **320,** 1308–1308 (2008).
9. Gabor, N. M., Song, J. C., Ma, Q., Nair, N. L., Taychatanapat, T., Watanabe, K., Taniguchi, T., Levitov, L. S. & Jarillo-Herrero, P. Hot carrier–assisted intrinsic photoresponse in graphene. *Science* **334,** 648–652 (2011).
10. Tielrooij, K. J., Song, J. C. W., Jensen, S. A., Centeno, A., Pesquera, A., Elorza, A. Z., Bonn, M., Levitov, L. S. & Koppens, F. H. L. Photoexcitation cascade and multiple hot-carrier generation in graphene. *Nature Physics* **9,** 248–252 (2013).

11. George, P. A., Strait, J., Dawlaty, J., Shivaraman, S., Chandrashekhar, M., Rana, F. & Spencer, M. G. Ultrafast optical-pump terahertz-probe spectroscopy of the carrier relaxation and recombination dynamics in epitaxial graphene. *Nano letters* **8,** 4248–4251 (2008).
12. Strait, J. H., Wang, H., Shivaraman, S., Shields, V., Spencer, M. & Rana, F. Very slow cooling dynamics of photoexcited carriers in graphene observed by optical-pump terahertz-probe spectroscopy. *Nano Letters* **11,** 4902–4906 (2011).
13. Lin, K.-C., Li, M.-Y., Li, L. J., Ling, D. C., Chi, C. C. & Chen, J.-C. Ultrafast dynamics of hot electrons and phonons in chemical vapor deposited graphene. *Journal of Applied Physics* **113,** (2013).
14. Ju, L., Geng, B., Horng, J., Girit, C., Martin, M., Hao, Z., Bechtel, H. A., Liang, X., Zettl, A., Shen, Y. R. & Wang, F. Graphene plasmonics for tunable terahertz metamaterials. *Nature Nanotechnology* **6,** 630–634 (2010).
15. Grigorenko, A. N., Polini, M. & Novoselov, K. S. Graphene plasmonics. *Nature Photonics* **6,** 749–758 (2012).
16. Boubanga-Tombet, S., Chan, S., Watanabe, T., Satou, A., Ryzhii, V. & Otsuji, T. Ultrafast carrier dynamics and terahertz emission in optically pumped graphene at room temperature. *Phys. Rev. B* **85,** 035443 (2012).
17. Li, T., Luo, L., Hupalo, M., Zhang, J., Tringides, M. C., Schmalian, J. & Wang, J. Femtosecond Population Inversion and Stimulated Emission of Dense Dirac Fermions in Graphene. *Phys. Rev. Lett.* **108,** 167401 (2012).
18. Cheng, R., Bai, J., Liao, L., Zhou, H., Chen, Y., Liu, L., Lin, Y.-C., Jiang, S., Huang, Y. & Duan, X. High-frequency self-aligned graphene transistors with transferred gate stacks. *Proceedings of the National Academy of Sciences of the United States of America* **109,** 11588–11592 (2012).
19. Schwierz, F. Graphene transistors: Status, prospects, and problems. *Proceedings of the IEEE* **101,** 1567–1584 (2013).

20. Bae, S., Kim, H., Lee, Y., Xu, X., Park, J.-S., Zheng, Y., Balakrishnan, J., Lei, T., Ri Kim, H., Song, Y. I., Kim, Y.-J., Kim, K. S., Özyilmaz, B., Ahn, J.-H., Hong, B. H. & Iijima, S. Roll-to-roll production of 30-inch graphene films for transparent electrodes. *Nature Nanotechnology* **5,** 574–578 (2010).

21. Lee, C., Kim, J. Y., Bae, S., Kim, K. S., Hong, B. H. & Choi, E. J. Optical response of large scale single layer graphene. *Applied Physics Letters* **98,** 071905 (2011).

22. Dawlaty, J. M., Shivaraman, S., Strait, J., George, P., Chandrashekhar, M., Rana, F., Spencer, M. G., Veksler, D. & Chen, Y. Measurement of the optical absorption spectra of epitaxial graphene from terahertz to visible. *Applied Physics Letters* **93,** (2008).

23. Horng, J., Chen, C.-F., Geng, B., Girit, C., Zhang, Y., Hao, Z., Bechtel, H. A., Martin, M., Zettl, A., Crommie, M. F., Shen, Y. R. & Wang, F. Drude conductivity of Dirac fermions in graphene. *Physical Review B - Condensed Matter and Materials Physics* **83,** (2011).

24. Paul, M. J., Tomaino, J. L., Kevek, J. W., Deborde, T., Thompson, Z. J., Minot, E. D. & Lee, Y.-S. Terahertz imaging of inhomogeneous electrodynamics in single-layer graphene embedded in dielectrics. *Applied Physics Letters* **101,** (2012).

25. Maeng, I., Lim, S., Chae, S. J., Lee, Y. H., Choi, H. & Son, J.-H. Gate-controlled nonlinear conductivity of Dirac fermion in graphene field-effect transistors measured by terahertz time-domain spectroscopy. *Nano Letters* **12,** 551–555 (2012).

26. Choi, H., Borondics, F., Siegel, D. A., Zhou, S. Y., Martin, M. C., Lanzara, A. & Kaindl, R. A. Broadband electromagnetic response and ultrafast dynamics of few-layer epitaxial graphene. *Applied Physics Letters* **94,** (2009).

27. Lao, Y.-F., Unil Perera, A. G., Shepperd, K., Wang, F., Conrad, E. H. & Williams, M. D. Temperature-dependent far-infrared response of epitaxial multilayer graphene. *Applied Physics Letters* **102,** (2013).

28. Low, T. & Avouris, P. Graphene plasmonics for terahertz to mid-infrared applications. *ACS Nano* **8,** 1086–1101 (2014).
29. Nikitin, A. Y., Guinea, F., García-Vidal, F. J. & Martín-Moreno, L. Edge and waveguide terahertz surface plasmon modes in graphene microribbons. *Physical Review B - Condensed Matter and Materials Physics* **84,** (2011).
30. Ryzhii, V., Ryzhii, M. & Otsuji, T. Negative dynamic conductivity of graphene with optical pumping. *Journal of Applied Physics* **101,** (2007).
31. Yan, H., Li, X., Chandra, B., Tulevski, G., Wu, Y., Freitag, M., Zhu, W., Avouris, P. & Xia, F. Tunable infrared plasmonic devices using graphene/insulator stacks. *Nature Nanotechnology* **7,** 330–334 (2012).
32. Xia, F., Farmer, D. B., Lin, Y.-M. & Avouris, P. Graphene field-effect transistors with high on/off current ratio and large transport band gap at room temperature. *Nano Letters* **10,** 715–718 (2010).
33. Skulason, H. S., Nguyen, H. V., Guermoune, A., Sridharan, V., Siaj, M., Caloz, C. & Szkopek, T. 110 GHz measurement of large-area graphene integrated in low-loss microwave structures. *Applied Physics Letters* **99,** 153504 (2011).
34. Petković, I., Williams, F. I. B., Bennaceur, K., Portier, F., Roche, P. & Glattli, D. C. Carrier drift velocity and edge magnetoplasmons in graphene. *Physical Review Letters* **110,** (2013).
35. Auston, D. H. Picosecond optoelectronic switching and gating in silicon. *Applied Physics Letters* **26,** 101–103 (1975).
36. Dazhang, L., Cunningham, J., Byrne, M. B., Khanna, S., Wood, C. D., Burnett, A. D., Ershad, S. M., Linfield, E. H. & Davies, A. G. On-chip terahertz Goubau-line waveguides with integrated photoconductive emitters and mode-discriminating detectors. *Applied Physics Letters* **95,** (2009).

37. Shi, S.-F., Tang, T.-T., Zeng, B., Ju, L., Zhou, Q., Zettl, A. & Wang, F. Controlling graphene ultrafast hot carrier response from metal-like to semiconductor-like by electrostatic gating. *Nano Letters* **14,** 1578–1582 (2014).

38. Gan, X., Shiue, R.-J., Gao, Y., Meric, I., Heinz, T. F., Shepard, K., Hone, J., Assefa, S. & Englund, D. Chip-integrated ultrafast graphene photodetector with high responsivity. *Nature Photonics* **7,** 883–887 (2013).

39. Gacemi, D., Mangeney, J., Laurtent, T., Lampin, J.-F., Akalin, T., Blary, K., Degiron, A., Crozat, P. & Meng, F. THz surface plasmon modes on planar Goubau lines. *Optics Express* **20,** 8466–8471 (2012).

40. Prechtel, L., Song, L., Schuh, D., Ajayan, P., Wegscheider, W. & Holleitner, A. W. Time-resolved ultrafast photocurrents and terahertz generation in freely suspended graphene. *Nature Communications* **3,** (2012).

41. Gordy, W. Microwave spectroscopy. *Reviews of Modern Physics* **20,** 668–717 (1948).

42. Burrus, C. A. & Gordy, W. Submillimeter wave spectroscopy [8]. *Physical Review* **93,** 897–898 (1954).

43. Smith, P. R., Auston, D. H., Johnson, A. M. & Augustyniak, W. M. Picosecond photoconductivity in radiation-damaged silicon-on-sapphire films. *Applied Physics Letters* **38,** 47–50 (1981).

44. Auston, D. H., Lavallard, P., Sol, N. & Kaplan, D. An amorphous silicon photodetector for picosecond pulses. *Applied Physics Letters* **36,** 66–68 (1980).

45. Auston, D. H., Johnson, A. M., Smith, P. R. & Bean, J. C. Picosecond optoelectronic detection, sampling, and correlation measurements in amorphous semiconductors. *Applied Physics Letters* **37,** 371–373 (1980).

46. Nuss, M. C., Auston, D. H. & Capasso, F. Direct subpicosecond measurement of carrier mobility of photoexcited electrons in gallium arsenide. *Physical Review Letters* **58,** 2355–2358 (1987).

47. Gallagher, W. J., Chi, C.-C., Duling, I. N., Grischkowsky, D., Halas, N. J., Ketchen, M. B. & Kleinsasser, A. W. Subpicosecond optoelectronic study of resistive and superconductive transmission lines. *Applied Physics Letters* **50,** 350–352 (1987).

48. Walther, M., Freeman, M. R. & Hegmann, F. A. Metal-wire terahertz time-domain spectroscopy. *Applied Physics Letters* **87,** 1–3 (2005).

49. Defonzo, A. P., Jarwala, M. & Lutz, C. Transient response of planar integrated optoelectronic antennas. *Applied Physics Letters* **50,** 1155–1157 (1987).

50. Rice, A., Jin, Y., Ma, X. F., Zhang, X.-C., Bliss, D., Larkin, J. & Alexander, M. Terahertz optical rectification from ⟨110⟩ zinc-blende crystals. *Applied Physics Letters* **64,** 1324–1326 (1994).

51. Bonvalet, A., Joffre, M., Martin, J. L. & Migus, A. Generation of ultrabroadband femtosecond pulses in the mid-infrared by optical rectification of 15 fs light pulses at 100 MHz repetition rate. *Applied Physics Letters* **67,** 2907 (1995).

52. Wang, K. & Mittleman, D. M. Metal wires for terahertz wave guiding. *Nature* **432,** 376–379 (2004).

53. Sommerfeld, A. Ueber die Fortpflanzung elektrodynamischer Wellen längs eines Drahtes. *Annalen der Physik* **303,** 233–290 (1899).

54. Ashoori, R. C., Stormer, H. L., Pfeiffer, L. N., Baldwin, K. W. & West, K. Edge magnetoplasmons in the time domain. *Physical Review B* **45,** 3894–3897 (1992).

55. Shaner, E. A. & Lyon, S. A. Time-resolved impulse response of the magnetoplasmon resonance in a two-dimensional electron gas. *Physical Review B - Condensed Matter and Materials Physics* **66,** 414021–414023 (2002).

56. Ulbricht, R., Hendry, E., Shan, J., Heinz, T. F. & Bonn, M. Carrier dynamics in semiconductors studied with time-resolved terahertz spectroscopy. *Reviews of Modern Physics* **83,** 543–586 (2011).

57. Zhong, Z., Gabor, N. M., Sharping, J. E., Gaeta, A. L. & McEuen, P. L. Terahertz time-domain measurement of ballistic electron resonance in a single-walled carbon nanotube. *Nature Nanotechnology* **3,** 201–205 (2008).

58. Gupta, S., Frankel, M. Y., Valdmanis, J. A., Whitaker, J. F., Mourou, G. A., Smith, F. W. & Calawa, A. R. Subpicosecond carrier lifetime in GaAs grown by molecular beam epitaxy at low temperatures. *Applied Physics Letters* **59,** 3276–3278 (1991).

59. Krotkus, A., Marcinkevicius, S., Jasinski, J., Kaminska, M., Tan, H. H. & Jagadish, C. Picosecond carrier lifetime in GaAs implanted with high doses of As ions: an alternative material to low-temperature GaAs for optoelectronic applications. *Applied Physics Letters* **66,** 3304–3306 (1995).

60. Liu, M. Y., Chou, S. Y., Hsiang, T. Y., Alexandrou, S. & Sobolewski, R. Nanoscale metal–semiconductor–metal photodetectors with subpicosecond response time fabricated using electron beam lithography. *Journal of Vacuum Science & Technology B* **10,** 2932–2935 (1992).

61. Dietz, R. J. B., Gerhard, M., Stanze, D., Koch, M., Sartorius, B. & Schell, M. THz generation at 1.55 μm excitation: Six-fold increase in THz conversion efficiency by separated photoconductive and trapping regions. *Optics Express* **19,** 25911–25917 (2011).

62. Brener, I., Dykaar, D., Frommer, A., Pfeiffer, L. N., Lopata, J., Wynn, J., West, K. & Nuss, M. C. Terahertz emission from electric field singularities in biased semiconductors. *Optics Letters* **21,** 1924–1926 (1996).

63. Treizebré, A., Akalin, T. & Bocquet, B. Planar excitation of goubau transmission lines for THz BioMEMS. *IEEE Microwave and Wireless Components Letters* **15,** 886–888 (2005).

64. Cohn, S. B. Slot line on a dielectric substrate. *Microwave Theory and Techniques, IEEE Transactions on* **17,** 768–778 (1969).

65. Akalin, T., Treizebré, A. & Bocquet, B. Single-wire transmission lines at terahertz frequencies. *Microwave Theory and Techniques, IEEE Transactions on* **54,** 2762–2767 (2006).

66. Goubau, G. Surface waves and their application to transmission lines. *Journal of Applied Physics* **21,** 1119–1128 (1950).

67. Treizebre, A., Laurette, S., Xu, Y., Bosisio, R. G. & Bocquet, B. THz power divider circuits on planar Goubau lines (PGLS). *Progress In Electromagnetics Research C* **26,** 219–228 (2012).

68. Russell, C., Wood, C. D., Burnett, A. D., Li, L., Linfield, E. H., Davies, A. G. & Cunningham, J. E. Spectroscopy of polycrystalline materials using thinned-substrate planar Goubau line at cryogenic temperatures. *Lab on a Chip - Miniaturisation for Chemistry and Biology* **13,** 4065–4070 (2013).

69. Gacemi, D., Mangeney, J., Colombelli, R. & Degiron, A. Subwavelength metallic waveguides as a tool for extreme confinement of THz surface waves. *Scientific Reports* **3,** (2013).

70. Russell, C. Broadband On-chip Terahertz Spectroscopy. (2013).

71. Wallace, P. R. The band theory of graphite. *Physical Review* **71,** 622–634 (1947).

72. Novoselov, K. S., Geim, A. K., Morozov, S. V., Jiang, D., Zhang, Y., Dubonos, S. V., Grigorieva, I. V. & Firsov, A. A. Electric field in atomically thin carbon films. *Science* **306,** 666–669 (2004).

73. Peierls, R. Quelques propriétés typiques des corps solides. in *Annales de l'institut Henri Poincaré* **5,** 177–222 (Presses universitaires de France, 1935).

74. Landau, L. D. Zur Theorie der phasenumwandlungen II. *Phys. Z. Sowjetunion* **11,** 26–35 (1937).

75. Frank, I. W., Tanenbaum, D. M., Van der Zande, A. M. & McEuen, P. L. Mechanical properties of suspended graphene sheets. *Journal of Vacuum Science & Technology B* **25,** 2558–2561 (2007).

76. Balandin, A. A., Ghosh, S., Bao, W., Calizo, I., Teweldebrhan, D., Miao, F. & Lau, C. N. Superior thermal conductivity of single-layer graphene. *Nano Letters* **8,** 902–907 (2008).

77. Zhang, Y., Tan, Y.-W., Stormer, H. L. & Kim, P. Experimental observation of the quantum Hall effect and Berry's phase in graphene. *Nature* **438,** 201–204 (2005).

78. Castro Neto, A. H., Guinea, F., Peres, N. M. R., Novoselov, K. S. & Geim, A. K. The electronic properties of graphene. *Reviews of Modern Physics* **81,** 109–162 (2009).

79. Bolotin, K. I., Sikes, K. J., Jiang, Z., Klima, M., Fudenberg, G., Hone, J., Kim, P. & Stormer, H. L. Ultrahigh electron mobility in suspended graphene. *Solid State Communications* **146,** 351–355 (2008).

80. Graphene Industries -> Products. at <http://grapheneindustries.com/?Products>

81. Berger, C., Song, Z., Li, T., Li, X., Ogbazghi, A. Y., Feng, R., Dai, Z., Alexei, N., Conrad, M. E. H., First, P. N. & De Heer, W. A. Ultrathin epitaxial graphite: 2D electron gas properties and a route toward graphene-based nanoelectronics. *Journal of Physical Chemistry B* **108,** 19912–19916 (2004).

82. Hass, J., De Heer, W. A. & Conrad, E. H. The growth and morphology of epitaxial multilayer graphene. *Journal of Physics Condensed Matter* **20,** (2008).

83. Hass, J., Varchon, F., Millán-Otoya, J. E., Sprinkle, M., Sharma, N., De Heer, W. A., Berger, C., First, P. N., Magaud, L. & Conrad, E. H. Why multilayer graphene on 4H-SiC$(000\bar{1})$ behaves like a single sheet of graphene. *Physical Review Letters* **100,** (2008).

84. Orlita, M., Faugeras, C., Plochocka, P., Neugebauer, P., Martinez, G., Maude, D. K., Barra, A.-L., Sprinkle, M., Berger, C., De Heer, W. A. & Potemski, M. Approaching the dirac point in high-mobility multilayer epitaxial graphene. *Physical Review Letters* **101,** (2008).

85. Mattevi, C., Kim, H. & Chhowalla, M. A review of chemical vapour deposition of graphene on copper. *Journal of Materials Chemistry* **21,** 3324–3334 (2011).

86. Petrone, N., Dean, C. R., Meric, I., van Der Zande, A. M., Huang, P. Y., Wang, L., Muller, D., Shepard, K. L. & Hone, J. Chemical vapor deposition-derived graphene with electrical performance of exfoliated graphene. *Nano letters* **12,** 2751–2756 (2012).

87. Vlassiouk, I., Regmi, M., Fulvio, P., Dai, S., Datskos, P., Eres, G. & Smirnov, S. Role of hydrogen in chemical vapor deposition growth of large single-crystal graphene. *ACS Nano* **5,** 6069–6076 (2011).

88. Yan, Z., Lin, J., Peng, Z., Sun, Z., Zhu, Y., Li, L., Xiang, C., Samuel, E. L., Kittrell, C. & Tour, J. M. Toward the synthesis of wafer-scale single-crystal graphene on copper foils. *ACS Nano* **6,** 9110–9117 (2012).

89. Al-Temimy, A., Riedl, C. & Starke, U. Low temperature growth of epitaxial graphene on SiC induced by carbon evaporation. *Applied Physics Letters* **95,** (2009).

90. Stankovich, S., Piner, R. D., Chen, X., Wu, N., Nguyen, S. T. & Ruoff, R. S. Stable aqueous dispersions of graphitic nanoplatelets via the reduction of exfoliated graphite oxide in the presence of poly(sodium 4-styrenesulfonate). *Journal of Materials Chemistry* **16,** 155–158 (2006).

91. Choucair, M., Thordarson, P. & Stride, J. A. Gram-scale production of graphene based on solvothermal synthesis and sonication. *Nature Nanotechnology* **4,** 30–33 (2009).

92. Haering, R. R. Band structure of rhombohedral graphite. *Canadian Journal of Physics* **36,** 352–362 (1958).

93. Dresselhaus, M. S., Dresselhaus, G. & Saito, R. Physics of carbon nanotubes. *Carbon* **33,** 883–891 (1995).

94. Charlier, J.-C., Eklund, P. C., Zhu, J. & Ferrari, A. C. *Electron and phonon properties of graphene: Their relationship with carbon nanotubes.* **111,** (2008).

95. Novoselov, K. S., Geim, A. K., Morozov, S. V., Jiang, D., Katsnelson, M. I., Grigorieva, I. V., Dubonos, S. V. & Firsov, A. A. Two-dimensional gas of massless Dirac fermions in graphene. *Nature* **438,** 197–200 (2005).
96. Tan, Y.-W., Zhang, Y., Bolotin, K., Zhao, Y., Adam, S., Hwang, E. H., Das Sarma, S., Stormer, H. L. & Kim, P. Measurement of scattering rate and minimum conductivity in graphene. *Physical Review Letters* **99,** (2007).
97. Tongay, S., Berke, K., Lemaitre, M., Nasrollahi, Z., Tanner, D. B., Hebard, A. F. & Appleton, B. R. Stable hole doping of graphene for low electrical resistance and high optical transparency. *Nanotechnology* **22,** (2011).
98. Schedin, F., Geim, A. K., Morozov, S. V., Hill, E. W., Blake, P., Katsnelson, M. I. & Novoselov, K. S. Detection of individual gas molecules adsorbed on graphene. *Nature materials* **6,** 652–655 (2007).
99. Dan, Y., Lu, Y., Kybert, N. J., Luo, Z. & Johnson, A. C. Intrinsic response of graphene vapor sensors. *Nano Letters* **9,** 1472–1475 (2009).
100. Hess, L. H., Hauf, M. V., Seifert, M., Speck, F., Seyller, T., Stutzmann, M., Sharp, I. D. & Garrido, J. A. High-transconductance graphene solution-gated field effect transistors. *Applied Physics Letters* **99,** 033503 (2011).
101. Pirkle, A., Chan, J., Venugopal, A., Hinojos, D., Magnuson, C. W., McDonnell, S., Colombo, L., Vogel, E. M., Ruoff, R. S. & Wallace, R. M. The effect of chemical residues on the physical and electrical properties of chemical vapor deposited graphene transferred to SiO2. *Applied Physics Letters* **99,** 122108 (2011).
102. Yun, J. M., Park, S., Hwang, Y. H., Lee, E.-S., Maiti, U., Moon, H., Kim, B.-H., Bae, B.-S., Kim, Y.-H. & Kim, S. O. Complementary p- and n-Type Polymer Doping for Ambient Stable Graphene Inverter. *ACS Nano* **8,** 650–656 (2014).
103. Lockhart de la Rosa, C. J. Graphene as Transparent Conductive Film for GaN-Based Vertical Cavity Surface Emitting Lasers.

104. Tomaino, J. L., Jameson, A. D., Kevek, J. W., Paul, M. J., van der Zande, A. M., Barton, R. A., McEuen, P. L., Minot, E. D. & Lee, Y.-S. Terahertz imaging and spectroscopy of large-area single-layer graphene. *Optics express* **19,** 141–146 (2011).

105. Dawlaty, J. M., Shivaraman, S., Chandrashekhar, M., Rana, F. & Spencer, M. G. Measurement of ultrafast carrier dynamics in epitaxial graphene. *Applied Physics Letters* **92,** 042116 (2008).

106. Docherty, C. J., Lin, C.-T., Joyce, H. J., Nicholas, R. J., Herz, L. M., Li, L.-J. & Johnston, M. B. Extreme sensitivity of graphene photoconductivity to environmental gases. *Nature Communications* **3,** (2012).

107. Chen, J., Badioli, M., Alonso-González, P., Thongrattanasiri, S., Huth, F., Osmond, J., Spasenović, M., Centeno, A., Pesquera, A. & Godignon, P. Optical nano-imaging of gate-tunable graphene plasmons. *Nature* **487,** 77–81 (2012).

108. Yoon, H., Forsythe, C., Wang, L., Tombros, N., Watanabe, K., Taniguchi, T., Hone, J., Kim, P. & Ham, D. Measurement of collective dynamical mass of Dirac fermions in graphene. *Nature Nanotechnology* **9,** 594–599 (2014).

109. Lee, H.-J., Kim, E., Yook, J.-G. & Jung, J. Intrinsic characteristics of transmission line of graphenes at microwave frequencies. *Applied Physics Letters* **100,** (2012).

110. Bao, Q., Zhang, H., Wang, Y., Ni, Z., Yan, Y., Shen, Z. X., Loh, K. P. & Tang, D. Y. Atomic-layer graphene as a saturable absorber for ultrafast pulsed lasers. *Advanced Functional Materials* **19,** 3077–3083 (2009).

111. Xia, F., Mueller, T., Lin, Y., Valdes-Garcia, A. & Avouris, P. Ultrafast graphene photodetector. *Nature nanotechnology* **4,** 839–843 (2009).

112. Cai, X., Sushkov, A. B., Suess, R. J., Jadidi, M. M., Jenkins, G. S., Nyakiti, L. O., Myers-Ward, R. L., Li, S., Yan, J., Gaskill, D. K., Murphy, T. E., Drew, H. D. & Fuhrer, M. S. Sensitive room-temperature terahertz detection via the photothermoelectric effect in graphene. *Nature Nanotechnology* **9,** 814–819 (2014).

113. Mueller, T., Xia, F. & Avouris, P. Graphene photodetectors for high-speed optical communications. *Nature Photonics* **4,** 297–301 (2010).

114. Song, J. C. W., Rudner, M. S., Marcus, C. M. & Levitov, L. S. Hot carrier transport and photocurrent response in graphene. *Nano Letters* **11,** 4688–4692 (2011).

115. Song, J. C. W. & Levitov, L. S. Energy flows in graphene: Hot carrier dynamics and cooling. *Journal of Physics Condensed Matter* **27,** (2015).

116. Bonaccorso, F., Sun, Z., Hasan, T. & Ferrari, A. C. Graphene photonics and optoelectronics. *Nature Photonics* **4,** 611–622 (2010).

117. Miseikis, V. The Interaction of Graphene with High-Frequency Acoustic and Electromagnetic Waves. (2012).

118. Yablonovitch, E., Gmitter, T., Harbison, J. P. & Bhat, R. Extreme selectivity in the lift-off of epitaxial GaAs films. *Applied Physics Letters* **51,** 2222–2224 (1987).

119. Suk, J. W., Kitt, A., Magnuson, C. W., Hao, Y., Ahmed, S., An, J., Swan, A. K., Goldberg, B. B. & Ruoff, R. S. Transfer of CVD-Grown Monolayer Graphene onto Arbitrary Substrates. *ACS Nano* **5,** 6916–6924 (2011).

120. Demeester, P., Pollentier, I., Dobbelaere, P. D., Brys, C. & Van Deale, P. Epitaxial lift-off and its applications. *Semiconductor Science and Technology* **8,** 1124–1135 (1993).

121. Deng, L., zhu Lin, W. & rong Sun, Z. Response characteristic of femtosecond LT-GaAs photoconductive switches at different voltage biases. *Journal of Physics D: Applied Physics* **42,** 245103 (2009).

122. Blake, P., Hill, E. W., Neto, A. C., Novoselov, K. S., Jiang, D., Yang, R., Booth, T. J. & Geim, A. K. Making graphene visible. *Applied Physics Letters* **91,** 063124 (2007).

123. Meyer, J. C., Geim, A. K., Katsnelson, M. I., Novoselov, K. S., Booth, T. J. & Roth, S. The structure of suspended graphene sheets. *Nature* **446,** 60–63 (2007).

124. Lee, C., Wei, X., Kysar, J. W. & Hone, J. Measurement of the elastic properties and intrinsic strength of monolayer graphene. *science* **321,** 385–388 (2008).

125. Ferrari, A. C., Meyer, J. C., Scardaci, V., Casiraghi, C., Lazzeri, M., Mauri, F., Piscanec, S., Jiang, D., Novoselov, K. S. & Roth, S. Raman spectrum of graphene and graphene layers. *Physical review letters* **97,** 187401 (2006).
126. Ferrari, A. C. & Basko, D. M. Raman spectroscopy as a versatile tool for studying the properties of graphene. *Nature nanotechnology* **8,** 235–246 (2013).
127. Das, A., Pisana, S., Chakraborty, B., Piscanec, S., Saha, S. K., Waghmare, U. V., Novoselov, K. S., Krishnamurthy, H. R., Geim, A. K. & Ferrari, A. C. Monitoring dopants by Raman scattering in an electrochemically top-gated graphene transistor. *Nature nanotechnology* **3,** 210–215 (2008).
128. Van Geelen, A., Hageman, P. R., Bauhuis, G. J., Van Rijsingen, P. C., Schmidt, P. & Giling, L. J. Epitaxial lift-off GaAs solar cell from a reusable GaAs substrate. *Materials Science and Engineering B* **45,** 162–171 (1997).
129. Kumada, N., Tanabe, S., Hibino, H., Kamata, H., Hashisaka, M., Muraki, K. & Fujisawa, T. Plasmon transport in graphene investigated by time-resolved electrical measurements. *Nat Commun* **4,** 1363 (2013).
130. Shah, J., Pinczuk, A., Gossard, A. C. & Wiegmann, W. Energy-loss rates for hot electrons and holes in GaAs quantum wells. *Physical review letters* **54,** 2045 (1985).
131. Lutz, J., Kuchar, F., Ismail, K., Nickel, H. & Schlapp, W. Time resolved measurements of the energy relaxation in the 2DEG of AlGaAs/GaAs. *Semiconductor science and technology* **8,** 399 (1993).
132. Wang, H., Strait, J. H., George, P. A., Shivaraman, S., Shields, V. B., Chandrashekhar, M., Hwang, J., Rana, F., Spencer, M. G. & Ruiz-Vargas, C. S. Ultrafast relaxation dynamics of hot optical phonons in graphene. *Applied Physics Letters* **96,** 081917 (2010).
133. Frenzel, A. J., Lui, C. H., Fang, W., Nair, N. L., Herring, P. K., Jarillo-Herrero, P., Kong, J. & Gedik, N. Observation of suppressed terahertz absorption in photoexcited graphene. *Applied Physics Letters* **102,** (2013).

134. Johannsen, J. C., Ulstrup, S., Cilento, F., Crepaldi, A., Zacchigna, M., Cacho, C., Turcu, I. C. E., Springate, E., Fromm, F., Raidel, C., Seyller, T., Parmigiani, F., Grioni, M. & Hofmann, P. Direct view of hot carrier dynamics in graphene. *Physical Review Letters* **111,** (2013).

135. Suzuki, M. & Tonouchi, M. Fe-implanted InGaAs terahertz emitters for 1.56 μm wavelength excitation. *Applied Physics Letters* **86,** 1–3 (2005).

136. Hunter, N., Mayorov, A. S., Wood, C. D., Russell, C., Li, L., Linfield, E. H., Davies, A. G. & Cunningham, J. E. On-chip picosecond pulse detection and generation using graphene photoconductive switches. *Nano Letters* **15,** 1591–1596 (2015).

137. Echtermeyer, T. J., Nene, P. S., Trushin, M., Gorbachev, R. V., Eiden, A. L., Milana, S., Sun, Z., Schliemann, J., Lidorikis, E., Novoselov, K. S. & Ferrari, A. C. Photothermoelectric and photoelectric contributions to light detection in metal-graphene-metal photodetectors. *Nano Letters* **14,** 3733–3742 (2014).

138. Xu, X., Gabor, N. M., Alden, J. S., van der Zande, A. M. & McEuen, P. L. Photo-thermoelectric effect at a graphene interface junction. *Nano letters* **10,** 562–566 (2009).

139. Khomyakov, P. A., Giovannetti, G., Rusu, P. C., Brocks, G., Van Den Brink, J. & Kelly, P. J. First-principles study of the interaction and charge transfer between graphene and metals. *Physical Review B - Condensed Matter and Materials Physics* **79,** (2009).

140. Song, J. C. W., Tielrooij, K. J., Koppens, F. H. L. & Levitov, L. S. Photoexcited carrier dynamics and impact-excitation cascade in graphene. *Phys. Rev. B* **87,** 155429 (2013).

141. Dember, H. Photoelectromotive force in cuprous oxide crystals. *Phys. Z* **32,** 554–556 (1931).

142. Johnston, M. B., Whittaker, D. M., Corchia, A., Davies, A. G. & Linfield, E. H. Simulation of terahertz generation at semiconductor surfaces. *Physical Review B - Condensed Matter and Materials Physics* **65,** 1653011–1653018 (2002).